Process optimization and electrochemical investigation of nanostructured carbon materials for mixed assembly energy storage devices

by

Belinda Sinothando Moyo

A thesis submitted in partial fulfilment of the requirements for the degree of

MASTER OF SCIENCE (MSc) IN PHYSICS

Faculty of Natural and Agricultural Sciences

University of Pretoria

Hatfield Pretoria

September 2018

Supervisor/promoter: **Prof. N. I. Manyala**

Declaration

I, <u>Moyo, Belinda Sinothando</u> declare that this thesis, entitled "***Process optimization and electrochemical investigation of nanostructured carbon materials for mixed assembly energy storage devices***" which I hereby submit for the Master of Science (MSc), is the result of investigations carried out by me under the supervision of Prof. N. I. Manyala in the Physics department at the University of Pretoria, South Africa and has not previously been submitted by me for a degree at any other tertiary institution. In keeping with the general practice in reporting scientific observations, due acknowledgement and referencing has been made whenever the work described is based on the findings of other investigators.

Signature………………………………… Date………………………………………

ABSTRACT

In this study, the effect of the inclusion of a hydrothermal pre-treatment procedure and varying the mass ratios of the raw material and the activating agents on the electrochemical performance of laboratory-synthesized activated carbon (AC) nanostructures is reported. Symmetric cells and mixed assembly cells were fabricated and tested in this work.

The AC materials were obtained using an environmentally friendly, mild-alkaline potassium based activating agents (AAs). Hibiscus biomass waste and polypyrrole materials were adopted as the raw materials for source of carbon in the optimization process using these AAs to synthesize porous electrochemically active materials.

The incorporation of the hydrothermal (HT) pre-treatment procedure for the hibiscus biomass waste material decreased the optimal carbonization time to 1 hour (sample was noted as (HTAC-1) and increased the specific surface area (SSA) of the material. The effect of the mass ratio of the AA and raw material was analysed for the polypyrrole (PPY) raw material and the SSA as well as the pore volume were found to increase with an increase in the AA ratio to a maximum threshold of 6:1 (sample was noted as AC-PPY-6). A mixed assembly (MA) device fabricated from the HTAC-1 and the AC-PPY-6 samples demonstrated an extended operating potential window of 1.70 V. A good stability was displayed by the MA device after a stability test of 10 000 constant galvanostatic charge-discharge cycles. The device had a capacitance retention of 82% with a corresponding coulombic efficiency of 99.6% respectively. Most importantly, the performance of the device improved after an 80 hour voltage holding ageing test, the capacitance of the device increased as time progressed, from 94.4 $F \cdot g^{-1}$ to 219.5 $F \cdot g^{-1}$.

The stability metrics displayed by the mixed assembly device was relatively better as compared to the AC-PPY-6 and HTAC-1 symmetric devices. Although the capacitance value was lower

compared to the AC-PPY-6 symmetric device, the MA device showed better energy storage capability after voltage holding (floating) tests.

Acknowledgements

Mtinsilana, Mandla Mkhize, Chifundo Mbewe-Khumalo, Mandla Dube and my colleague Mr Raju Kala.

Finally, I would like to express my gratitude to my parents and family for their love, support, and encouragement throughout this journey.

TABLE OF CONTENTS

List of abbreviations and symbols

%:	percentage
@:	at
~:	approximately
<:	less than
>:	greater than
Δ:	change in
A g^{-1}:	amps per gram
A:	amperes
AA:	activating agent
AC:	activated carbon
AC-PPY-0:	activated carbon from polypyrrole with 0:1 AA:PPY ratio
AC-PPY-2:	activated carbon from polypyrrole with 2:1 AA:PPY ratio
AC-PPY-4:	activated carbon from polypyrrole with 4:1 AA:PPY ratio
AC-PPY-6:	activated carbon from polypyrrole with 6:1 AA:PPY ratio
AC-PPY-8:	activated carbon from polypyrrole with 8:1 AA:PPY ratio
Ag/AgCl:	silver/silver chloride
BET:	Brunauer-Emmett-Teller
BJH:	Barrett-Joyner-Halenda
$\overset{\circ}{\text{C}}$ min^{-1}:	degrees Celsius per minute
$\overset{\circ}{\text{C}}$:	degrees Celsius
CAB:	carbon acetylene black
CAS	chemical abstract service
cm:	centimetre
CP:	chronopotentiometry
C$_s$:	specific capacitance
CV:	cyclic voltammetry
CVD:	chemical vapour deposition
DI:	deionized
E:	potential
EDL:	electrochemical double layer
EDLC:	electrochemical double layer capacitors
EDX:	electron dispersive x-ray spectroscopy
EIS:	electrochemical impedance spectroscopy
EMIM-TFSI:	1-ethyl-3-methylimidazolium bis(trifluoromethylsulfonyl)amide
F g^{-1}:	farad per gram
FeCl$_2$:	iron chloride
FeCl$_3$:	iron (III) chloride

Fig.:	figure
FTIR:	Fourier transform infrared spectroscopy
FWHM	Full-width half-maximum
g:	gram
GC:	glassy carbon
GCD:	galvanostatic charge-discharge
H_2SO_4:	sulphuric acid
HCl:	hydrochloric acid
Hg/HgO:	mercury/mercury oxide
HHL:	hydrothermal hibiscus calyces
HT:	hydrothermal
HTAC-1:	hydrothermal activated carbon carbonized for 1 hour
HTAC-2:	hydrothermal activated carbon carbonized for 2 hours
HTAC-4:	hydrothermal activated carbon carbonized for 4 hours
I:	current
IR:	infrared
K:	kelvin
K_2CO_3:	potassium carbonate
KCl:	potassium chloride
keV:	kilo electron-volts
$KHCO_3$:	potassium bicarbonate
KNO_3:	potassium nitrate
KOH:	potassium hydroxide
kV:	kilovolts
M:	molar
m:	mass
$m^2\ g^{-1}$:	square metre per gram
mA:	milli-amps
MA:	mixed assembly
$mAh\ g^{-1}$:	milli-amp hour per gram
mL	millilitres
MnO_2:	manganese dioxide
Na_2SO_4:	sodium sulphate
NaOH:	sodium hydroxide
NFG:	nickel foam graphene
NHTAC-1:	non-hydrothermal activated carbon carbonized for 1 hour
NHTAC-2:	non-hydrothermal activated carbon carbonized for 2 hours
NHTAC-4:	non-hydrothermal activated carbon carbonized for 4 hours
nm:	nanometre
P/P_0:	relative pressure

PPY:	polypyrrole
PSD:	pore size distribution
PVDF:	polyvinylidene fluoride
PYR14-TFSI:	1-butyl-1-methylpyrrolidinium bis(trifluoromethylsulfonyl)amide
R_{ct}:	charge transfer reaction
R_s:	solution resistance
RuO_2:	ruthenium dioxide
s:	seconds
SCE:	standard calomel electrode
Sccm:	standard cubic centimetre per minute
SEM:	scanning electron microscopy
SSA:	specific surface area
TEM:	tunnelling/ transmission electron microscopy
t_{max}:	maximum time
t_{min}:	minimum time
V:	voltage
V_{max}:	maximum voltage
V_{meso}:	mesopore volume
V_{micro}:	micropore volume
V_{min}:	minimum voltage
W:	warburg
$Wh\ kg^{-1}$:	watt hour per kilogram
Wt. %:	percentage weight
Z':	real impedance
-Z'':	imaginary impedance
$ZnCl_2$:	zinc chloride
Ω:	ohms

List of figures

List of tables

List of equations

1. $n\lambda = 2\text{d}\sin\theta$

2. $C_S = \dfrac{I\Delta t}{m\Delta V}$

   Where Δt ($\Delta t = t_{max} - t_{min}$) and ΔV ($\Delta V = V_{max} - V_{min}$)

3. $C_S = \dfrac{I\Delta t}{3.6m}$

4. $m_{negative\ electrode}C_{S_{negative\ electrode}} = m_{positive\ electrode}C_{S_{positive\ electrode}}$

5. $V_t = V_i - m.t^{1/2}$

CHAPTER 1

INTRODUCTION

As the whole world unites in an attempt to diminish the effects of global warming; sustainable and environmentally friendly energy sources which are cleaner and greener, are being investigated as alternatives to those generated from fossil fuels which produce green-house gases [1, 2].

Renewable energy sources such as solar, hydropower, wind and the conversion from kinetic energy to electrical energy are being explored as they meet this criterion. However, for these energy sources to be efficient and effective to meet the global energy demand, reliable energy storage devices, such as batteries and electrochemical capacitors, are needed to harvest the energy for flexible use [1, 2].

Batteries convert stored chemical charges to electrical energy through redox reactions. Electrons move from the anode to the current resulting in an electric current, however they have a short life-span and low power density [3–5]. The most common types of batteries include the lithium ion, nickel-metal hydride, nickel cadmium, zinc-carbon and the alkaline battery [4, 6]. The downside of batteries is that once the required chemical reactant is depleted, they seize to function. The disposal process is costly and releases detrimental chemicals such as mercury, cadmium and dioxins into the environment [3–6].

Electrochemical capacitors, (ECs) commonly known as supercapacitors (SCs) have a long-life cycle, high power and reasonable energy densities [7, 8]. They store energy chemically as charge, giving rise to a potential dependent storage ability.

Supercapacitors can be classified in two categories, namely faradaic and electrochemical double layer capacitors (EDLCs) based on their charge storage mechanisms [1, 2, 7, 8].

Faradaic capacitors undergo a redox process which is responsible for the transfer of charges between the electrode and electrolyte interface [8].

Electrochemical double layer capacitors store charge electrostatically at the electrode-electrolyte interface with the absence of mass and charge transport [8, 9]. The components of EDLCs include two electrodes, an electrolyte and a separator. The separator is made up of an electron insulating yet ion-conducting membrane [9–11].

When an electric potential is applied on one of the EDLC electrodes, it causes an oppositely charged ions to maneuver and accumulate at the surface of the other electrode giving rise to charge separation [9, 10]. EDLCs are mainly composed of carbon-based materials existing in different forms such as activated carbons [11], templated carbon [12], graphene [13], carbon nanotubes [14], carbon aerogels [11] and graphite [15, 16].

Activated carbon can be obtained from the combustion or carbonization of carbonaceous material using either a physical or a chemical activation method. They are the oldest and most commonly adopted EDLC material due to their high porous nature which in turn increases their surface area. They are also chemically stable, electrically conductive, have low-cost implications and not detrimental to the environment [1, 2, 17–19].

In the physical preparation method, the carbon-based material undergoes combustion in a controlled environment at 800 ˚C to 1200 ˚C [20]. This method is time considered to be time consuming as it occurs at high temperatures and the resultant specific surface area is below the critical requirement of a capacitor [20].

In the chemical activation method, a chemical activating agent is added to the carbonaceous material which then undergoes carbonization at a temperature ranging from 600 ˚C to 900 ˚C in the presence of a chemical catalyst [20].

The latter synthesis route is much preferred over the former for the production of activated

carbon due to the ease of morphology and textural characteristic control of the material. Additionally, the time factor involved plays a major role since activated carbon materials prepared via the chemical route can be completed in a shorter period of time [20].

Other sources of activated carbon include renewable carbon sources such as plant and animal biomass, fossil-based carbon sources commonly known as non-renewable carbon which include coal, peat and pitches. Activated carbons can also be produced from synthetic organic polymers such as PVA as well as templated carbon.

In this dissertation, activated carbon samples derived from two different material precursors are produced from an optimized synthesis route. The as-synthesized products were studied using various characterization techniques with potential application for energy storage device electrodes. The selection of the raw materials was based on the conversion of conductive-polymer and low-value biomass raw materials into highly porous nanostructured active electrode materials. The starter materials were laboratory synthesized polypyrrole and naturally-shed hibiscus calyces.

Aim and Objectives

The entire materials production technique was optimized based on the adoption of two distinct activating agents namely, potassium bicarbonate ($KHCO_3$) and potassium carbonate (K_2CO_3) in equal and varying mass ratio of raw material to the activating agent (1:1) for varying carbonization times.

The inclusion of a pre-hydrothermal treatment step for the biomass hibiscus material was also studied to fully elucidate its effect on the percentage of carbon content readily available for activation.

The activated carbon nanostructures from both sources were subjected to extensive material characterization techniques which included scanning electron microscopy (SEM), electron

dispersive x-ray spectroscopy (EDX), transmission electron microscopy (TEM), Raman spectroscopy, Fourier transform infrared spectroscopy (FTIR) and Brunauer–Emmett–Teller (BET) porosity technique. Evaluation of the electrochemical performance of the activated carbon material was also done when fabricated into device electrodes both in half-cell and full device designs, this included cyclic voltammetry, potentiometric charge-discharge and electrochemical impedance spectroscopy analysis.

The combination of the two carbon sources was done in order to exploit their individual electric double layer (EDL) properties to obtain an improved device with respect to its electrochemical capability referred to as a mixed assembly configuration.

Outline of dissertation

This dissertation consists of five chapters which are broken up as follows:

Chapter 1 presents the general introduction in relation to the concerns on environmental degradation due to the increase in energy demands to meet technological development. This chapter also outlines the aims and objectives which will be tackled in this dissertation.

Chapter 2 focuses on the literature review which describes the current active research on activated carbon materials obtained from biomass sources.

Chapter 3 deals with the experimental methodology implemented along with the optimization of the processes adopted in obtaining the final products.

The results of the experimental studies and material analysis are documented and discussed in Chapter 4 with possible elucidation of the research findings.

An overall detailed conclusion of this work is deliberated upon in Chapter 5, possible suggestions for further studies which can be undertaken in a bid to solve the general energy storage problems are also included in this chapter.

References

1. Momodu, D., Okafor, C., Manyala, N., Bello, A., ZebazeKana, M.G. and Ntsoenzok, E. 2017. *Transformation of Plant Biomass Waste into Resourceful Activated Carbon Nanostructures for Mixed-Assembly Type Electrochemical Capacitors.* Waste and Biomass Valorization, pp.1-13.

2. Peng, C., Yan, X.B., Wang, R.T., Lang, J.W., Ou, Y.J. and Xue, Q.J. 2013. *Promising activated carbons derived from waste tea-leaves and their application in high performance supercapacitors electrodes.* Electrochimica Acta, 87, pp.401-408.

3. Divyashree, A. and Hegde, G. 2015. *Activated carbon nanospheres derived from bio-waste materials for supercapacitor applications–a review.* RSC Advances, 5(107), pp.88339-88352.

4. Provazi, K., Campos, B.A., Espinosa, D.C.R. and Tenório, J.A.S. 2011. *Metal separation from mixed types of batteries using selective precipitation and liquid–liquid extraction techniques.* Waste Management, 31(1), pp.59-64.

5. Simon, P., Gogotsi, Y. and Dunn, B. 2014. *Where do batteries end and supercapacitors begin?.* Science, 343(6176), pp.1210-1211.

6. Zhao, L., Yang, D. and Zhu, N.W., 2008. *Bioleaching of spent Ni–Cd batteries by continuous flow system: effect of hydraulic retention time and process load.* Journal of hazardous materials, 160(2-3), pp.648-654.

7. Bello, A., Barzegar, F., Madito, M.J., Momodu, D.Y., Khaleed, A.A., Masikhwa, T.M., Dangbegnon, J.K. and Manyala, N. 2016. *Stability studies of polypyrole-derived carbon based symmetric supercapacitor via potentiostatic floating test.* Electrochimica Acta, 213, pp.107-114.

8. Momodu, D., Madito, M., Barzegar, F., Bello, A., Khaleed, A., Olaniyan, O.,

Dangbegnon, J. and Manyala, N. 2017. A*ctivated carbon derived from tree bark biomass with promising material properties for supercapacitors*. Journal of Solid State Electrochemistry, 21(3), pp.859-872.

9.   Wei, L. and Yushin, G. 2012. *Nanostructured activated carbons from natural precursors for electrical double layer capacitors*. Nano Energy, 1(4), pp.552-565.

10. Wei, L., Sevilla, M., Fuertes, A.B., Mokaya, R. and Yushin, G. 2011. *Hydrothermal carbonization of abundant renewable natural organic chemicals for high‑performance supercapacitor electrodes*. Advanced Energy Materials, 1(3), pp.356-361.

11. Conway, B.E. 2013. *Electrochemical supercapacitors: scientific fundamentals and technological applications*. Springer Science & Business Media.

12. Dutta, S., Bhaumik, A. and Wu, K.C.W. 2014. *Hierarchically porous carbon derived from polymers and biomass: effect of interconnected pores on energy applications*. Energy & Environmental Science, 7(11), pp.3574-3592.

13. Wimalasiri, Y., Fan, R., Zhao, X.S. and Zou, L., 2014. *Assembly of Ni-Al layered double hydroxide and graphene electrodes for supercapacitors*. Electrochimica Acta, 134, pp.127-135.

14. Baughman, R.H., Zakhidov, A.A. and De Heer, W.A., 2002. *Carbon nanotubes--the route toward applications*. Science, 297(5582), pp.787-792.

15. Pierson, H.O., 1993. *Handbook of carbon, graphite, diamond and fullerenes: processing, properties and applications*. Aufl. Park Ridge: Noyes Publications.

16. Burchell, T.D. 1999. *Carbon materials for advanced technologies*. Elsevier.

17. Bello, A., Barzegar, F., Madito, M.J., Momodu, D.Y., Khaleed, A.A., Masikhwa, T.M., Dangbegnon, J.K. and Manyala, N. 2016. *Electrochemical performance of polypyrrole*

derived porous activated carbon-based symmetric supercapacitors in various electrolytes. RSC Advances, 6(72), pp.68141-68149.

18.   Tay, T., Ucar, S. and Karagöz, S., 2009. *Preparation and characterization of activated carbon from waste biomass*. *Journal of Hazardous Materials*, *165*(1-3), pp.481-485.

19.   Yin, J., Zhu, Y., Yue, X., Wang, L., Zhu, H. and Wang, C., 2016. *From environmental pollutant to activated carbons for high-performance supercapacitors*. Electrochimica Acta, 201, pp.96-105.

CHAPTER 2

LITERATURE REVIEW

2.1. Introduction

Carbon is one of the most abundant elements in the world and it can be found in all organic materials. It is the basis of all animal and plant matter. Researchers have taken great interest in "Carbon" due to its versatility based on its electronic structure, $1s^2 2s^2 2p^2$. Carbon has a valence number of 4, which makes it tetravalent [1]. Depending on its hybridization state, carbon can exist in different arrangements; such as bulky balls (0D carbon structure), the 1D form of carbon as nanotubes, the 2D in the form of graphene as well as the stacked multilayer graphene in 3D, commonly known as graphite [2].

Numerous studies have been done on carbon materials as potential energy storage materials due to their abundance, large surface area, good electrical conductivity, high chemical stability and low cost [3–8].

2.2. Activated carbon

Activated carbon (AC) is considered a unique material filled with numerous "holes" held together by van der waals forces commonly referred to as pores [9, 10]. The carbon atoms in AC group themselves into stacks of irregularly sorted, flat aromatic sheets which are randomly cross-linked [10]. The pores have been categorized into three types, micropores (diameter < 2 nm), mesopores (2 nm $\leq$ diameter < 50 nm) and macropores (diameter $\geq$ 50 nm). The presence and the size of the pores within the material make it a great adsorbent and also determine how the adsorption takes place [9].

The synthesis of activated carbon from waste biomass material has become the major interest of many researchers as a result of its abundance in nature, environmentally friendly property, as well as its non-fossil, carbon-containing form [11, 12]. The use of carbon materials with an even larger specific surface area for applications related to electrochemical surface reactions [13–27]

has led to the development of various techniques linked to the preparation of highly porous carbon materials. The process of converting carbon-containing materials into high-surface area porous activated carbon materials is referred to as "activation".

2.2.1. Synthesis of activated carbon

Activated carbon can be synthesised in two different methods which have an influence on the outcome of the surface area as well as the porosity of the material. These are the physical activation and chemical activation methods [28].

In the physical activation method, carbon-based materials undergo combustion at a temperature in the region of 800 °C –1200 °C in the presence of a gas, which results in the release of carbon dioxide or steam [28, 29]. Chemical activation method involves the use of a chemical agent which serves as a catalyst to interact with the material thereby creating the pore structure. Several activating agents such as potassium hydroxide (KOH), sodium hydroxide (NaOH), potassium bicarbonate ($KHCO_3$), zinc chloride ($ZnCl_2$) and iron chloride ($FeCl_2$), to name a few, are added to the raw carbon-containing material in the chemical activation method. The impregnated material then undergoes carbonization at temperatures in the range of 600 °C – 900 °C [28]. The chemical activation method is considered to be advantageous compared to the physical activation method as it permits for more efficient control of the pore and morphological structure of the material, it also allows for an increase in the sample yield as well as a reduction of the activation steps needed and mineral matter content when necessary [28, 30].

The porosity of the activated carbon is of high importance as it affects the electrochemical performance of the material as it allows for ion storage and ion mobility [31–33].

Activated carbon has been derived from diverse biomass waste materials including pine cone [34], banana peels [35], sugar cane bagasse [36] and tree bark [37] to name a few.

2.2.2. Hydrothermal pre-treatment of carbon material

Some researchers have also adopted a pre-hydrothermal step to increase the amount of carbonaceous raw content available in the biomass waste before subjecting it to the actual activation and carbonization process.

Numerous studies have been reported on the hydrothermal carbonization step of biomass material in the synthesis of carbonaceous materials such as carbon spheres, carbon nanotubes, graphite and activated carbon [12].

Sevilla and Fuertes [38] implemented the hydrothermal carbonization step in their work, which reported on the preparation of carbon spheres. In a typical procedure, $2.0 - 16.0$ g of cellulose were dispersed in distilled water and continuously stirred for 4 hours; thereafter, the mixture was transferred into an autoclave with a stirring mechanism and heated for 4 hours at a temperature of 250 °C. The solid product obtained was then rinsed out with distilled water and dried for 4 hours at 120 °C. The final product was found to have a higher carbon content and less oxygen and hydrogen content than the raw biomass material. The porous microspheres obtained were approximately 2-5 µm in diameter. Wang et al. [39] prepared carbon spheres for lithium storage using the hydrothermal process. Simply, 1.5 M sugar solution was subjected to a hydrothermal treatment at 190 °C for 5 hours in an autoclave. The product was then retrieved and carbonized in a tube furnace at 1000 °C under argon gas flow. The final product possessed a nanopore diameter of 0.4 nm, a specific surface area of 400 $m^2 \cdot g^{-1}$ and had a lithium storage capacity of approximately 430 $mAh \cdot g^{-1}$.

This shows that after the hydrothermal step, the thermal treatment of the biomass material gave rise to a solid raw product with a higher carbon content as well as fewer impurities. Additionally, this process also accelerates the physical and chemical interaction between reagents and solvent as well as acid/base reactions [12, 38]. In a study conducted by Hu et al. [12], it was found that directly after the hydrothermal process, a small number of micropores were present within the

material and this process contributed to the pore formation in the material which led to an increased surface area.

Fasakin et al. [35] prepared activated carbon from banana peels at temperatures ranging from 750 °C to 950 °C with KOH as the activating agent in an argon atmosphere. Prior to carbonization, the peels were subjected to hydrothermal treatment in a sulphuric acid solution for 12 hours at a temperature of 160 °C. The sample carbonized at 900 °C resulted in a high specific surface area of 1362 $m^2 \cdot g^{-1}$ with a corresponding specific capacitance of 165 $F \cdot g^{-1}$ at a specific current of 0.5 $A \cdot g^{-1}$.

2.2.3. Activation mechanism

Various techniques have been employed when it comes to the activating mechanism employed on the raw material. Adeniran and Mokaya explored the effect of the activating mechanism on the porosity of the activated carbon from polypyrrole polymer (PPY) [40] for hydrogen storage. PPY serving as the carbon precursor was synthesised and activated with KOH as the activating agent using two different methods to test the effect of compactivation on the final textural properties and hydrogen uptake in the as-synthesized sample. Firstly, the PPY and KOH were mixed in an agate mortar and compacted for 10 minutes with a 10 ton load in a 1.3 cm diameter. In the second preparation route, the PPY polymer and KOH were mixed and not compacted. The compaction was done to reduce the inter-particle voids prior to the thermochemical treatment. Both samples were then carbonized at 800 °C under nitrogen gas flow for 1 hour. The products were then washed with 10 wt.% hydrochloric acid (HCl) and rinsed with deionized water (DI) until a pH of 7.0 was obtained before being dried at 120 °C for 3 hours. The compacted carbon sample was found to have a higher specific surface area and pore volume of 4000 $m^2 \cdot g^{-1}$ and 3.0 $cm^3 \cdot g^{-1}$ respectively. The compacted sample also had an increase in its hydrogen storage capability from 7.4 wt% to 9.6 wt%.

Studies done by Peng et al. [5] involved a report where waste tea-leaves were used as the precursor in the preparation of activated carbon and KOH was the activating agent used in the carbonization process. The material was carbonized in the CVD system at 800 °C in a nitrogen atmosphere for 1 hour. The obtained product had a specific surface area in the range of 2245 $m^2 \cdot g^{-1}$ to 2841 $m^2 \cdot g^{-1}$ with a corresponding specific capacitance of 330 $F \cdot g^{-1}$ at a specific current of 1.0 $A \cdot g^{-1}$ in a KOH electrolyte. The product had an electrochemical cycle stability of approximately 92% after 2000 cycles.

Bello et al. [34] synthesised activated carbon from pine cone having included a hydrothermal synthesis step. The pine cone was activated with potassium hydroxide (KOH), having employed the compactivation technique, the sample was then carbonized at a temperature of 800 °C for one hour. The product had a specific surface area of 1515 $m^2 \cdot g^{-1}$, specific capacitance and energy density of 137 $F \cdot g^{-1}$ and 19 $Wh \cdot kg^{-1}$ were obtained respectively, at a specific current of 1.0 $A \cdot g^{-1}$ having a potential window of 2.0 V in a 1 M sodium sulphate (Na_2SO_4) electrolyte solution.

2.2.4. Activating agents

Recently, alternative activating agents (AAs) have been researched as the most commonly used potassium hydroxide (KOH) pellet has been discovered to pose economic and environmental threats due to its highly alkaline nature which limits its use as an AA in an up-scaled set-up [41].

Rufford et al. activated carbon prepared from sugar bagasse activated with zinc chloride and carbonized at 750 °C and 900 °C for 1 hour under nitrogen gas flow [36]. The specific surface area obtained was greater than 1000 $m^2 \cdot g^{-1}$ with corresponding specific capacitance and energy density of 300 $F \cdot g^{-1}$ and 10 $Wh \cdot kg^{-1}$ at 1.0 $A \cdot g^{-1}$ in the 2 electrode configuration in a 1 M H_2SO_4 electrolyte respectively. (K_2CO_3) and potassium hydrogen carbonate ($KHCO_3$) have also been investigated as AAs since they are better environmental friendly alternatives [41].

The effect of the activating agent in the synthesis of activated carbon was observed in the studies by Tay et al. [8]. Soybean oil cakes were activated with KOH and K_2CO_3 with subjection to carbonization in a CVD system using nitrogen gas at a temperature of 800 °C for 1 hour. The sample activated with K_2CO_3 was found to have a higher porosity, pore volume and a specific surface area of 1352.88 $m^2 \cdot g^{-1}$ compared to 643 $m^2 \cdot g^{-1}$ from using KOH [8, 41]. This study demonstrated the suitability of a less toxic alternative activating agents which yield equally porous materials.

Carvalho et al. [42] synthesised activated carbon from cork waste. In their work, the cork was activated with K_2CO_3 with varying weight ratios for K_2CO_3: cork of 1:1 and 5:1 respectively. The sample was then carbonized using a horizontal tube furnace in a nitrogen atmosphere at 800 °C for 1 hour. Thereafter, the sample was rinsed with DI water to a pH of 7.0 and dried at 100 °C. The obtained activated carbon product was cylindrical in shape and had a diameter and length of approximately 4 mm and 9 mm respectively. The porosity of the product was found to be independent of the ratio of the activating agent to the raw material. It also contained ultra micropores (width< 0.7nm) and super micropores (0.7 nm< width<2.0 nm). After comparison with his earlier work, Carvalho et al. [43] observed that the carbonization time had decreased to 2 hours from the 7 hours previously taken for carbonization with KOH. Potassium salts assist in the preparation of highly mesoporous materials, increases the sample yield, decreases the preparation time and the ion diffusion distance compared to KOH [41, 42].

PPY was synthesised and activated with KOH at 800 °C for 1 hour in a nitrogen atmosphere as described in the research study done by Bello et al. [7]. The PPY was tested with 3 different electrolytes and exhibited high specific capacitance values in all 3 electrolytes; 131 $F \cdot g^{-1}$ in 1 M Na_2SO_4, 108 $F \cdot g^{-1}$ in 6 M KOH and 94 $F \cdot g^{-1}$ in 1 M sodium nitrate ($NaNO_3$). The PPY material also exhibited a high specific surface area of 2230 $m^2 \cdot g^{-1}$.

2.3. Characterization techniques

2.3.1. Textural characterization

The textural properties of the sample material were analysed using the Brunauer- Emmett- Teller (BET) method as well as the Barrett-Joyner-Halenda method. These methods are used to determine the Specific surface area (SSA) and the pore size distribution of a material respectively [44]. In these techniques, nitrogen at a temperature of approximately 77 K (-196 ˚C) is used to acquire the adsorption energy of materials due to the interactions of dipoles within them [45]. The adsorption and desorption isotherms of the material are then obtained and used to determine the specific surface area, pore size distribution and pore volume of the material in question.

2.3.2. Scanning electron microscopy and Energy dispersive x-ray spectroscopy

In scanning electron microscopy (SEM), an electron beam is used to raster scan an electrically conductive sample material in order to determine the surface morphology, crystal structure and orientation.

Energy dispersive x-ray spectroscopy (EDX) is used to determine the elemental composition of a sample [46, 47]. The sample is subjected to an electron beam which passes through it and causes the sample to generate and emit x-rays that are then used to determine the element that produced them [46, 47].

These processes occur under a high vacuum in the region of 10^{-6} Torr (1.33 x 10^{-6} mBar) or less, in order for the morphology of the sample to be obtained.

Signals are collected from secondary, backscattered electrons and diffracted backscattered electrons as well as photons and x-rays. Secondary electrons are responsible for the morphology of the sample and the backscattered electrons show the discrepancies in the sample composition in the SEM and EDX techniques. The photons are used to determine the elemental analysis of the sample in EDX [46].

Although SEM and EDX are conducted using the same instrument, they require different accelerating voltages to function. SEM requires a low accelerating voltage (1.0 kV – 5.0 kV) as the electrons bombarding the sample from the electron beam only have to excite the electrons located on or close to the surface of the sample. A higher accelerating voltage (10 kV -30 kV) is needed to excite the x-rays which are mostly found in the core levels of the sample.

2.3.3. Transmission electron microscopy

The internal morphology of the sample material can be characterized using the tunnelling/ transmission electron microscopy (TEM) technique. Electrons from an electron beam are accelerated at a high voltage to enable them to be transmitted through the sample [46]. Information of the inner structure of the sample such as the crystal structure, dislocations and grain boundaries can be observed.

2.3.4. Fourier transform infrared spectroscopy

Fourier transform infrared spectroscopy (FTIR) assists in the identification of the functional groups present in the sample [46, 48]. Infrared light is used to observe the chemical properties of the sample, the absorption of the infrared radiation by the sample initiates molecular bond vibrational and or rotational energies which can be observed at different wavelengths [46]. This technique assists in the determination of the molecular and chemical structures in the sample.

2.3.5. Raman spectroscopy

Raman spectroscopy is a non-destructive method adopted to gain insight into the nature of the molecular vibrations present in a material [49]. It is based on the inelastic scattering of monochromatic light, in the visible or near infrared region, from a laser bombarding the sample at a specific power and wavelength [46, 48]. The laser perturbs Raman-active bonds within a specific material which gives a characteristic feedback thereby giving information on the structural properties of the sample.

Raman analysis is a common analysis tool conducted on carbon-based materials such as activated carbon, carbon nanotubes, carbon spheres and graphene. This is due to the Raman-active bonds which exist in carbon-containing materials. The characteristic D-peak and G-peak will always be observed with varying intensity levels. The D-peak which appears at approximately 1360 cm^{-1} in activated carbon gives information about the defects/disorders that are present in the material [50]. The G-peak is observed due to the stretching mode of the graphitic plane caused by the vibrations of the sp^2 carbon atoms [51, 52]. The 2D-peak which appears at a wavenumber of approximately 2700 cm^{-1} gives information about the number of layers that are present in the carbon material, such as graphene [49, 53, 54]. The intensity of the peaks assists in distinguishing between monolayer, bilayer and multilayer graphene [49, 54, 55].

2.3.6. X-ray powder diffraction spectroscopy

X-ray powder diffraction (XRD) is a technique used to classify the crystalline structure of the sample material by determining the purity and unit cell dimensions [55]. The sample is bombarded with x-rays which cause scattering of the electrons within the sample resulting in the observation of maximum and minimum diffraction patterns as well as the intensities [46, 55]. These patterns are only produced when the conditions satisfy Bragg's law.

$$n\lambda = 2d\sin\theta \qquad\qquad\qquad (1)$$

Where λ is the wavelength, θ is the diffraction angle and d is the lattice spacing in the crystal. The 2θ angle range determines all possible diffraction angles of randomly orientated lattices in powder materials, while the lattice spacing allows for the identification of materials as they all have a set of unique d-spacing values [46, 55].

2.3.7. Electrochemical characterization

The electrochemical performance of any material is determined using three unique tests which involve varying the amount of current as a function of the voltage applied from a potentiostat. These tests are cyclic voltammetry (CV), chronopotentiometry (CP), commonly referred to as

galvanostatic charge-discharge (GCD), and electrochemical impedance spectroscopy (EIS). These tests can be performed in both a half-cell (three-electrode) configuration (Fig. 1) and a full-cell (two-electrode) configuration (Fig. 2). In the three-electrode configuration, the electrochemical performance of half-cell electrodes are being investigated whereas in the two-electrode configuration, the electrochemical properties of the complete device are being analysed [47].

2.3.7.1. Cyclic voltammetry

Cyclic voltammetry (CV) is usually the first electrochemical test conducted on a sample material as it assists in the determination of the comfortable operating potential window of the specific material. The shape of the cyclic voltammogram (Fig. 3) assists in determining the nature of the charge storage mechanism present in the material. A rectangular-shaped CV curve is characteristic of a typical electric double layer (EDLC) charge storage mechanism. In some special cases, a rectangular CV plot is also obtained for pseudocapacitive materials such as ruthenium dioxide (RuO_2) and manganese dioxide (MnO_2) materials [56–59]. The CV curve comprising of typical reduction and oxidation (redox) peaks correlates to materials which are characterized by faradaic charge storage mechanism.
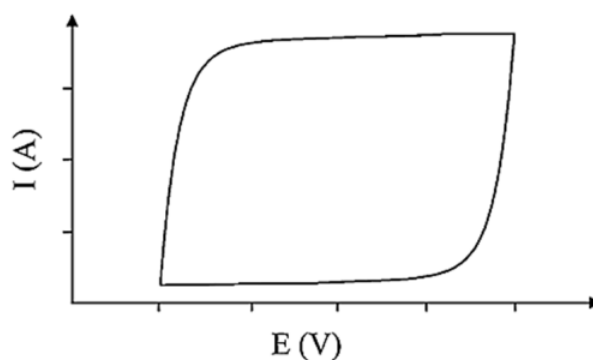
Figure 3: Cyclic voltammogram of a typical EDLC material

2.3.7.2. Galvanostatic charge-discharge

In galvanostatic charge-discharge (GCD) (Fig. 4), the material is repetitively charged and discharged at a constant current within a pre-determined operating potential window range [60].

The resultant plot gives the charging and discharge profile which can be used to determine the capacitance of the material.
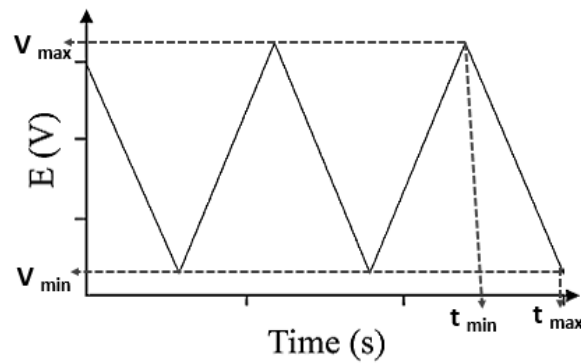
Figure 4: Galvanostatic charge-discharge curve of a typical EDLC material

For EDLC and pseudocapacitive-type materials, the GCD plot is linear for both the charging and discharging steps. The equation used to calculate the specific capacitance (C_s) of the material is given as:

$$C_s = \frac{I\Delta t}{m\Delta V} \tag{2}$$

Where I is the applied current, Δt ($\Delta t = t_{max} - t_{min}$) the discharge time, m the mass of the sample and ΔV ($\Delta V = V_{max} - V_{min}$) is the change in potential.

Whereas for faradic type materials, the charge-discharge profile is more of a polynomial shaped pattern which is anti-linear. As such in faradaic material, the specific capacitance cannot be calculated [61]; instead, the specific capacity of the material is calculated using:

$$C_s = \frac{I\Delta t}{3.6 \cdot m} \tag{3}$$

Ageing tests are conducted on the materials to determine their efficiency on a commercial scale. These tests include floating or ageing commonly known as voltage holding and cyclic ageing test [62]. An increase in the equivalent series resistance and a decrease in the capacitance of the material are usually observed after the ageing test [62].

In the voltage holding ageing test, the voltage applied on the material is kept constant for a period of time to accelerate the reaction taking place between the electrolyte and foreign species within the material [62]. The material is continuously charged and discharged at a high current in the stability test. This is done to emulate the conditions that the material will be subjected to a commercial scale [62].

Self-discharge is the term given to the process in which an electric capacitor experiences a voltage drop while stored in a charged state [63]. The self-discharge response can be determined in both the half-cell and full-cell configurations.

In the half-cell configuration, self-discharge is caused by reduced identification of the ion mobility mechanism, this in turn then causes a self-discharge reaction to occur at the electrode surface [64–66]. More realistic measurements of the self-discharge response of a commercial device are obtained when the self-discharge test is conducted in the full-cell configuration [63–66].

There are three causes of self-discharge namely: Ohmic leakage, charge distribution, and parasitic faradaic reactions.

Ohmic leakage self-discharge is due to a fault in the construction of the full-cell resulting in a resistive pathway between the positive and negative electrodes [63, 67, 68]. When the electrode has been charged up through a series of increasing resistance components, such as solution and ionic resistance, a charge distribution self-discharge tends to occur [67, 68]. The occurrence of redox reactions on the surface of the discharging electrode results in what is referred to as a parasitic faradaic self-discharge response [63, 67, 68].

2.3.7.3. Electrochemical impedance spectroscopy

Electrochemical impedance spectroscopy (EIS) analysis involves the application of a low amplitude alternating voltage to measure the impedance of a power cell as a function of frequency in order to characterize the charge transfer, electrode resistance properties and charge storage mechanism [60]. The Nyquist plot (Fig. 5) for example, is a common plot obtained from the EIS measurement which shows the imaginary impedance ($-Z''$ (Ω)) as a function of the real impedance (Z' (Ω)) at varying frequencies. The solution resistance (R_s), as well as the charge transfer reaction (R_{ct}), also known as the circuit resistance can be obtained from the Nyquist plot.
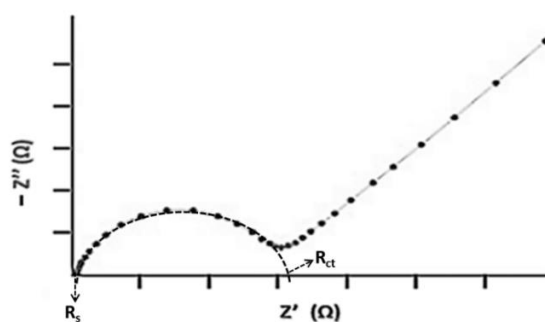
Figure 5: Nyquist plot

2.3.7.4. Half-cell configuration

For the half-cell configuration (figure 1), three types of electrodes are needed, namely the working electrode, counter electrode and reference electrode. The working electrode is made up of the sample material coated on a current collector which provides an interface for charge transfer. The slurry is made up of the sample material and a binder, which is added to hold the sample together, the mixture was held together by adding a few drops of N-methyl-2-pyrrolidone (NMP) and is pasted uniformly onto a current collector. A conductive additive is sometimes added in the preparation of the slurry to counteract the effect of the binder. The current collector should have a high current carrying capacity and be chemically stable.

Materials such as nickel foam, nickel foil, aluminium foil and carbon paper are commonly used as current collectors in the fabrication of electrodes.
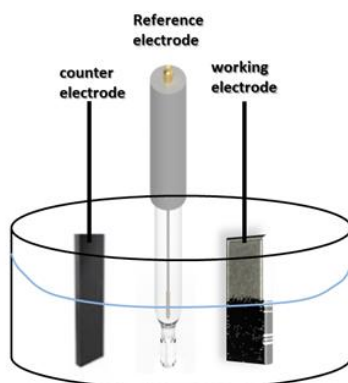
Figure 1: Three-electrode cell configuration

The counter electrode is usually a material that is porous, conductive and does not react with the electrolyte. Glassy carbon (GC) is the commonly used as the counter electrode in the electrochemical characterization of samples. Other counter electrodes used can be activated carbon pellets and graphite rods to name a few.

The purpose of the reference electrode is to determine the potential at the working electrode; silver/silver chloride (Ag/AgCl), mercury/mercury oxide (Hg/HgO), standard calomel electrode (SCE) are examples of some of the common reference electrodes used [47, 69, 70].

2.3.7.5. Full-cell configuration

The set-up of the full-cell configuration (figure 2) is in the form of a coin cell which only has two terminals, hence it is also referred to as two-electrode configuration. It consists of the working and the counter electrode, with the reference electrode being attached the counter electrode. The coin cell is in the form of a metal casing with a negative and positive terminal, consisting of a spring, spacer, separator with the sample material acting as the negative and positive electrode placed on either side of the separator.
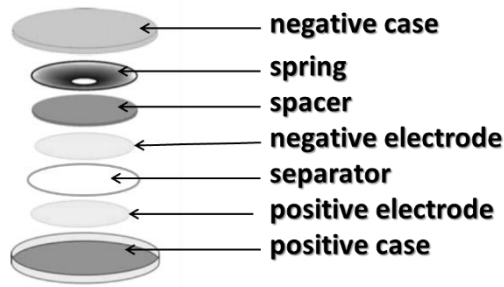
Figure 2: Two-electrode configuration

A full-cell can be classified as a symmetric or an asymmetric (mixed) device. This classification depends on whether or not the same sample material was used for negative and positive electrodes. If the sample material used for the negative and positive electrodes is the same, then the cell is considered to be a symmetric device, if not, it is classified as a mixed device. The negative and positive electrodes are prepared in the same way as the working electrode for the 3-electrode configuration on a coin shaped current collector. For the mixed device charge balancing is required which should be able to lead to the calculation of the masses on both positive and negative electrodes respectively as per the following equation:

$$m_{negative\ electrode} C_{s_{negative\ electrode}} = m_{positive\ electrode} C_{s_{positive\ electrode}} \tag{4}$$

Where $m_{negative\ electrode}$ and $m_{positive\ electrode}$ are the mass of the negative and positive electrodes respectively and $C_{s(negative\ electrode)}$ and $C_{s(positive\ electrode)}$ are the specific capacitance values for the negative and positive electrodes respectively.

References

1. Vollhardt, K.P.C. and Schore, N.E. 2014. *Organic Chemistry; Palgrave version: Structure and Function*. Macmillan International Higher Education.

2. Viculis, L.M., Mack, J.J., Mayer, O.M., Hahn, H.T. and Kaner, R.B. 2005. *Intercalation and exfoliation routes to graphite nanoplatelets*. Journal of Materials Chemistry, 15(9), pp.974-978.

3. Nishihara, H. and Kyotani, T., 2012. *Templated nanocarbons for energy storage. Advanced Materials, 24(33), pp.4473-4498.*

4. Momodu, D., Okafor, C., Manyala, N., Bello, A., ZebazeKana, M.G. and Ntsoenzok, E. 2017. *Transformation of Plant Biomass Waste into Resourceful Activated Carbon Nanostructures for Mixed-Assembly Type Electrochemical Capacitors*. Waste and Biomass Valorization, pp.1-13.

5. Peng, C., Yan, X.B., Wang, R.T., Lang, J.W., Ou, Y.J. and Xue, Q.J. 2013. *Promising activated carbons derived from waste tea-leaves and their application in high performance supercapacitors electrodes*. Electrochimica Acta, 87, pp.401-408.

6. Momodu, D., Madito, M., Barzegar, F., Bello, A., Khaleed, A., Olaniyan, O., Dangbegnon, J. and Manyala, N. 2017. *Activated carbon derived from tree bark biomass with promising material properties for supercapacitors*. Journal of Solid State Electrochemistry, 21(3), pp.859-872.

7. Bello, A., Barzegar, F., Madito, M.J., Momodu, D.Y., Khaleed, A.A., Masikhwa, T.M., Dangbegnon, J.K. and Manyala, N. 2016. *Electrochemical performance of polypyrrole derived porous activated carbon-based symmetric supercapacitors in various electrolytes*. RSC Advances, 6(72), pp.68141-68149.

8. Tay, T., Ucar, S. and Karagöz, S. 2009. *Preparation and characterization of activated carbon from waste biomass*. Journal of Hazardous Materials, 165(1-3), pp.481-485.

9. Marsh, H. and Reinoso, F.R. 2006. *Activated carbon*. Elsevier.

10. Bansal, R.C. and Goyal, M. 2005. *Activated carbon adsorption*. CRC press.

11. Klass, D.L., 1998. *Biomass for renewable energy, fuels, and chemicals*. Elsevier.

12. Hu, B., Wang, K., Wu, L., Yu, S.H., Antonietti, M. and Titirici, M.M., 2010. *Engineering carbon materials from the hydrothermal carbonization process of biomass*. Advanced Materials, 22(7), pp.813-828.

13. Corcho-Corral, B., Olivares-Marín, M., Valdes-Sánchez, E., Fernández-González, C., Macías-García, A. and Gómez-Serrano, V. 2005. *Development of activated carbon using vine shoots (Vitis vinifera) and its use for wine treatment*. Journal of agricultural and food chemistry, 53(3), pp.644-650.

14. Wei, J., Zhou, D., Sun, Z., Deng, Y., Xia, Y. and Zhao, D., 2013. *A controllable synthesis of rich nitrogen‐doped ordered mesoporous carbon for CO_2 capture and supercapacitors*. Advanced Functional Materials, 23(18), pp.2322-2328.

15. Jordá-Beneyto, M., Suárez-García, F., Lozano-Castelló, D., Cazorla-Amorós, D. and Linares-Solano, A. 2007. *Hydrogen storage on chemically activated carbons and carbon nanomaterials at high pressures*. Carbon, 45(2), pp.293-303.

16. De La Casa-Lillo M.A., Lamari-Darkrim F., Cazorla-Amorós D. and Linares-Solano A. 2002. *Hydrogen storage in activated carbons and activated carbon fibers*. J Phys Chem B 106:10930–10934.

17. Agarwal, R.K., Noh, J.S., Schwarz, J.A. and Davini, P. 1987. *Effect of surface acidity of activated carbon on hydrogen storage*. Carbon, 25(2), pp.219-226.

18.   Neuvonen, P.J., Vartiainen, M. and Tokola, O. 1983. *Comparison of activated charcoal and ipecac syrup in prevention of drug absorption*. European journal of clinical pharmacology, 24(4), pp.557-562.

19.   Korpiel, J.A. and Vidic, R.D. 1997. *Effect of sulfur impregnation method on activated carbon uptake of gas-phase mercury*. Environmental science & technology, 31(8), pp.2319-2325.

20.   Liu, W., Vidić, R.D. and Brown, T.D. 1998. *Optimization of sulfur impregnation protocol for fixed-bed application of activated carbon-based sorbents for gas-phase mercury removal*. Environmental Science & Technology, 32(4), pp.531-538.

21.   Zeng, H., Jin, F. and Guo, J. 2004. *Removal of elemental mercury from coal combustion flue gas by chloride-impregnated activated carbon*. Fuel, 83(1), pp.143-146.

22.   Pevida, C., Plaza, M.G., Arias, B., Fermoso, J., Rubiera, F. and Pis, J.J. 2008. *Surface modification of activated carbons for CO_2 capture*. Applied Surface Science, 254(22), pp.7165-7172.

23.   Plaza, M.G., García, S., Rubiera, F., Pis, J.J. and Pevida, C. 2010. *Post-combustion CO_2 capture with a commercial activated carbon: comparison of different regeneration strategies*. Chemical Engineering Journal, 163(1-2), pp.41-47.

24.   Bhatnagar, A., Hogland, W., Marques, M. and Sillanpää, M. 2013. *An overview of the modification methods of activated carbon for its water treatment applications*. Chemical Engineering Journal, 219, pp.499-511.

25.   Rivera-Utrilla, J., Sánchez-Polo, M., Gómez-Serrano, V., Alvarez, P.M., Alvim-Ferraz, M.C.M. and Dias, J.M. 2011. *Activated carbon modifications to enhance its water treatment applications. An overview*. Journal of hazardous materials, 187(1-3), pp.1-23.

26.   Monser, L. and Adhoum, N. 2002. *Modified activated carbon for the removal of copper,*

zinc, chromium and cyanide from wastewater. Separation and purification technology, 26(2-3), pp.137-146.

27. Ruediger, G.A., Pardon, K.H., Sas1, A.N., Godden, P.W. and Pollnitz, A.P. 2004. *Removal of pesticides from red and white wine by the use of fining and filter agents.* Australian Journal of Grape and Wine Research, 10(1), pp.8-16.

28. Yin, J., Zhu, Y., Yue, X., Wang, L., Zhu, H. and Wang, C. 2016. *From environmental pollutant to activated carbons for high-performance supercapacitors.* Electrochimica Acta, 201, pp.96-105.

29. Jain, A., Balasubramanian, R. and Srinivasan, M.P. 2016. *Hydrothermal conversion of biomass waste to activated carbon with high porosity: A review.* Chemical Engineering Journal, 283, pp.789-805.

30. Lillo-Ródenas, M.A., Cazorla-Amorós, D. and Linares-Solano, A. 2003. *Understanding chemical reactions between carbons and NaOH and KOH: an insight into the chemical activation mechanism.* Carbon, 41(2), pp.267-275.

31. Bello, A., Barzegar, F., Madito, M.J., Momodu, D.Y., Khaleed, A.A., Olaniyan, O., Masikhwa, T.M., Dangbegnon, J.K. and Manyala, N. 2017. *Floating of PPY derived carbon based symmetric supercapacitor in alkaline electrolyte.* ECS Transactions, 75(24), pp.1-12.

32. Chmiola, J., Yushin, G., Dash, R. and Gogotsi, Y. 2006. *Effect of pore size and surface area of carbide derived carbons on specific capacitance.* Journal of Power Sources, 158(1), pp.765-772.

33. Chmiola, J., Largeot, C., Taberna, P.L., Simon, P. and Gogotsi, Y. 2008. *Desolvation of ions in subnanometer pores and its effect on capacitance and double‑layer theory.* Angewandte Chemie International Edition, 47(18), pp.3392-3395.

34. Bello, A., Manyala, N., Barzegar, F., Khaleed, A.A., Momodu, D.Y. and Dangbegnon, J.K. 2016. *Renewable pine cone biomass derived carbon materials for supercapacitor application*. RSC Advances, 6(3), pp.1800-1809.

35. Fasakin, O., Dangbegnon, J.K., Momodu, D.Y., Madito, M.J., Oyedotun, K.O., Eleruja, M.A. and Manyala, N. 2018. *Synthesis and characterization of porous carbon derived from activated banana peels with hierarchical porosity for improved electrochemical performance*. Electrochimica Acta, 262, pp.187-196.

36. Rufford, T.E., Hulicova-Jurcakova, D., Khosla, K., Zhu, Z. and Lu, G.Q. 2010. *Microstructure and electrochemical double-layer capacitance of carbon electrodes prepared by zinc chloride activation of sugar cane bagasse*. Journal of Power Sources, 195(3), pp.912-918.

37. Momodu, D.Y., Madito, M.J., Barzegar, F., Masikhwa, T.M., Ugbo, F., Khaleed, A.A., Bello, A., Dangbegnon, J.K. and Manyala, N. 2016. *Activated carbon derived from tree bark biomass for high performance electrochemical capacitors*. In Meeting Abstracts (No. 7, pp. 984-984). The Electrochemical Society.

38. Sevilla, M. and Fuertes, A.B. 2009. *The production of carbon materials by hydrothermal carbonization of cellulose*. Carbon, 47(9), pp.2281-2289.

39. Wang, Q., Li, H., Chen, L. and Huang, X. 2001. *Monodispersed hard carbon spherules with uniform nanopores*. Carbon, 39(14), pp.2211-2214.

40. Adeniran, B. and Mokaya, R. 2015. *Compactivation: a mechanochemical approach to carbons with superior porosity and exceptional performance for hydrogen and CO_2 storage*. Nano Energy, 16, pp.173-185.

41. Sevilla, M. and Fuertes, A.B. 2016. *A Green Approach to High‐Performance Supercapacitor Electrodes: The Chemical Activation of Hydrochar with Potassium*

Bicarbonate. ChemSusChem, 9(14), pp.1880-1888.

42. Carvalho, A.P. 2004. *Activated Carbons from Cork Waste by Chemical Activation with K₂CO₃, Application to Adsorption of Natural Gas Components*. Carbon, 42(3), pp.672-674.

43. Carvalho, A.P., Cardoso, B., Pires, J. and de Carvalho, M.B. 2003. *Preparation of activated carbons from cork waste by chemical activation with KOH*. Carbon, 14(41), pp.2873-2876.

44. Sing, K. 2001. *The use of nitrogen adsorption for the characterisation of porous materials. Colloids and Surfaces A: Physicochemical and Engineering Aspects*. 187, pp.3-9.

45. Brunauer, S., Emmett, P.H. and Teller, E. 1938. *Adsorption of gases in multimolecular layers*. Journal of the American chemical society, 60(2), pp.309-319.

46. Skoog, D.A., Holler, F.J. and Crouch, S.R. 2007. *Instrumental analysis* (pp. 477-8). Belmont: Brooks/Cole, Cengage Learning.

47. Settle, F.A. 1997. *Handbook of instrumental techniques for analytical chemistry*. Prentice Hall PTR.

48. Wade L.G. 2003. *Organic chemistry*. 5th ed. New Jersey

49. Graves, P.R. and Gardiner, D.J. 1989. *Practical Raman Spectroscopy*

50. Yang, C., Hu, X., Wang, D., Dai, C., Zhang, L., Jin, H. and Agathopoulos, S. 2006. *Ultrasonically treated multi-walled carbon nanotubes (MWCNTs) as PtRu catalyst supports for methanol electrooxidation*. Journal of Power Sources, 160(1), pp.187-193.

51. Kim, W.S., Moon, S.Y., Bang, S.Y., Choi, B.G., Ham, H., Sekino, T. and Shim, K.B. 2009. *Fabrication of graphene layers from multiwalled carbon nanotubes using high dc*

pulse. Applied Physics Letters, 95(8), p.083103.

52. Cançado, L.G., Takai, K., Enoki, T., Endo, M., Kim, Y.A., Mizusaki, H., Jorio, A., Coelho, L.N., Magalhaes-Paniago, R. and Pimenta, M.A. 2006. *General equation for the determination of the crystallite size L_a of nanographite by Raman spectroscopy*. Applied Physics Letters, 88(16), p.163106.

53. Pimenta, M.A., Dresselhaus, G., Dresselhaus, M.S., Cancado, L.G., Jorio, A. and Saito, R. 2007. *Studying disorder in graphite-based systems by Raman spectroscopy*. Physical chemistry chemical physics, 9(11), pp.1276-1290.

54. Sadezky, A., Muckenhuber, H., Grothe, H., Niessner, R. and Pöschl, U. 2005. *Raman microspectroscopy of soot and related carbonaceous materials: spectral analysis and structural information*. Carbon, 43(8), pp.1731-1742.

55. B. D. Cullity. 1978. *Elements of x-ray diffraction*, 2nd Ed. Addison Wesley publication Company Inc.

56. Patake, V.D. and Lokhande, C.D. 2008. *Chemical synthesis of nano-porous ruthenium oxide (RuO₂) thin films for supercapacitor application*. Applied Surface Science, *254*(9), pp.2820-2824.

57. Hu, C.C., Chang, K.H., Lin, M.C. and Wu, Y.T. 2006. *Design and tailoring of the nanotubular arrayed architecture of hydrous RuO₂ for next generation supercapacitors*. Nano letters, 6(12), pp.2690-2695.

58. Gujar, T.P., Shinde, V.R., Lokhande, C.D., Kim, W.Y., Jung, K.D. and Joo, O.S. 2007. *Spray deposited amorphous RuO₂ for an effective use in electrochemical supercapacitor*. Electrochemistry Communications, 9(3), pp.504-510.

59. Amade, R., Jover, E., Caglar, B., Mutlu, T. and Bertran, E. 2011. *Optimization of MnO₂/vertically aligned carbon nanotube composite for supercapacitor application*.

Journal of Power Sources, 196(13), pp.5779-5783.

60.   Zhang, S. and Pan, N., 2015. *Supercapacitors performance evaluation. Advanced Energy Materials, 5(6), p.1401401.*

61.   Brousse, T., Bélanger, D. and Long, J.W. 2015. *To be or not to be pseudocapacitive?.* Journal of The Electrochemical Society, 162(5), pp.A5185-A5189.

62.   German, R., Sari, A., Venet, P., Ayadi, M., Briat, O. and Vinassa, J.M. 2014. *Prediction of supercapacitors floating ageing with surface electrode interface based ageing law.* Microelectronics Reliability, 54(9-10), pp.1813-1817.

63.   Andreas, H.A. 2015. *Self-discharge in electrochemical capacitors: a perspective article.* Journal of The Electrochemical Society, 162(5), pp.A5047-A5053.

65.   Kazaryan, S.A., Kharisov, G.G., Litvinenko, S.V. and Kogan, V.I. 2007. *Self-Discharge Related to Iron Ions and its Effect on the Parameters of HES $PbO_2/H_2SO_4/C$ Systems.* Journal of The Electrochemical Society, 154(8), pp.A751-A759.

66.   Kazaryan, S.A., Litvinenko, S.V. and Kharisov, G.G. 2008. *Self-discharge of heterogeneous electrochemical supercapacitor of $PbO_2/H_2SO_4/C$ related to manganese and titanium ions.* Journal of the Electrochemical Society, 155(6), pp.A464-A473.

67.   Conway, B.E., Birss, V. and Wojtowicz, J. 1997. *The role and utilization of pseudocapacitance for energy storage by supercapacitors.* Journal of Power Sources, 66(1-2), pp.1-14.

68.   Niu, J., Pell, W.G. and Conway, B.E. 2006. *Requirements for performance characterization of C double-layer supercapacitors: Applications to a high specific-area C-cloth material.* Journal of Power Sources, 156(2), pp.725-740.

69.   Ricketts, B.W. and Ton-That, C. 2000. *Self-discharge of carbon-based supercapacitors*

with organic electrolytes. Journal of Power Sources, 89(1), pp.64-69.

70. Inagaki, M., Konno, H. and Tanaike, O. 2010. *Carbon materials for electrochemical capacitors*. Journal of power sources, 195(24), pp.7880-7903.

71. Weingarth, D., Czekaj, I., Fei, Z., Foelske-Schmitz, A., Dyson, P.J., Wokaun, A. and Kötz, R. 2012. *Electrochemical stability of imidazolium based ionic liquids containing cyano groups in the anion: a cyclic voltammetry, XPS and DFT study*. Journal of The Electrochemical Society, 159(7), pp.H611-H615.

CHAPTER 3

EXPERIMENTAL PROCEDURE

In this chapter, the experimental procedures used in the preparation and synthesis of the activated carbon material from both polypyrrole and biomass are detailed. The materials used include dried hibiscus calyces, iron(III)chloride (CAS number: 7705-08-0), pyrrole monomer (CAS number: 109-97-7), potassium carbonate anhydrous (CAS number: 584-08-7), potassium hydrogen carbonate (CAS number: 298-14-6), sulphuric acid (CAS number: 7664-93-9), hydrochloric acid (CAS number: 7647-01-0) and potassium nitrate (CAS number: 7757-79-1).

3.1.   Sample preparation

3.1.1.   Hydrothermal treatment of biomass hibiscus calyces

5 g of raw biomass material (dried hibiscus calyces) was mixed with a sulphuric acid (H_2SO_4) solution with a concentration of 0.22 M in a 250 mL beaker. The mixture was stirred for several minutes using a magnetic stirrer before it was transferred into a teflon lined autoclave. The autoclave was placed in an electric oven at a temperature of 160 °C for a fixed period of 12 hours. No further studies was done for other residence times in this study. Subsequently, the autoclave was removed and cooled to room temperature. The product was then filtered using filter paper and rinsed with DI water to obtain a neutral pH. The final product was then dried in the oven at 60 °C for 12 hours and named hydro-thermalized hibiscus calyces (HHL).

3.1.2.   Synthesis of activated carbon from biomass hibiscus calyces using potassium hydrogen carbonate (KHCO3)

The HHL powder was initially mixed with potassium hydrogen carbonate ($KHCO_3$) activating agent (AA) in a ratio of 1:1 by mass for the AA: HHL and mildy compactivated to make a mould.

Afterwards, the mixture was placed in a chemical vapour deposition (CVD) system to undergo carbonization at 850 °C with a ramping rate of 5 °C min^{-1} under 300 sccm of argon gas flow for 1 hour. After which, the CVD system was allowed to cool down to room temperature with the gas continuously flowing. The as-obtained sample was then immersed in 20 mL of 1 M hydrochloric acid (HCl) in a 100 mL beaker sealed with polyfilm for 10 hours to remove any traces of unreacted AA and rinsed thoroughly with deionized water by filtration to obtain a neutral pH. The final washed sample was then dried in the oven at 60 °C for 12 hours. This carbonization procedure was also repeated using the same HHL material for 2 hours and 4 hours respectively to study the effect of carbonization time on pore activation/evolution in the sample. The as-obtained final samples were labelled as HTAC-1, which corresponds to hydrothermal activated carbon activated with $KHCO_3$ with a carbonization time of 1 hour. Similarly, the other final samples were labelled HTAC-2 and HTAC-4. Furthermore, in order to also optimize the synthesis procedure for obtaining highly porous nanostructures, control samples were also prepared in which dried hibiscus calyces which were not subjected to a pre-hydrothermal treatment were also carbonized with the same amount of AA. These samples were also labelled as NHTAC-1, which corresponds to non-hydrothermal activated carbon activated with $KHCO_3$ with a carbonization time of 1 hour. Similarly, the other final samples were labelled, NHTAC-2, and NHTAC-4 for the same carbonization times. The synthesis process for the activated carbon is outlined in figure 6.

Figure 6: Schematic of the experimental procedure followed in the preparation of the HTAC samples.
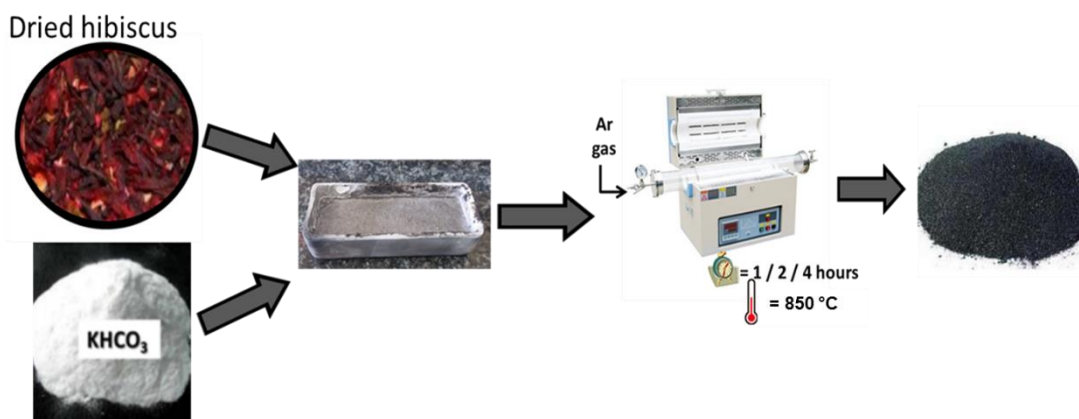
Figure 7: Schematic of the experimental procedure followed in the preparation of the NHTAC samples.

3.1.3. Preparation of polypyrrole (PPY) polymer

2.4 g of iron(III) chloride ($FeCl_3$) was dissolved in a 250 mL beaker containing 50 mL deionized water and stirred for 30 minutes using a magnetic stirrer. Thereafter, 0.5 mL of pyrrole monomer was then added slowly while continuously stirring for 12 hours. The product was then washed continuously with deionized water to eliminate the acidic by-products through filtration until a neutral pH was obtained. An electric oven (set to 80 °C) was used to dry the sample over 24 hours (total time).

3.1.4. Synthesis of activated carbon from polypyrrole (PPY) precursor

The PPY powder was mixed with potassium carbonate anhydrous (K_2CO_3) activating agent (AA) in different K_2CO_3: PPY mass ratios denoted as 0:1, 2:1, 4:1, 6:1 and 8:1, respectively and mildy compactivated. Each sample was then carbonized for 2 hours at 800 °C with a ramping rate of ca. 5 °C min^{-1} in the presence of argon gas. The activated carbon was then immersed in 1 M HCl to remove the remaining unreacted salts and continuously rinsed with deionized water (DI) to attain a neutral pH. The sample was then dried in the oven at 60 °C for 12 hours. The final samples were labelled as AC-PPY-0, AC-PPY-2, AC-PPY-4, AC-PPY-6 and AC-PPY-8 to denote the amount of AA used.

3.2. Material characterization

3.2.1. Brunauer–Emmett–Teller (BET) porosity technique

The Brunauer–Emmett–Teller (BET) method was used to obtain the material textural characteristics which include surface area measurements, pore size and pore volume on a Micromeritics TriStar II 3020 pore analyser. 200 mg of the sample was weighed and degassed at 140 °C for 12 hours at a pressure of 0.8 mbar (~500 mTorr) to eliminate any traces of moisture present. The degassed samples were transferred to the main analysis chamber operated at -196 °C (77 K) within a relative pressure (P/P_o) range of 0.01-1.0. The pore size distribution (PSD) study was done by analysing the desorption branch of the nitrogen-sorption isotherm for the samples using the Barrett-Joyner-Halenda (BJH) method.

3.2.2. Scanning electron microscopy (SEM) technique

The surface morphology of the as-synthesized samples was analyzed using a Zeiss Ultra Plus 55 field emission scanning electron microscope operated at an accelerating voltage of 2.0 kV. The samples were prepared for characterization by placing a small specimen of the sample onto double-sided carbon tape which was set on an aluminium stud.

3.2.3. Transmission electron microscopy (TEM)

A JOEL JEM-2100F microscope was used to obtain the morphology of the samples using the transmission electron microscopy (TEM) technique operated at 200 keV. The samples for TEM analysis were prepared by dispersing the powder material in a 100% ethanol solvent with a sonication step added to evenly disperse any agglomerated particles. The solution mixture with a uniformly dispersed material was then placed onto a carbon-coated copper grid using a micropipette and dried for 30 minutes before being loaded into the TEM system for analysis.

3.2.4. Energy dispersive X-ray spectroscopy (EDX)

The elemental composition was determined using energy dispersive X-ray spectroscopy (EDX) technique. This was done using the Zeiss Ultra Plus 55 scanning electron microscope at an operating voltage of 20.0 kV. The EDX component is incorporated into the SEM system with a detector to analyse the x-ray emissions which occur as a result of the rearrangement of electrons within the energy levels from the material under study. This gives information about the signatory element on the sample surface. The sample was immersed in resin and dried in an electric oven at 60 °C for 24 hours. The resin was then smoothened by polishing with multiple sand papers of 1200 grit, 800 grit, 400 grit and 200 grit roughness.

3.2.5. Fourier transform infrared spectroscopy (FTIR)

The FTIR spectra of samples were measured and recorded using a Bruker Vertex 77v Fourier Transform-Infrared spectrometer which was controlled using Opus 7.0 spectroscopy software. The vibrational modes were examined at wavenumbers ranging from 500 to 4000 cm^{-1}.

3.2.6. Raman spectroscopy

The Raman spectra for the samples were obtained using a WITec alpha300 RAS+ confocal Raman microscope system. The spectra were focused and obtained using a 50X objective lens, at an operating wavelength of 532 nm, 50 mW power and a raster scan rate of 5 seconds.

3.2.7. X-ray powder diffraction (XRD)

The X-ray diffraction for the samples was obtained using an XPERT-PRO diffractometer in a $\theta/2\theta$ configuration with a cobalt tube at 35 KV and 50 mA.

3.2.8. Electrochemical characterization

Electrochemical analysis of the sample electrodes was done on a VMP300 15-channel Bio-logic potentiostat in both three-electrode (half-cell) and two-electrode (full-cell) configurations. The three electrode measurements, namely cyclic voltammetry, chronopotentiometry and electrochemical impedance spectroscopy, were performed to obtain the optimum operating conditions and charge storage behaviour for the half-cell electrode. Thereafter, using the information obtained from the three-electrode tests, full devices were designed and fabricated in a coin cell set-up using 2025. In the half-cell set-up, an Ag/AgCl (3 M KCl) reference electrode and polished glassy carbon counter electrode was adopted in neutral aqueous electrolytes.

The working electrodes were prepared by mixing the active electrochemically active material with carbon black initially and then polyvinylidene fluoride (PVDF) binder in a mass ratio of 8:1:1. Thereafter, a few drops N-methyl-2-pyrrolidone (NMP) was added to the entire mixture to make a slurry which was homogeneously coated onto nickel-foam graphene (NFG) templates serving as the current collector and dried at 60 °C in an electric oven for 8 hours.

The cyclic voltammetry (CV) measurements were obtained for the materials under study in both negative and positive operating potential windows ranging from -0.9 V to 0.0 V and 0.0 V to 0.9 V at varying scan rates from 10 to 100 mV·s^{-1}.

Chrono-potentiometric (CP) measurements were also measured at varying gravimetric specific current values ranging from 0.5 to 10.0 A·g^{-1}.

Lastly, the electrochemical impedance-spectroscopy (EIS) analysis was run on an open circuit voltage between a frequency range from 10 mHz to 100 kHz. All tests were done with an EC-Lab computer program (v11.02) interfaced with the potentiostat.

CHAPTER 4

RESULTS AND DISCUSSION

4.1. Introduction

In this chapter, the results of the materials prepared, and their characterization as outlined in chapter 3 are discussed. Activated carbon (AC) samples were synthesised and optimized from polypyrrole (PPY) and biomass waste raw materials.

In the sample synthesis of the AC from dried hibiscus calyces, the raw material was optimized by subjecting it to hydrothermal (HT) pre-treatment before being activated with potassium hydrogen carbonate ($KHCO_3$) in a mass ratio of 1:1 thereafter carbonized. These samples were further optimized by varying the carbonization time, the samples were carbonized for 1 hour, 2 hours and 4 hours and were labelled as HTAC-1, HTAC-2 and HTAC-4 denoting the carbonization time. Control samples were also prepared in which dried hibiscus which not subjected to a pre-hydrothermal (NHT) treatment were also carbonized with the same amount of AA. These samples were also labelled as NHTAC-1, NHTAC-2 and NHTAC-4 denoting the carbonization time.

Activated carbon was also synthesised from PPY having used potassium carbonate (K_2CO_3) as an activating agent (AA). The samples were prepared by optimizing the activating agent mass ratio to the PPY material. The AA:PPY ratios considered were 0:1, 2:1, 4:1, 6:1 and 8:1. The as-synthesized samples were denoted as AC-PPY-0, AC-PPY-2, AC-PPY-4, AC-PPY-6 and AC-PPY-8, denoting the mass ratio of the activating agent present.

4.2. Textural properties of activated carbon samples

Figure 8 (a-d) displays the textural properties with the isotherms and pore size distribution plots of the HTAC and NHTAC samples. It is seen from the BET plots that the HTAC-2 and HTAC-4 samples depict a type II isotherm with an H4 hysteresis loop, while the HTAC-1 sample depicted a type II isotherm with an H3 hysteresis loop, which means that the material contains both micropores and mesopores [1]. Furthermore, the BJH curves confirm the presence of micropores and mesopores within the samples. This can be seen with the peaks situated at a pore diameter of ~ 2 nm. The HTAC-1 sample was found to have a higher mesopore volume than the other samples. Table 1 summarizes the BET results obtained and it can be seen that specific surface area and pore volume increased with a decrease in carbonization time for the HTAC samples, with the HTAC-1 sample having the highest specific surface area (SSA) and total pore volume of 1337.95 $m^2 \cdot g^{-1}$ and 1.29 $cm^3 \cdot g^{-1}$ respectively.

For the NHTAC samples, an optimum carbonization time of 2 hours was obtained for the activated carbon material based on the highest recorded specific surface area and pore volume of approximately 909.49 $m^2 \cdot g^{-1}$ and 0.65 $cm^3 \cdot g^{-1}$ respectively. A high SSA and pore volume are essential in energy storage devices as they assist in the charge storage process and are essential for ion mobility within the material [1]. From the acquired BET results, it is evident that the incorporation of the hydrothermal pre-treatment step improved the synthesis of the activated carbon material as it halved the carbonization time required and yielded a sample with higher SSA and pore volume.

Figure 8 (e, f) display the textural properties of the AC-PPY samples with detailed description of the BET and BJH plots. The BET plots were of type II isotherm with an H4 hysteresis loop which verifies the presence of micropores and mesopores as confirmed in the BJH plot.

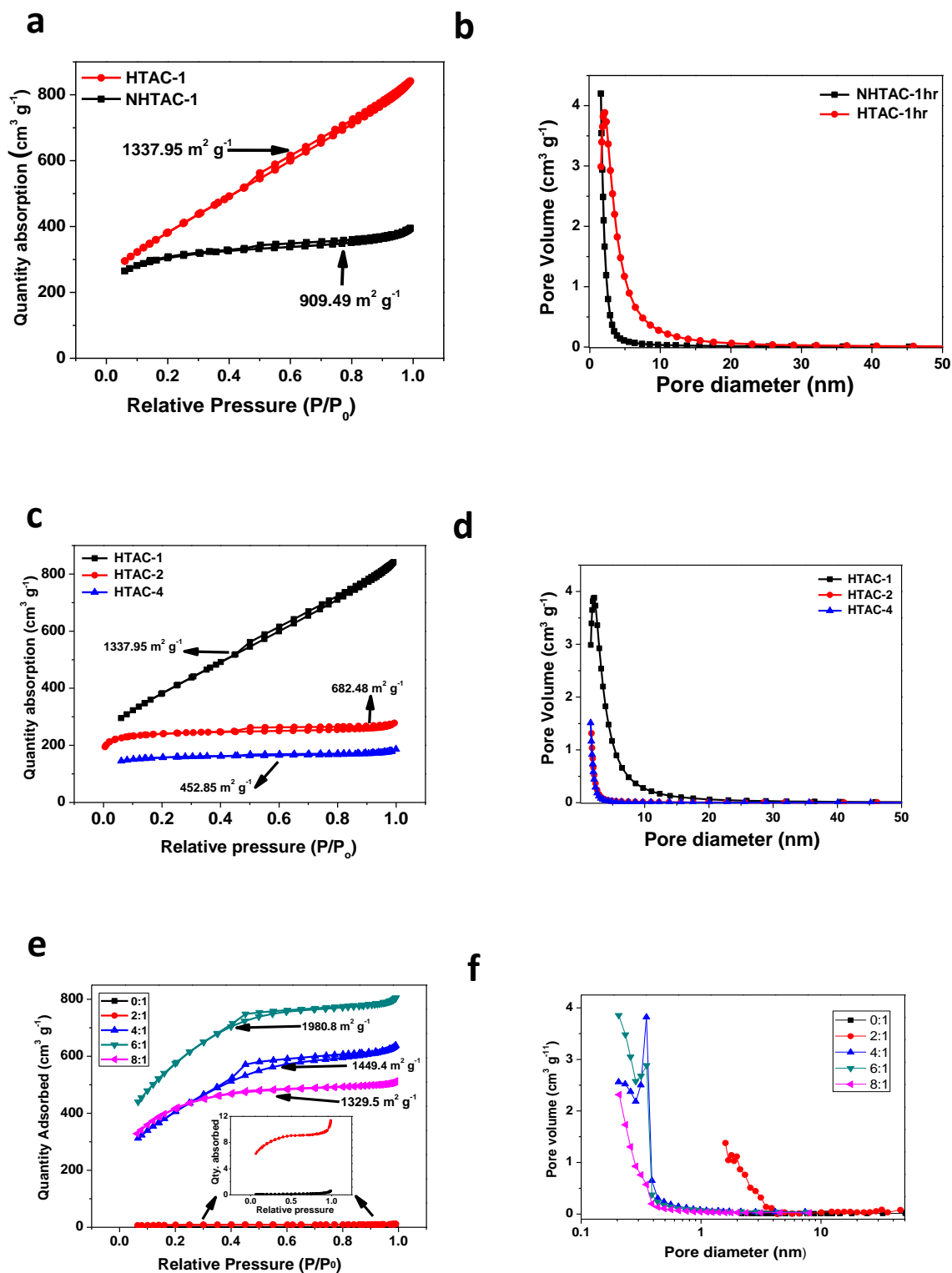**Figure 8:** Textural properties illustrating the (a, b) hydrothermal effect and (c, d) the effect of the carbonization time for HTAC and NHTAC samples and (e, f) textural properties of the AC-PPY samples for different mass ratios of activating agent

The SSA of the AC-PPY samples were found to increase with an increase in the amount of activating agent used to an optimal ratio of 6:1 (AA: PPY) after which it decreased. The highest

41

SSA and corresponding total pore volume obtained for the AC-PPY-6 samples was approximately 1980.80 $m^2 \cdot g^{-1}$ and 1.24 $cm^3 \cdot g^{-1}$ respectively.

The textural properties of all the samples have been summarized in Table 1 and 2.

Table 1: Summary of textural properties of HTAC and NHTAC samples

Sample	Specific surface area (S_{BET}, $m^2 \cdot g^{-1}$)	Total pore volume (V, $cm^3 \cdot g^{-1}$)	Micropore volume (V_{micro}, $cm^3 \cdot g^{-1}$)	Mesopore Volume (V_{meso}, $cm^3 \cdot g^{-1}$)	Average pore diameter (nm)
NHTAC-1	909.49	0.60	0.27	0.34	2.65
HTAC-1	1337.95	1.29	0.01	1.28	3.85
NHTAC-2	1057.28	0.67	0.37	0.30	2.53
HTAC-2	682.48	0.42	0.30	0.12	2.47
NHTAC-4	663.47	0.45	0.18	0.27	2.68
HTAC-4	452.85	0.28	0.18	0.10	2.45

Table 2: Summary of textural properties of AC-PPY samples

Sample	Specific surface area (S_{BET}, $m^2 \cdot g^{-1}$)	Total pore volume (V, $cm^3 \cdot g^{-1}$)	Micropore volume (V_{micro}, $cm^3 \cdot g^{-1}$)	Mesopore Volume (V_{meso}, $cm^3 \cdot g^{-1}$)	Average pore diameter (nm)
AC-PPY-0	7.57	0.02	0.00	0.02	9.82
AC-PPY-2	562.83	0.38	0.06	0.32	2.68
AC-PPY-4	1449.42	0.98	0.02	0.96	2.75
AC-PPY-6	1980.81	1.24	0.03	1.21	2.50
AC-PPY-8	1329.47	0.79	0.14	0.65	2.38

The textural properties of the activated carbon samples displayed in table 1 and table 2 provide a platform for an optimization of the pore structure network. This is achieved via the introduction of a pre-hydrothermal step, variation of the activation time at a fixed carbonization temperature and increment of the activating agent content.

The diverse SSA values and pore volume of the activated carbon samples recorded from the porosity analysis is linked to the nature of the pores present in each material.

In table 1, the reduction in the SSA and associated pore volume with the introduction of the pre-hydrothermal step could be attributed to a saturation of the porous framework with an excessive amount of activating agent. An optimum content of activating agent equal to the raw material is proposed for a considerable activation time in which all existing porosity enhancing material is used up in the specified period of time. Further extension of this time could lead to a destruction of the pore network since the HTAC samples contain less amount of impurities based on the pre-hydrothermal treatment step. This assertion is made in an attempt to initially describe the reason for the observed irregular trend of SSA values observed in table 1. Further in-depth characterization methods are required to fully understand the observed trend.

In table 2, the drop in SSA with increasing quantity of activating agent could be linked to the pore formation and pore growth dynamics. Simply put, excessive amounts of unreacted activating agent leads to an initial pore widening that occurs with possible breakdown of the porous carbon framework [2].

4.3. Electron microscopy investigation on activated carbon samples
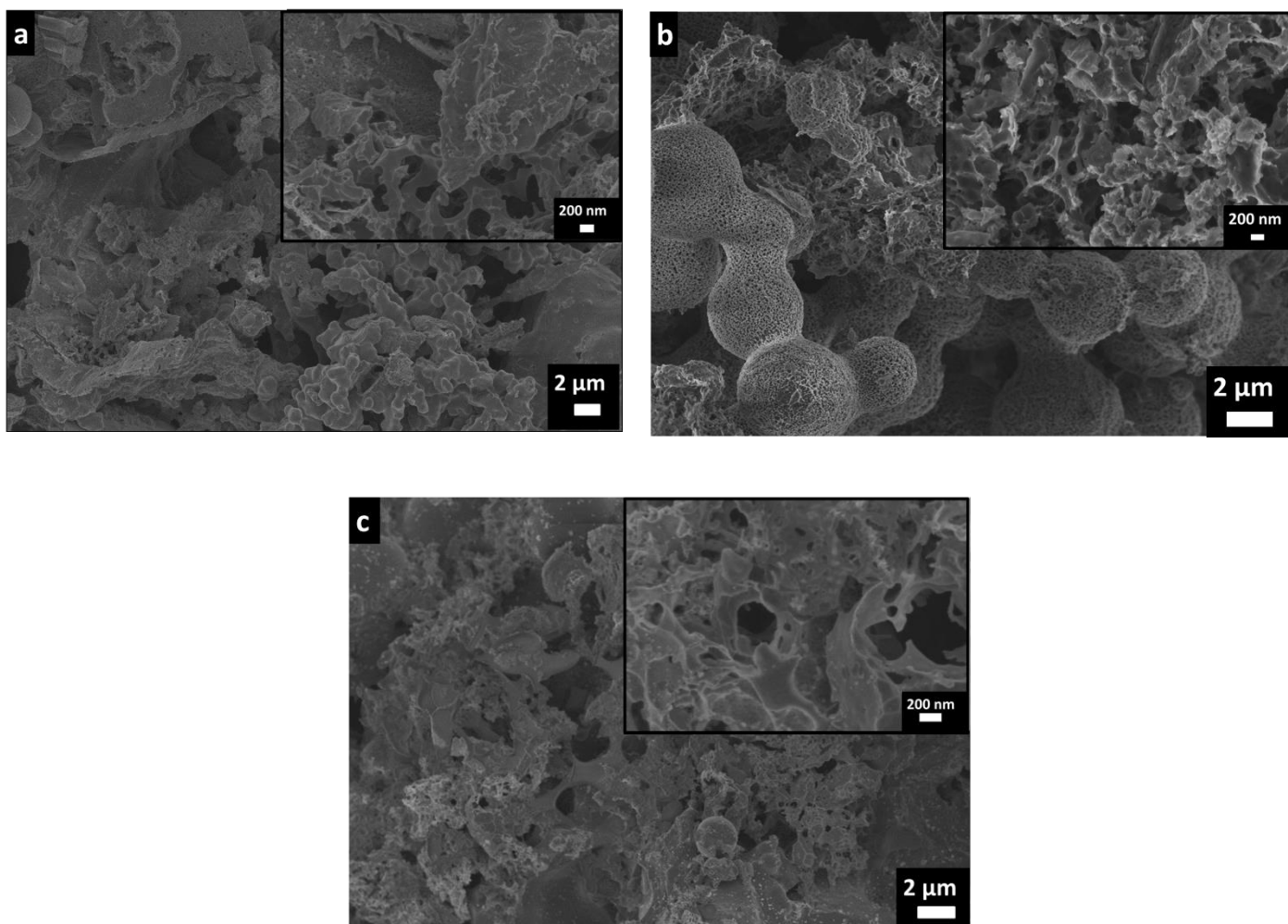
Figure 9: SEM micrographs at low and higher magnifications (inset) of (a) HTAC-1, (b) HTAC-2 and (c) HTAC-4.

Figure 9 shows the SEM micrographs of the HTAC samples. The samples consist of randomly distributed spherical structures composed of interconnected sheet-like structures. The HTAC-1 and HTAC-4 samples also have agglomerated spheres. The presence of these spheres could be due to the pre-treatment step which led to the formation of the observed carbon spheres. Similar occurrences have been reported in earlier studies by Hu et al. [3]. In addition, to further validate this claim, the SEM micrographs of the NHTAC samples (Fig. A1 in the appendix) showed no spherical structures.
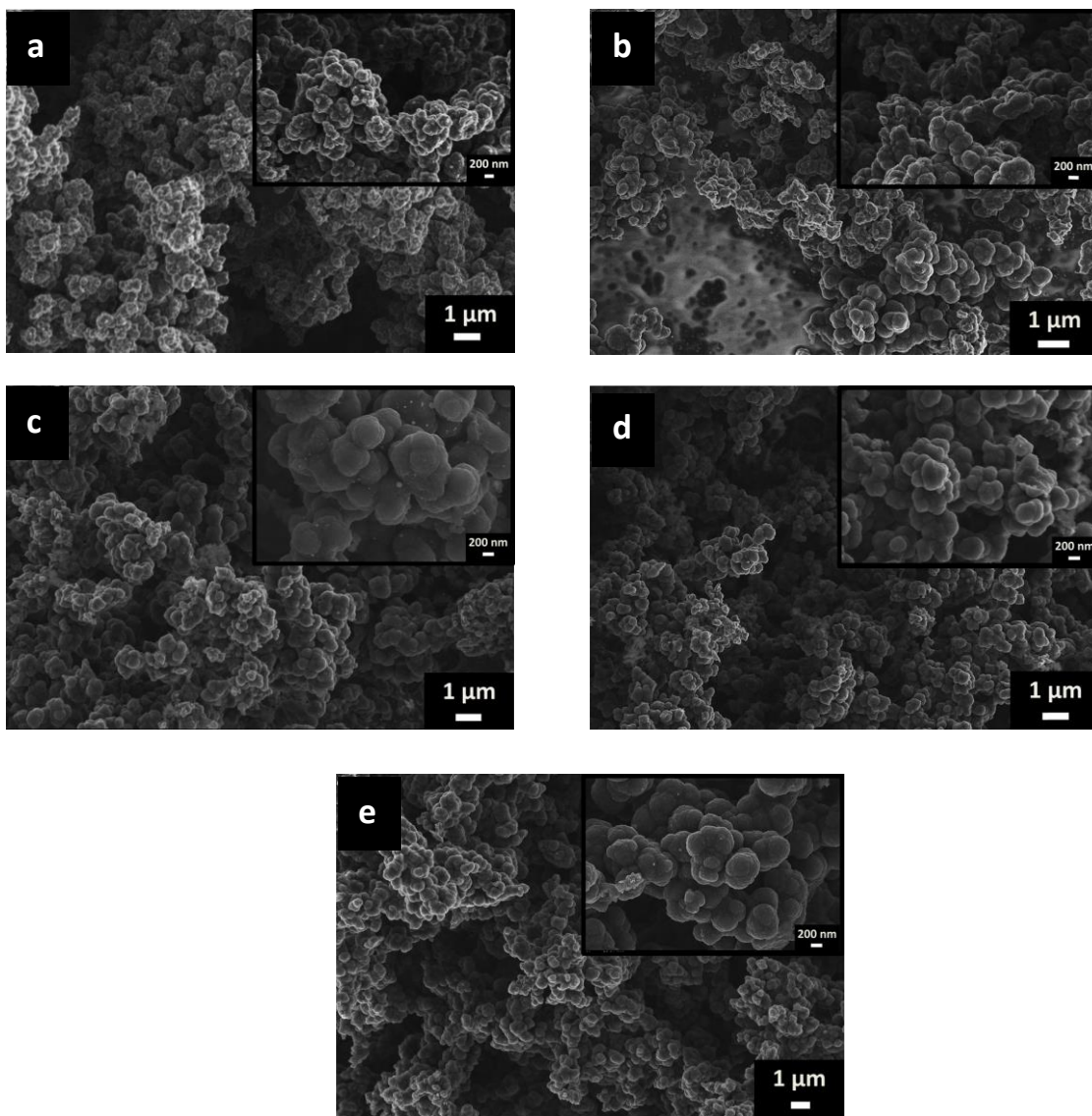
Figure 10: SEM micrographs at low and higher magnifications (inset) of (a) AC-PPY-0, (b) AC-PPY-2, (c) AC-PPY-4, (d) AC-PPY-6 and (e) AC-PPY-8

All three samples were found to contain pores on their surface which corresponds to the observations from the textural characterization. The smaller pores present in the sample could assist in the penetration of electrolyte ions which are essential for charge storage and enhance the electrochemical performance of the material [4]. The SEM micrographs of the AC-PPY samples (Fig. 10) for the different activating agent content depict almost identical morphological characteristics. All samples were composed of porous agglomerated spherical structures with the presence of a sheet-like structure evident in figure 10(b).
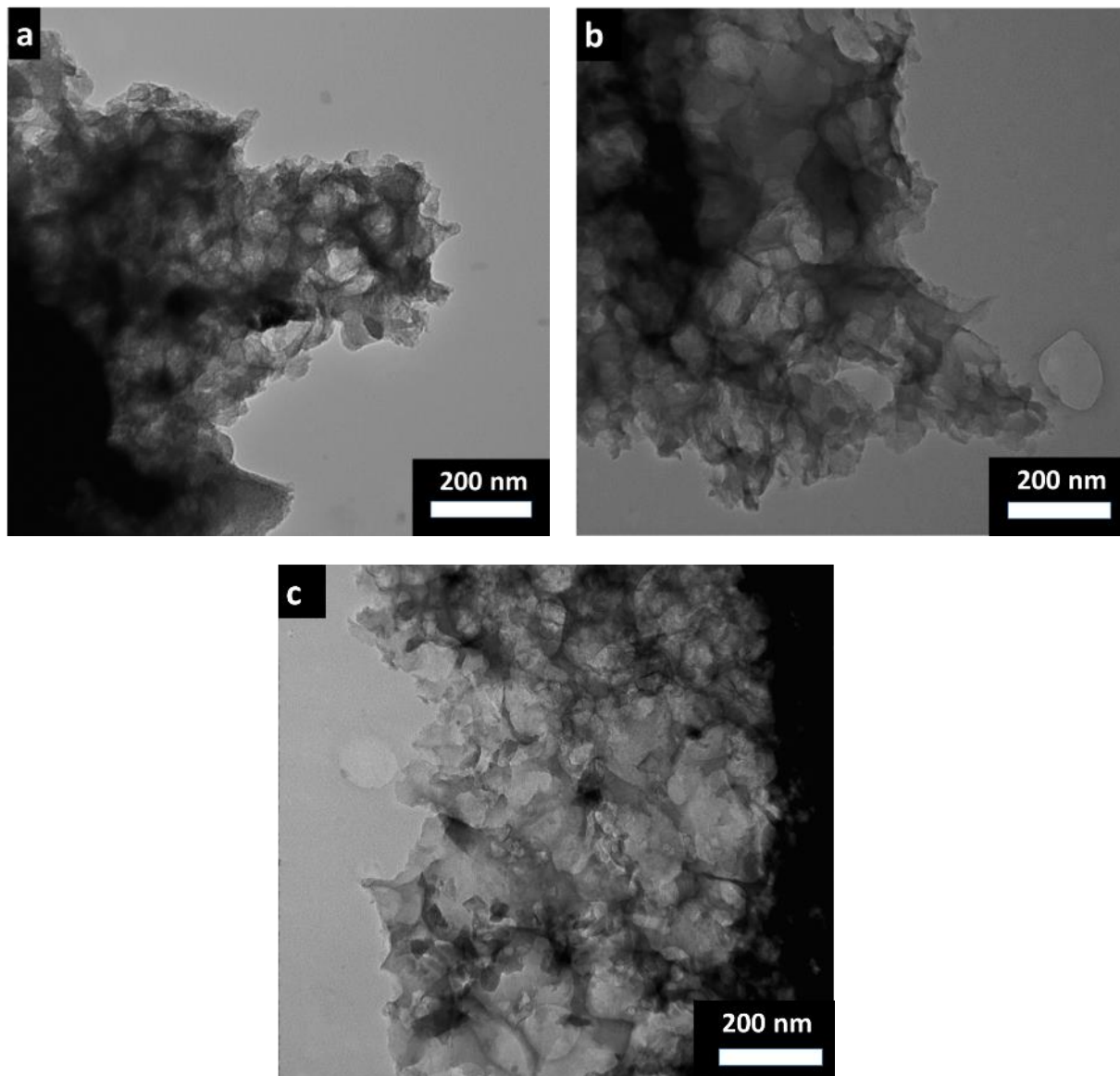
Figure 11: TEM micrographs of (a) HTAC-1, (b) HTAC-2, and (c) HTAC-4 samples

The spheres appear to have become more densely packed with the increase in the AA:PPY ratio. The surface of the spheres provides the necessary site required for charge storage through the interaction of charges with the porous sites. The TEM micrographs (Fig. 11) show interconnected porosity in the HTAC samples which is created by the porosity enhancing agent from the activation procedure adopted [4, 5].
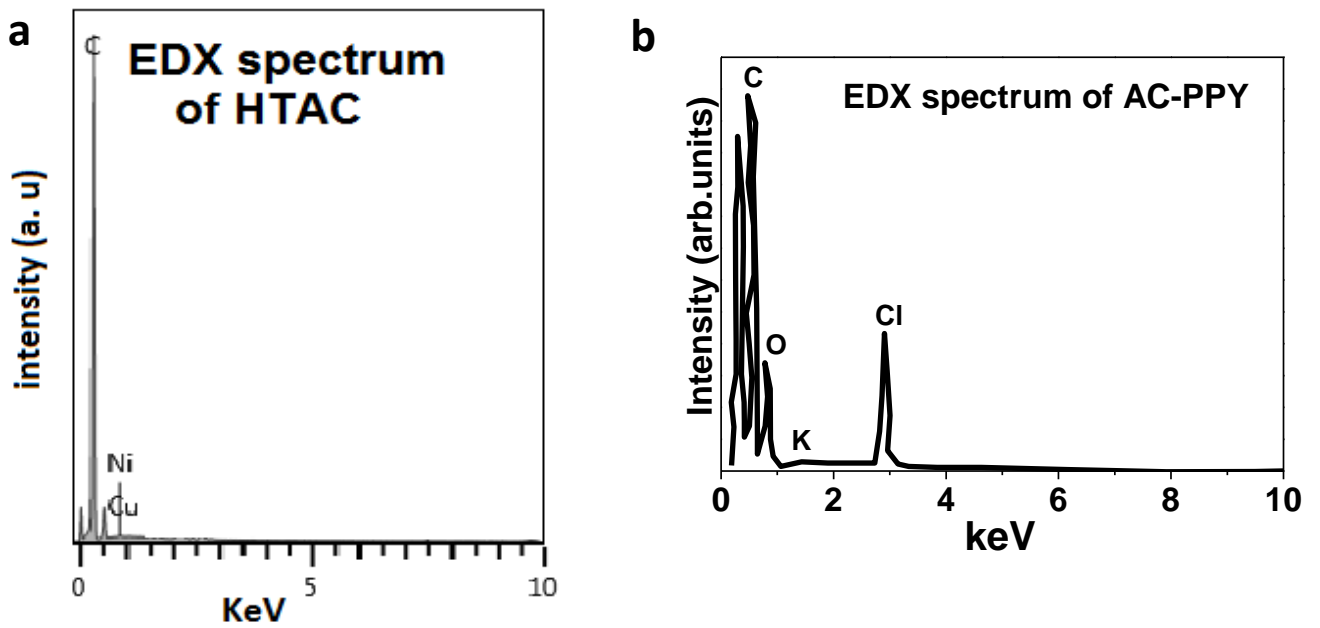
Figure 12: EDX spectra of (a) HTAC and (b) AC-PPY samples

The elemental composition of the activated carbon samples was analysed using EDX (Fig. 12 (a, b)) and it confirmed a high carbon content present within the material in both the HTAC and AC-PPY samples; with traces of nickel and copper in the HTAC samples which could be linked to the composition of the resin. Traces of oxygen, chlorine and potassium were also observed in the AC-PPY samples which was linked to the washing step used in obtaining the final product and removing unreacted activating agents present.

4.4. Vibrational spectroscopic analysis of activated carbon samples
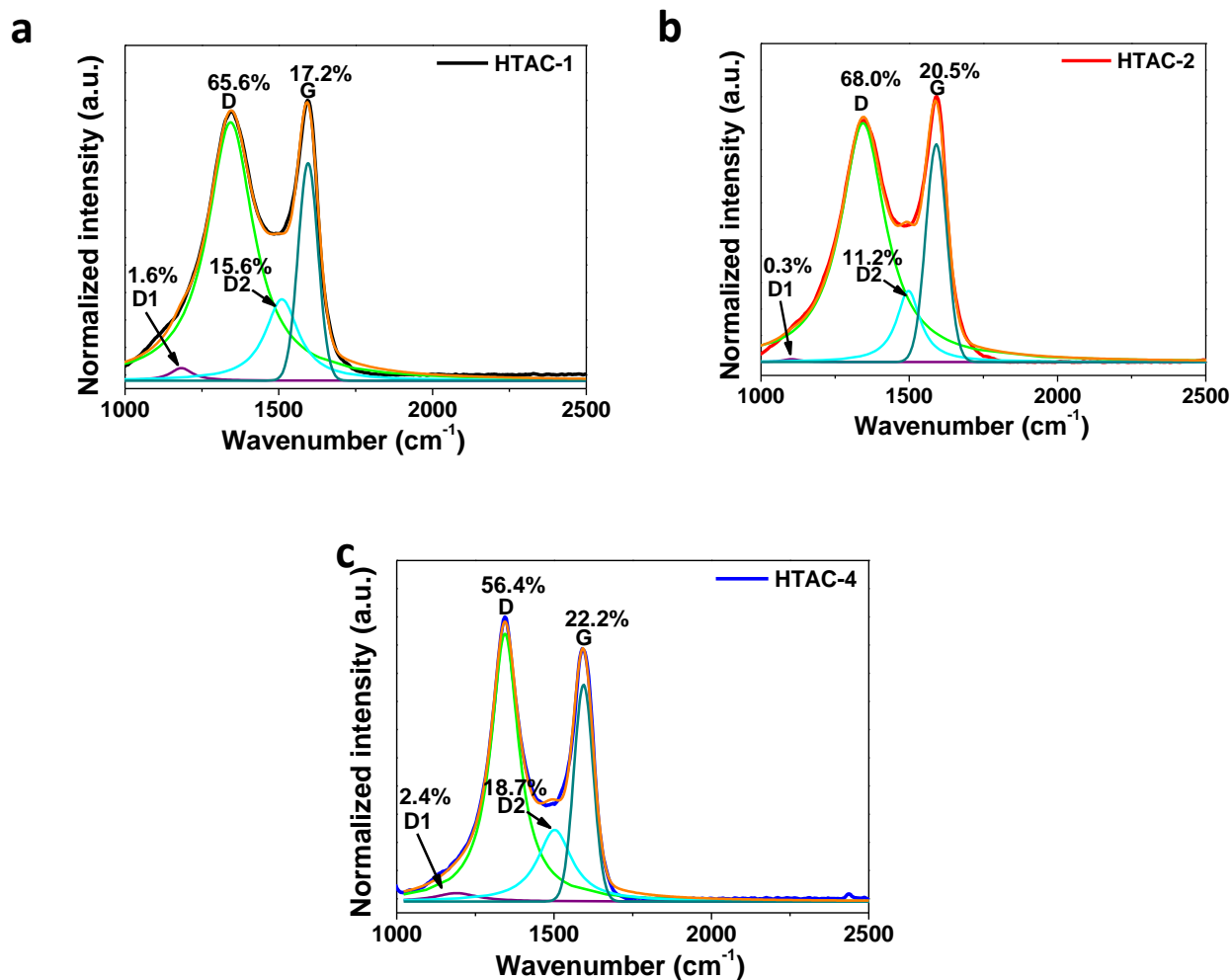
Figure 13: The deconvoluted Raman spectra of the HTAC samples.

Table 3. Raman peaks characteristics for the HTAC samples.

	D FWHM (cm^{-1})	G FWHM (cm^{-1})	D/G	D$_2$/G
HTAC-1	180.87	76.12	3.82	0.91
HTAC-2	182.40	83.06	3.32	0.55
HTAC-4	106.80	72.31	2.51	0.83

Raman analysis was also conducted on the HTAC samples (Fig. 13 (a)), a D- and a G-peaks were observed from the samples which are characteristic of carbon-based materials [4, 6–8].

The presence of the G-peak confirms the graphitic nature of the material which is due to the presence of the sp^2 hybrid bonds within the material while the D-peak gives information about the disorder present within the material as well as the presence of the sp^3-sp^2 bond combination within the material [6, 8–10].

The deconvoluted Raman spectra show the D1- and D2-peaks which correspond to the vibration of the sp^2-sp^3 bonds and amorphous carbon at interstitial sites of the disordered graphitic structure of the carbon material, respectively [6]. The Raman spectra were deconvoluted using a Lorentzian function to obtain the integral areas of the D and G peaks which were used to calculate the fractional percentage contribution of each peak and the ratios listed in table 3. Table 3 displays a higher D/G ratio of disordered carbon relative to the graphitic carbon for HTAC-1. In addition, HTAC-1 shows a higher D2/G ratio of amorphous carbon relative to the graphitic carbon compared to other samples.

Figure 14 depicts the Raman spectra for the AC-PPY samples; a distinct peak observed at 1100 cm^{-1} (*) is linked to the pristine polymer material, however, the intensity of the peak decreases with an increase in amount of activating agent added to the material. D- and G-peaks were observed for all samples except the AC-PPY-0 (non-activated) sample which confirms the carbonaceous nature of the material. The D/G ratios for the activated AC-PPY samples were found to be similar.

From the FTIR analysis conducted, the HTAC samples were found to have the same IR - active bonds regardless of the carbonization time (Fig. 15). The samples were found to have a C-C stretching band at 1050 cm^{-1} as well as a C=C vibrational stretching band at 1600 cm^{-1} [1, 4, 5, 11, 12]. The peak observed at ~2100 cm^{-1} is due to the aliphatic structures (C-H) present within the material [13].
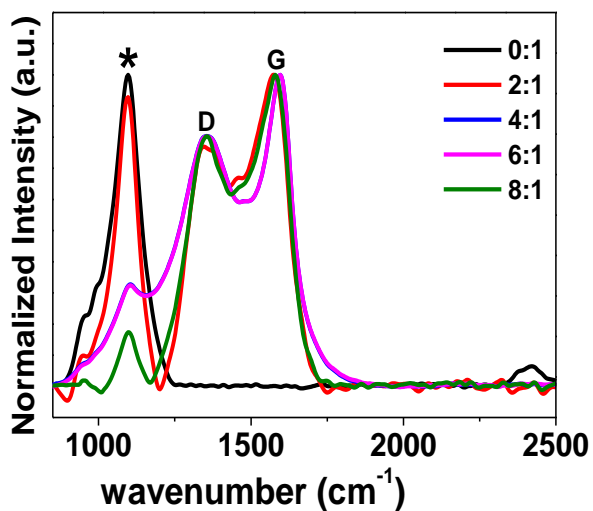
Figure 14: The Normalized Raman spectra of the AC-PPY samples
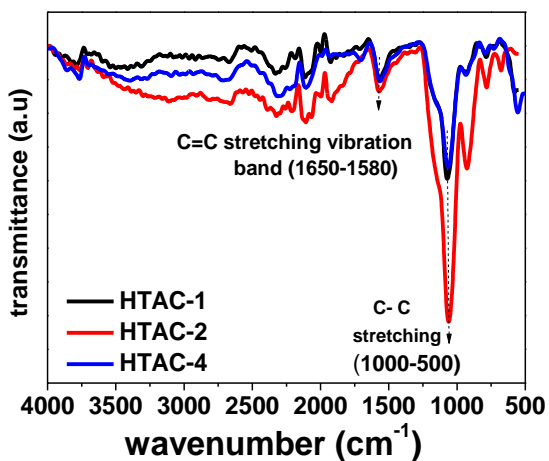
Figure 15: FTIR spectra of HTAC samples

Based on the results obtained from the extensive materials characterization reported so far, further tests involved analysis on the best materials in terms of good textural and structural properties from the BET SSA and the Raman D/G ratios respectively, which correspond to HTAC-1 and AC-PPY-6 samples in this case.

4.5. X-ray diffraction analysis of activated carbon samples
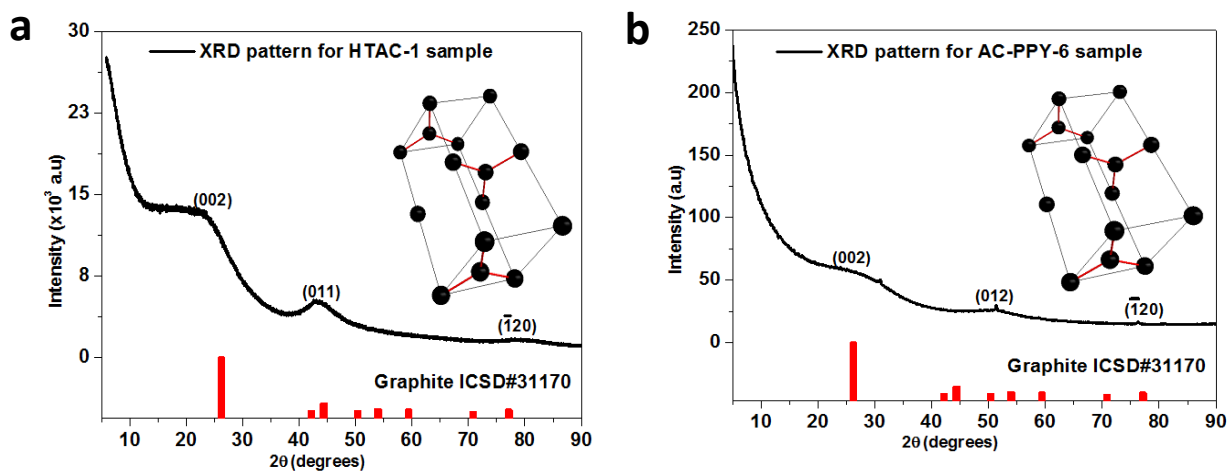
Figure 16: XRD pattern of (a) HTAC and (b) AC-PPY samples

The XRD pattern (as shown in Fig. 16 (a)) of the HTAC-1 samples correlated best with the graphite ICSD card 31170. The sample was found to have an amorphous structure with crystal planes corresponding to (002), (011) and (-120). The presence of the (011) peak at a 2-theta angle of 44° suggests a high disorder within the samples [8].

Similar to the HTAC-1 sample, the AC-PPY-6 sample (Fig. 16 (b)) was also linked to the graphite ICSD card 31170. The sample was found to have an amorphous structure with crystal planes corresponding to (002), (012) and (-120). The variation could be linked to the synthesis procedure adopted and disorder in the material.

4.6. Electrochemical characterization of activated carbon samples

4.6.1. Electrochemical characterization of HTAC samples

The electrochemical performance of the HTAC samples was analysed and the results obtained thereof are shown in figure 17. The cyclic voltammetry (CV) and galvanostatic charge-discharge (GCD) curves obtained for the samples were found to be rectangular in shape with a symmetric linear charge-discharge curve. These unique attributes were recorded in both the positive and negative operating potential range and corroborates with a material whose mechanism of storage is mainly of EDLC behaviour [1, 4, 8, 14].

The rectangular shape of the CV curve demonstrates the fast electrochemical response, good electrical conductivity and double layer mechanism of the material, while the symmetry of the GCD curve shows the fast ion mobility within the material [1, 4, 8, 14–16]. In addition, the samples were found to have a higher electrochemical response in the negative potential window as compared to the positive potential window. This can be seen with the higher current response in the CV curve and longer discharge times as seen from the GCD curves (Fig. 17 (b)).

The electrochemical performance of the materials in terms of current response and discharge time was found to decrease with an increase in carbonization time adopted. This could be linked to the earlier suggestion that long periods of exposure of the material to the activating agent leads to a breakdown of the already established framework, resulting in a decrease in SSA. The HTAC-1 sample gave the highest current response and the longest discharge time regardless of its operation in the negative or positive potential window. Thus, it can be suggested that the ideal optimization time required for synthesizing activated carbon from hibiscus calyces was 1 hour based on the electrochemical performance which is in conformity with the textural property results.
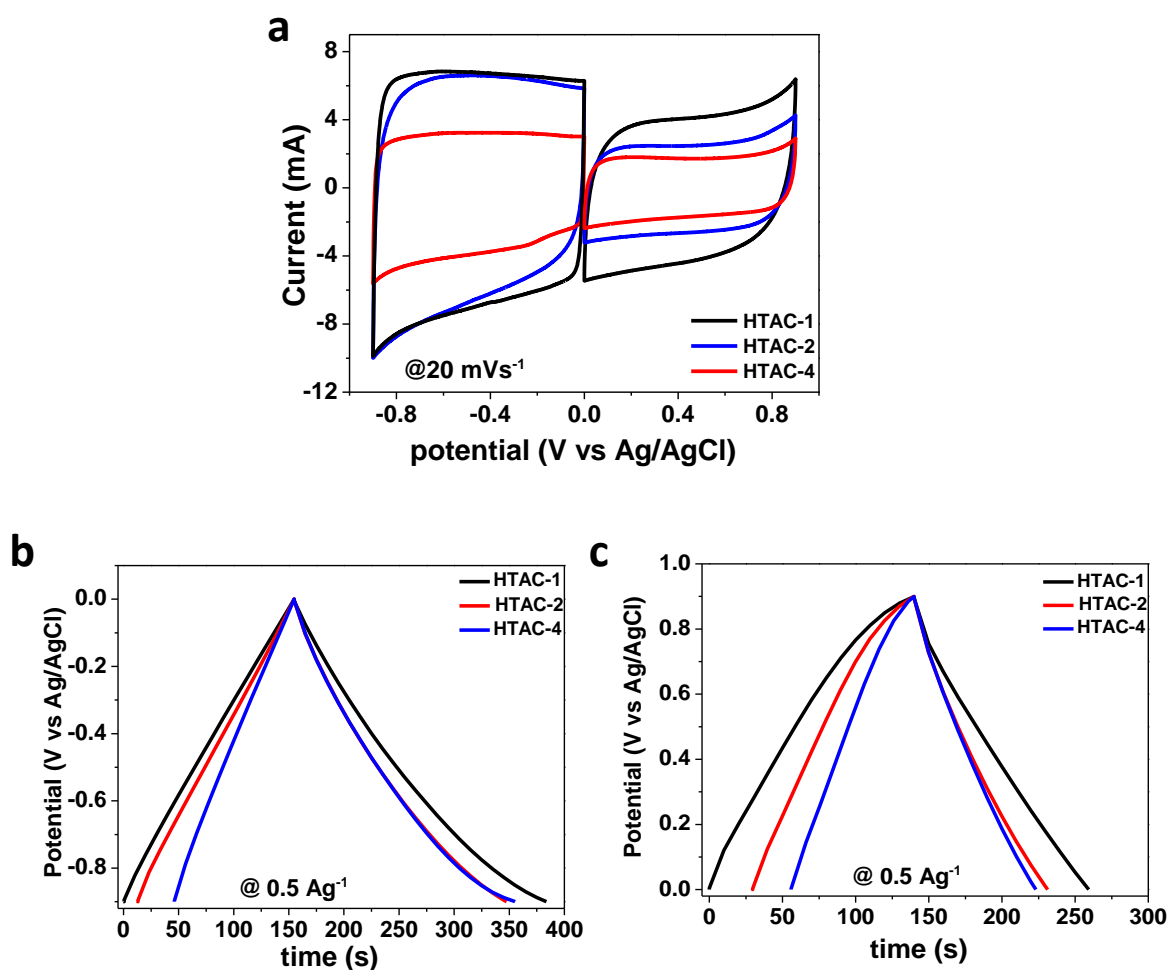
Figure 17: (a) cyclic voltammogram (CV) and (b, c) galvanostatic charge-discharge plots (GCD) of HTAC samples in both the positive and negative potential windows in a 2.5 M KNO_3 electrolyte.

The as-calculated specific capacitance of the samples with respect to the varying carbonization times is plotted in figure 18 in both operating potential range. As observed from the current response, the HTAC-1 had the highest specific capacitance of 127.12 $F \cdot g^{-1}$ and 66.39 $F \cdot g^{-1}$ in the negative and positive potential regions respectively at a specific current of 0.5 $A \cdot g^{-1}$.

Based on the findings, a detailed electrochemical evaluation was conducted on the HTAC-1 sample in a three-electrode configuration. The sample electrode was operational in both the positive and negative potential windows of 0.00 to 0.90 V and -0.90 V to 0.00 V respectively.
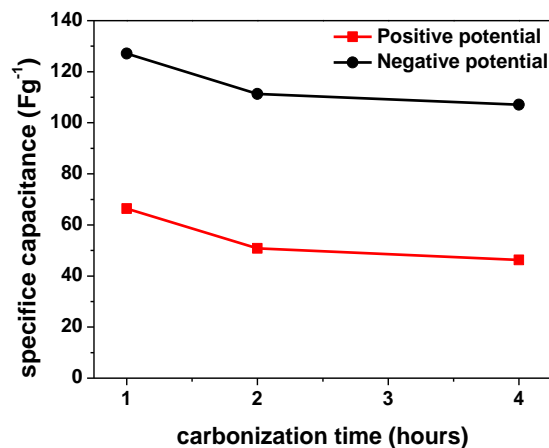
Figure 18: Specific capacitance as a function of carbonization time for the HTAC samples calculated in both the negative and positive potential windows

The current response of the sample was found to increase with an increase in the scan rate as well as little or no distortion to the EDLC nature of the CV plot in both operating potentials (see Fig. 19 (a)). This can be explained to be due to the presence of a dominating capacitive form of storage with little diffusion limitation even as scan rate increases [17].

The associated GCD plots displayed in figure 19 (b, c) depict a decreasing discharge time with an increase in the applied specific current. This is linked to the ionic movement limitation which does not give ample time for interaction with pore sites at relatively higher specific currents [18]. The relationship between the specific capacitance as a function of specific current is displayed in figure 19 (d); the specific capacitance of the material in the negative potential region was found to be higher than that in the positive potential region. As expected, the specific capacitance values decreased with an increase in the applied specific current.
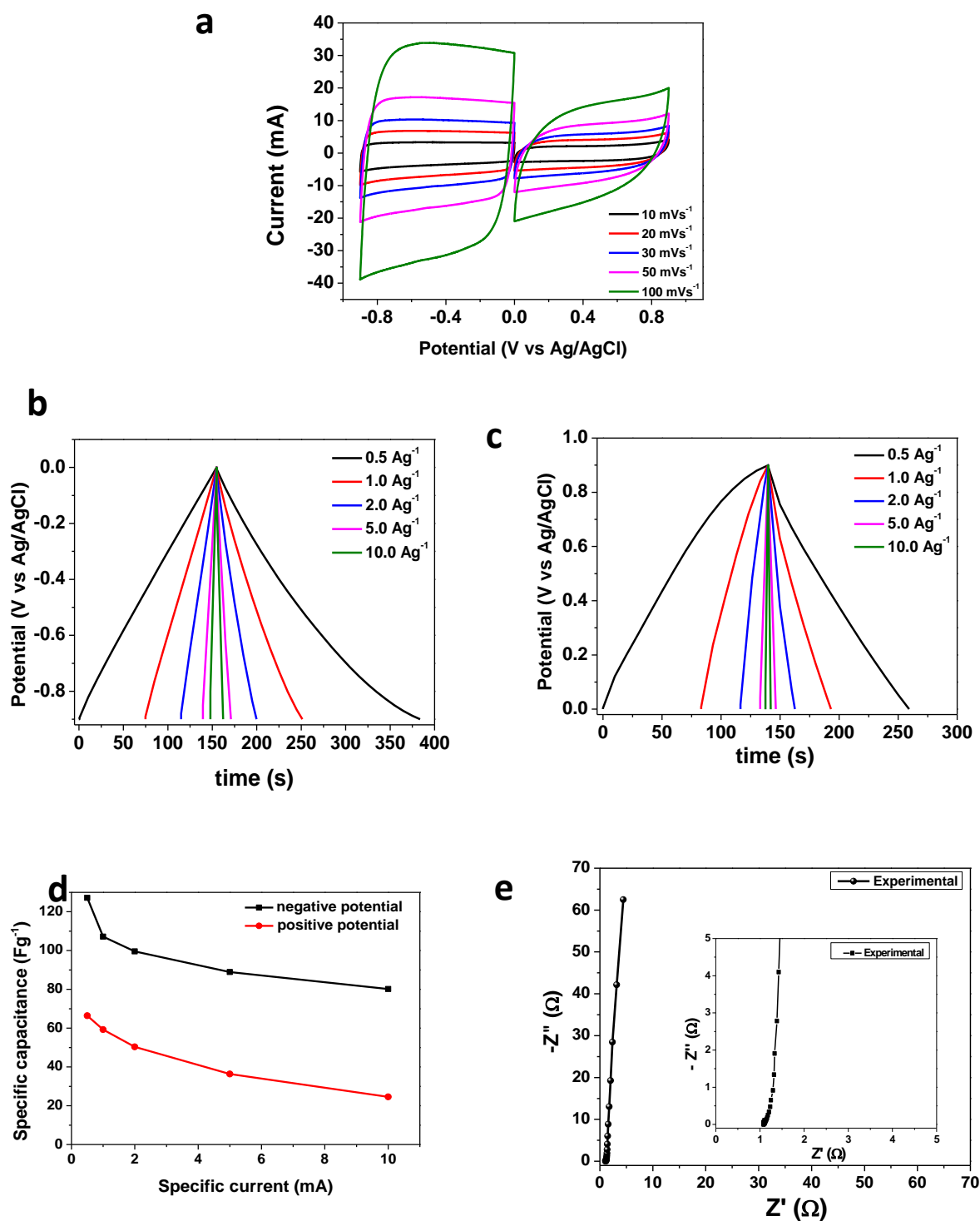
Figure 19: (a) Cyclic voltammogram (CV) and (b, c) Galvanostatic charge-discharge (GCD) plot at varying scan rates and current densities in the positive and negative potential windows, (e) Nyquist plot with corresponding circuit diagram of the HTAC-1 sample in a 2.5 M KNO_3 electrolyte.

Figure 19 (e) displays the fitting of the Nyquist plot obtained experimentally with a model described by the modified Randles circuit commonly referred to as the equivalent circuit [19]. The elements of the circuit best describes the capacitive behaviour of the sample electrode and

was done using the ZFIT data fitting software which applied the complex nonlinear least-squares method [20]. The slope of the Nyquist plot in the low-frequency region, which is almost parallel to the y-axis (perfectly vertical), is close to an ideal capacitance suggesting a pure capacitive behaviour and fast transfer character of the material. At the high frequency region, the intercept of the Nyquist plot on the real impedance (Z') axis corresponds to the equivalent series resistance, R_s. This value is comprised of the internal resistance of the sample electrode, ionic resistance of the electrolyte and the contact resistance between the active material/current collector interface [21]. An equivalent series resistance (R_s) value of 1.08 Ω was obtained for the HTAC-1 sample In addition, the short length of the Nyquist plot over varying frequency depicts a fast diffusion of the electrolyte ions within the pores of the material electrode [1, 22]. A symmetric device was assembled to further analyse the electrochemical performance of the HTAC-1 sample in the two-electrode configuration. The symmetric device was operational in an operating voltage window of 0.00 to 1.80 V. This showed a successful exploitation of the operating potential in both the positive and negative range. Similar characteristics of the half-cell electrodes were recorded in the symmetric device. The current response of the sample was found to increase with an increase in the scan rate as can be seen in figure 20(a). Correspondingly, the discharge time decreased with an increase in the applied specific current as observed in figure 20(b).

The specific capacitance as a function of specific current displayed in figure 20(d) reports a device specific capacitance of 65.68 $F \cdot g^{-1}$ with a corresponding specific energy and power values of approximately 7.39 $Wh \cdot kg^{-1}$ and 450 $W \cdot kg^{-1}$ respectively, at a specific current of ca. 0.5 $A \cdot g^{-1}$.
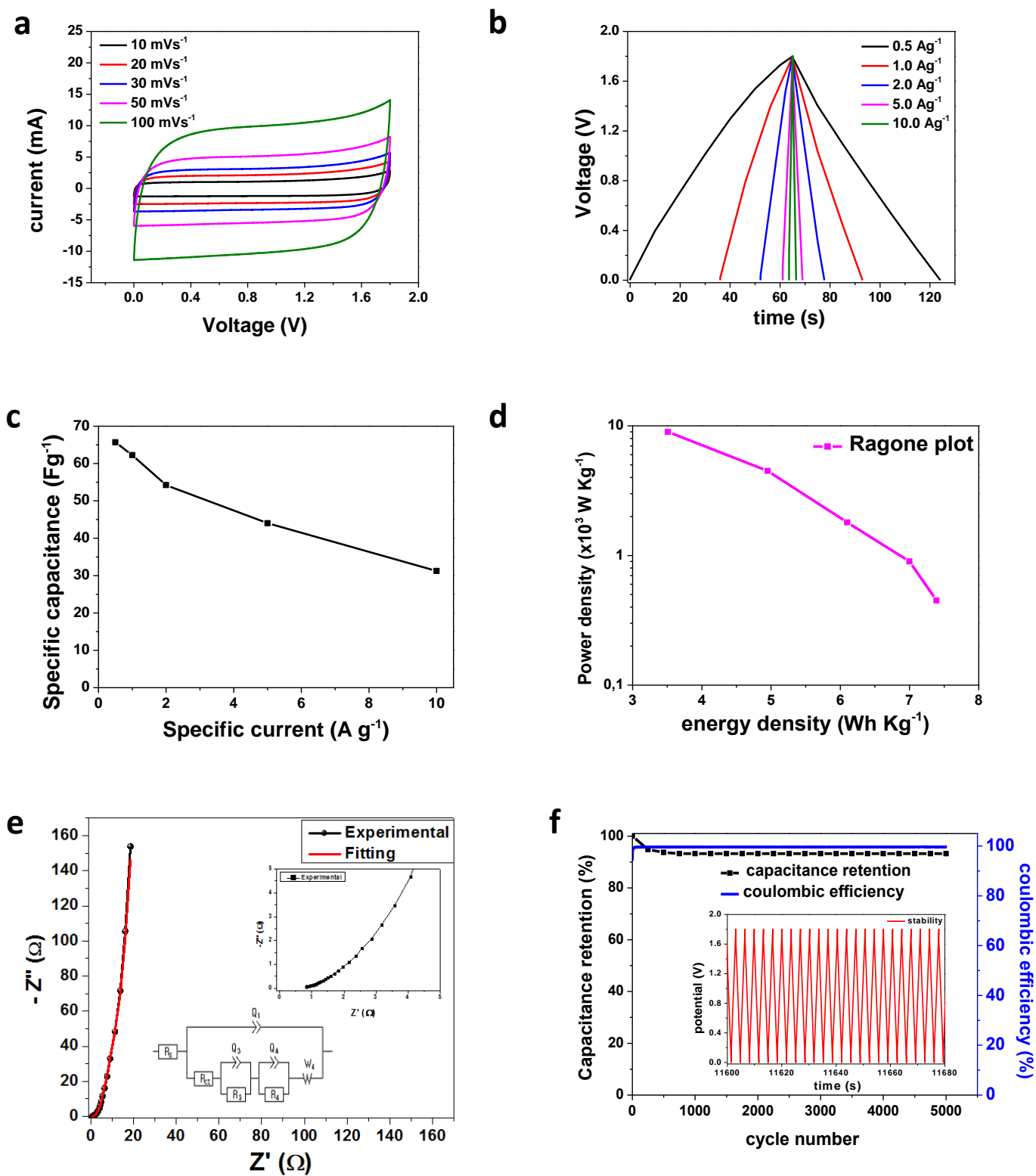
Figure 20: (a) Cyclic voltammogram, (b) galvanostatic charge-discharge plot, (c) specific capacitance, (d) Ragone plot, (e) Nyquist plot and (f) the capacitance retention versus cycle number with the figure inset showing a few galvanostatic charge-discharge cycles at 10 A g^{-1} of the HTAC-1 symmetric device

The Nyquist plot of the device with its corresponding circuit diagram was plotted in figure 20(e). The curve was quasi-vertical in the low-frequency region, had an intercept with the real impedance axis at the high frequency region corresponding to an R_s value of 0.82 Ω.

The equivalent circuit diagram (inset to figure 20(e)) shows the equivalent series resistance (R_s) element in series with the charge transfer resistance (R_{ct}). The set of constant phase elements (Q) are connected in parallel with respective leakage resistors (R) which can be linked to the deviation of the Nyquist plot from the ideal behaviour in the low frequency region [23]. The Warburg impedance (W) is due to the semi-infinite diffusion electrolyte within the electrode material causing a deviation from the ideal behaviour of the sample [1, 8, 14, 15, 22, 24].

Cycling ageing test (Fig. 20(f)) was conducted on the device with the device retaining 93% of its original capacitance value even after 5000 constant galvanostatic charge-discharge cycles. An associated device coulombic efficiency of 98% was also recorded for the activated carbon-based symmetric device which demonstrates its long term cyclic capability.

4.6.2. Electrochemical characterization of AC-PPY samples

The electrochemical performance of the AC-PPY samples with different mass ratios of activating agent to raw polypyrrole polymer was analysed with the results summarized in figure 21.

The CV and GCD curves of the PPY-based samples all exhibited rectangular-shaped CV and triangular GCD profiles respectively within an operating potential window range of 0.80 V.

In figure 21(a-b), the AC-PPY-6 sample exhibited the highest current response as well as longest discharge time which contributes to high capacitive performance of the material.

A detailed and in-depth electrochemical performance analysis of the AC-PPY-6 sample was performed based on the initial tests to determine the charge storage capability of the PPY material.

In figure 21(e), the AC-PPY-6 sample exhibited the most ideal capacitance behavior with respect to the vertical nature of the Nyquist plot in the low-frequency region and also had a shortest diffusion length with a relatively low R_s value of 0.50 Ω (Fig. 21(f)).

In Figure 21(c), the current response of the AC-PPY-6 sample increased with an increase in the scan rate which signifies the charge storage mechanism to be largely capacitive with negligible diffusion limitation. The decreased discharge time with an increase in the specific applied current was also attributed to the inability of charges to fully interact with pore sites at high specific current values as observed in the electrochemical results for the AC-PPY samples.
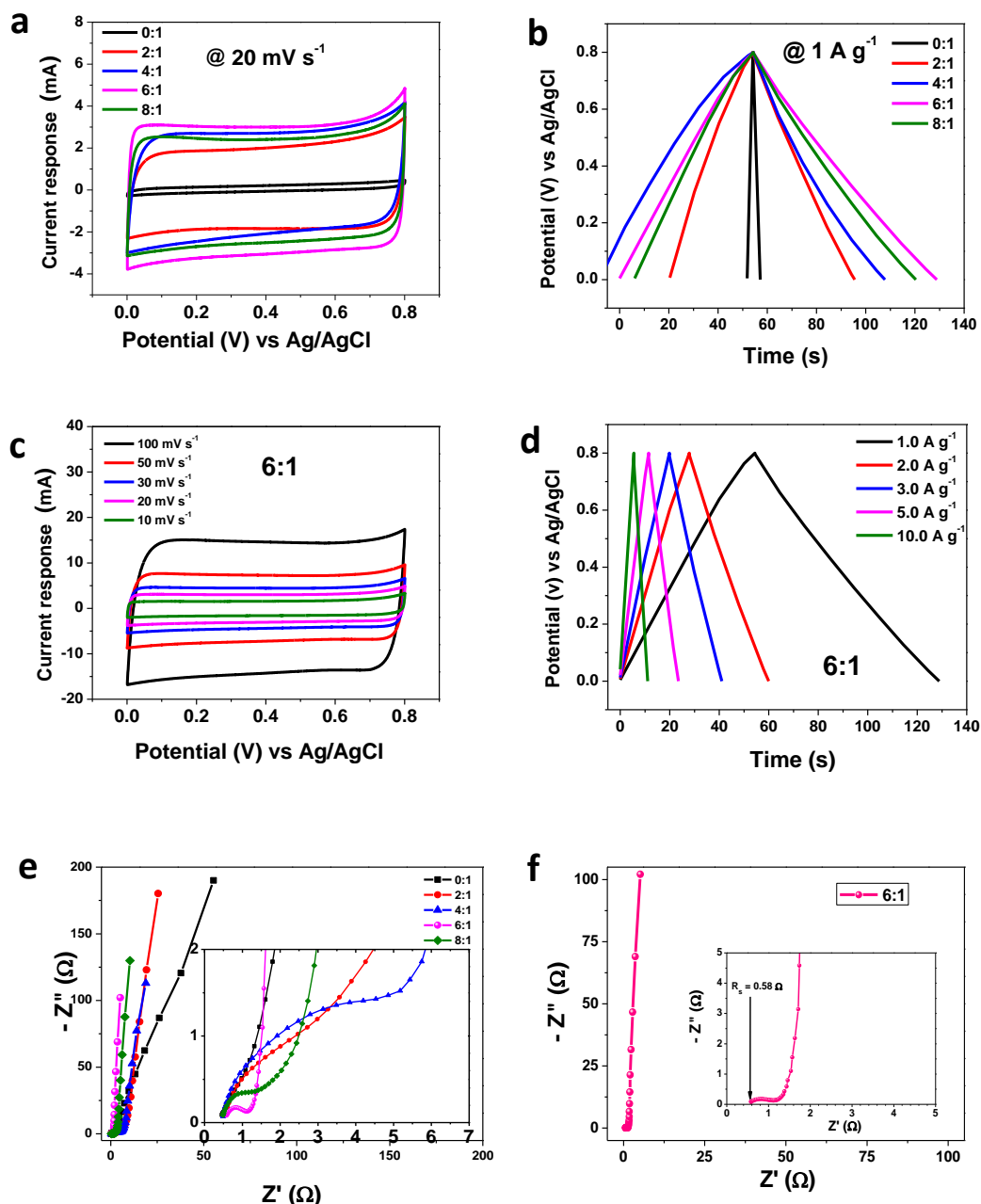
Fig. 21: (a, b) Cyclic voltammetry (CV) and associated galvanostatic charge-discharge (GCD) plots of AC-PPY samples, (c, d) detailed CV and the related GCD profile of AC-PPY-6 sample at varying scan rates and current densities, (e, f) EIS plot of the AC-PPY samples and (f) the EIS of AC-PPY-6 sample in a 2.5 M KNO_3 electrolyte.

60
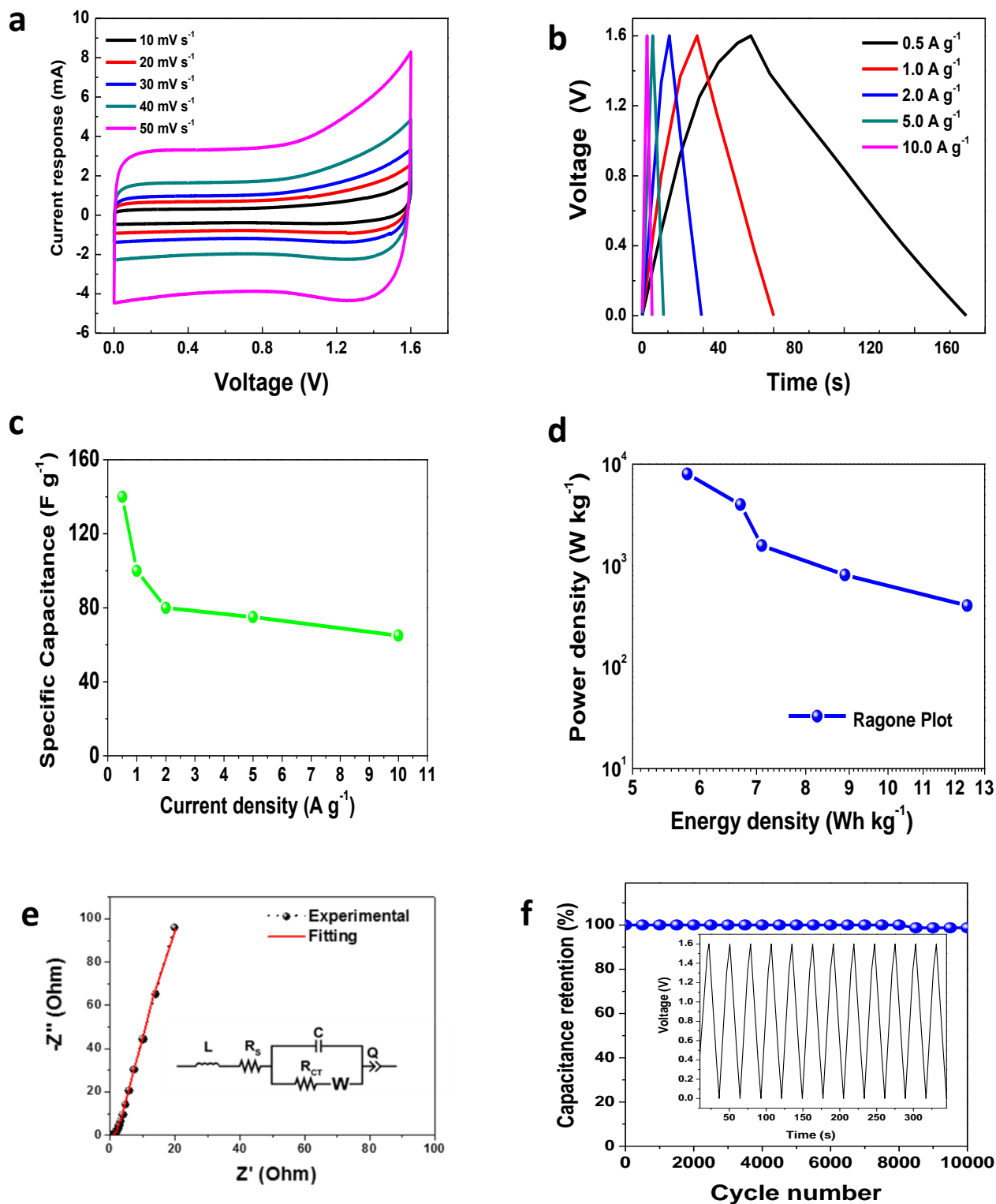
Figure 22: (a) Cyclic voltammogram (CV), (b) Galvanostatic charge-discharge (GCD) plot, (c) specific capacitance, (d) Ragone plot, (e) Nyquist plot and (f) the capacitance retention versus cycle number with the inset to the figure showing a few galvanostatic charge-discharge cycles at 2 A g^{-1} of the AC-PPY-6 symmetric device

The AC-PPY-6 sample was further analysed as a symmetric device. The sample had a stable working potential window of 1.60 V for the full cell, as shown in figure 22(a, b). The capacitance obtained at a specific current of 0.50 A·g^{-1} was 140 F·g^{-1}. An energy density and corresponding power density of 12.40 Wh·kg^{-1} and 415 W·kg^{-1} respectively were calculated at a specific current of 0.50 A·g^{-1}. The cell was also found to have retained 99% of its initial capacitance after 10 000 cycles.

Further ageing tests were conducted on the device in the form of voltage holding and self-discharge. The voltage holding test was conducted for 72 hours with capacitance being monitored at 10 hour intervals (Fig. 23(a, b)). The capacitance was found to increase as time elapsed due to the improved wettability and availability of pores. The capacitance of the material increased from 75 F·g^{-1} to 137.5 F·g^{-1}, with the energy density increasing from 6.70 Wh·kg^{-1} to 12.20 Wh·kg^{-1} at a specific current of 2.0 A·g^{-1}. The increase in the capacitance of the material was due to an increase in the accessibility of pores, which resulted in an increase in the capacitance of the material.

Self-discharge test (Fig. 23(c-d)) was also performed on the device, and it was found that the device had a slow discharge rate and it maintained a potential of 1.04 V for over 40 hours. However, the device initially discharged at a very fast rate, with a potential drop from 1.50 V to 1.27 V. This is linked to the thermodynamic limit experienced by aqueous solutions due to the initial decomposition of water at ~1.2V [17, 25]. The self-discharge profile was characterized by two different diffusion-controlled mechanism fitted to different equations as follows:

$$V_t = V_i - m.t^{1/2} \tag{5}$$

where V_t is defined as the voltage in a given self-discharge time, t is the self-discharge time, V_i is defined as the maximum voltage, and m is a diffusion and geometrical constant dependent on the material electrode parameters.

Figure 23: (a) Specific capacitance variation with voltage holding time periods, (b) Cyclic voltammogram profile before and after voltage holding, (c) self-discharge, and (d) fitting of self-discharge curve as a function of $t^{1/2}$.

The value of *m* defined the exact diffusion mechanism observed [26]. From the results obtained, it was evident that the PPY-based activated carbon samples performed better as a potential energy storage material.

A detailed report summarizing the results obtained from the conversion of conductive polymer into activated carbon nanostructures (AC-PPY) is presented in the appendix entitled; *"Electrochemical analysis of nanoporous carbons derived from activation of polypyrrole for stable supercapacitors"* and has been published in the Journal of Material Science (Energy Materials).

4.6.3. Mixed assembly electrode device

A mixed hybrid (MA) device was fabricated from the HTAC-1 and AC-PPY-6 samples to analyse its electrochemical properties. HTAC-1 was used as a negative electrode and PPY-6 was used as a positive electrode based on their individual three electrode measurements performance in both potential windows. The device was operational in a voltage window of 1.70 V in order to extend the operating voltage by harnessing individual properties from both forms of activated carbon from biomass waste as well as conductive polymer sources.

The current response of the mixed hybrid device was found to increase with an increase in the scan rate as can be seen in the CV plot (Fig. 24(a)). Similarly, in figure 24(b) the discharge time decreased with an increase in the applied specific current.

The specific capacitance of the device calculated from the discharge part of the GCD profile was found to be 94.44 $F \cdot g^{-1}$ with a corresponding energy density and power density values of 9.45 $Wh \cdot kg^{-1}$ and 420 $W \cdot kg^{-1}$ respectively, at a specific current of 0.50 $A \cdot g^{-1}$.

The Nyquist plot of the device with its corresponding circuit diagram was plotted in figure 24(c). The curve was vertical in the low-frequency region and a corresponding R_s value of 0.60 Ω was recorded. Cycling ageing test (Fig. 24(e)) was conducted on the device and after 10 000 cycles the device had a capacitance retention of 82 % and a coulombic efficiency of 99.6 %.

Interestingly, it is observed that the mixed device, although it has a low capacitance value compared to the AC-PPY-6 symmetric device, it had better stability compared to the both the AC-PPY-6 and HTAC-1 symmetric devices.

Table 4 summarises the performance results of the AC-PPY-6, HTAC-1 and MA devices and it is notable in the coulombic efficiency values for the MA device was much higher than those of the AC-PPY-6 device and the HTAC-1 device was higher than that of the MA device.
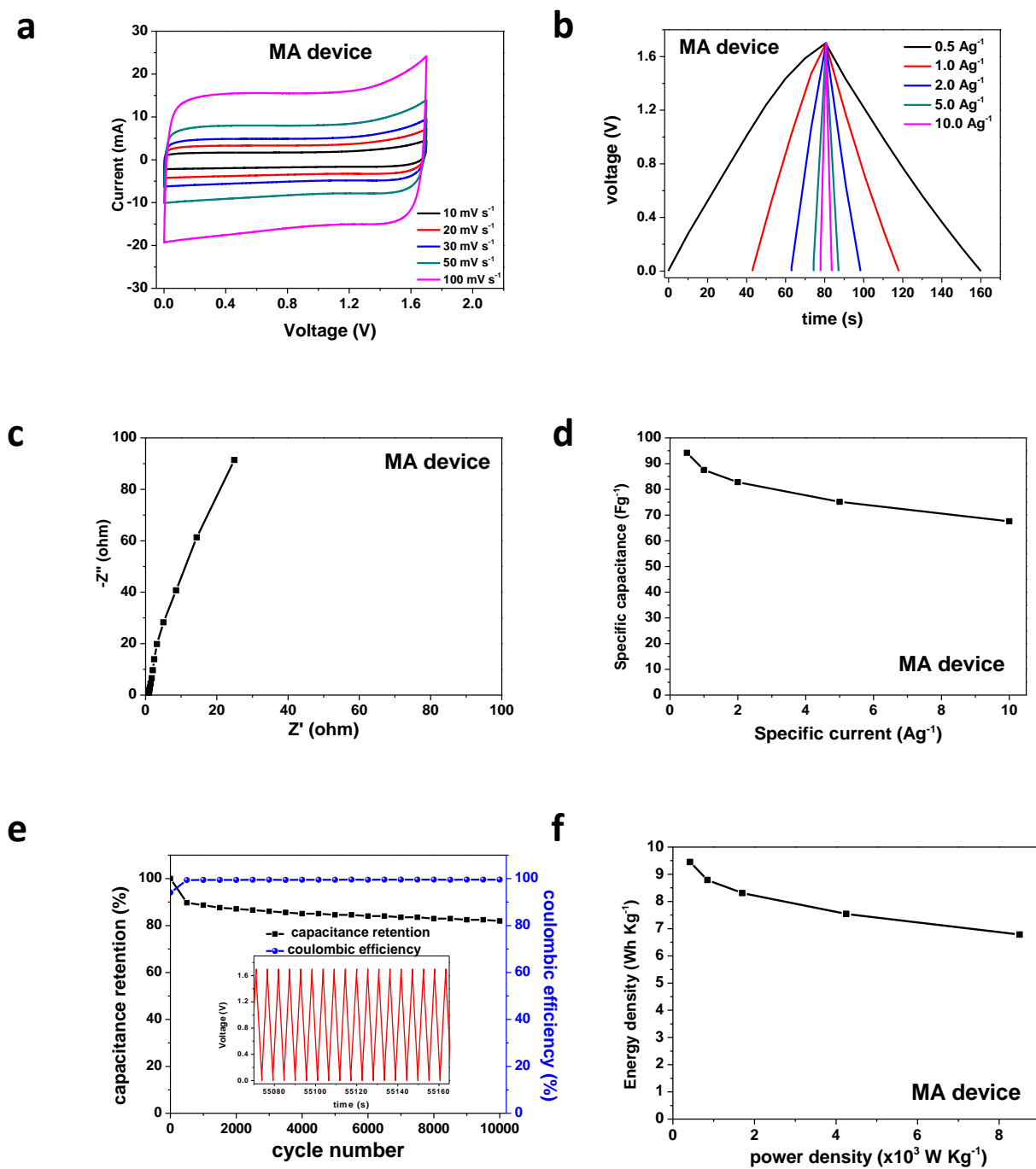
Figure 24: Cyclic voltammogram (CV), (b) Galvanostatic charge-discharge (GCD) plot, (c) Nyquist plot (EIS), (d) specific capacitance, (e) capacitance retention and the Ragone plot of the HTAC-1 // AC-PPY-6 sample.
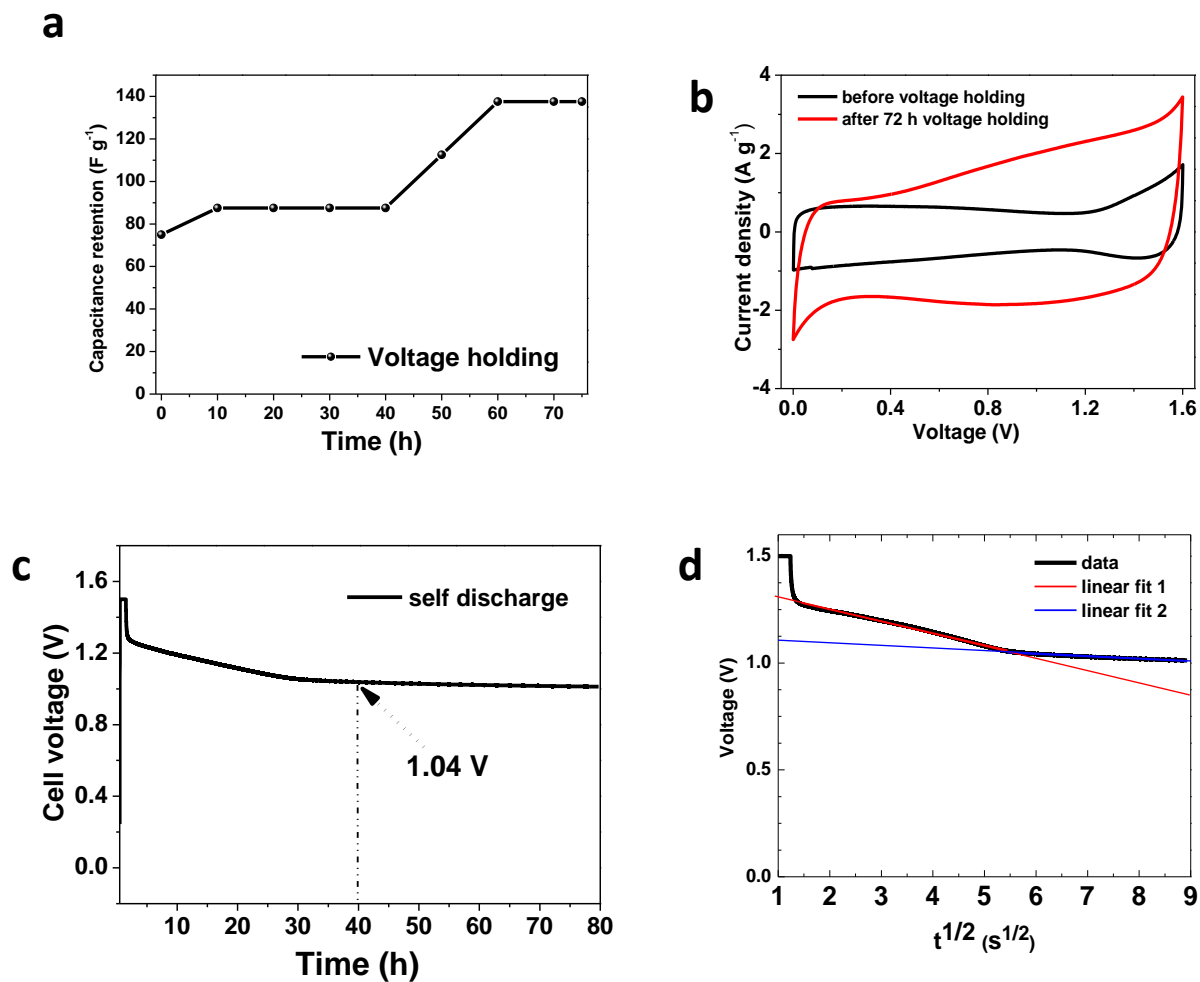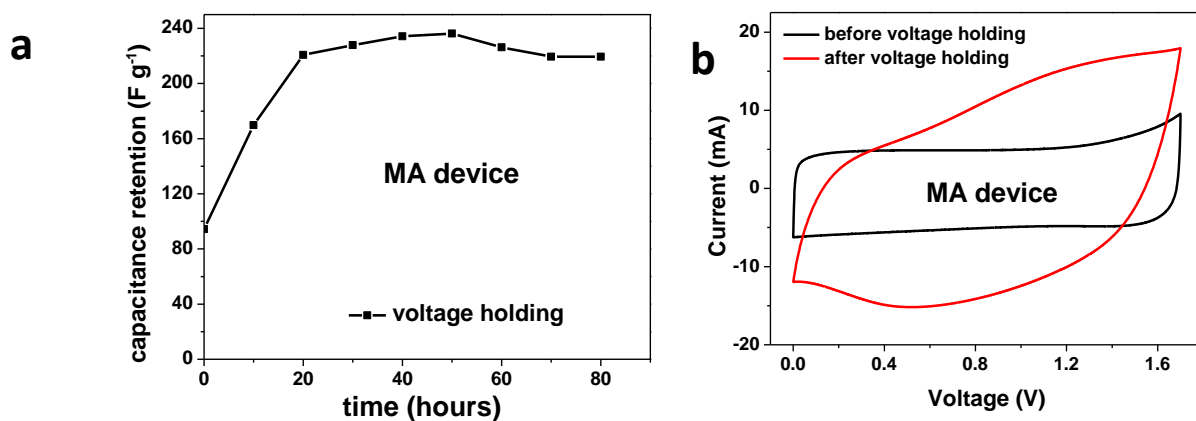
Figure 25: (a) Specific capacitance variation with voltage holding time periods, (b) Cyclic voltammogram profile before and after voltage holding

Table 4: Summary of performance data for all 3 devices (HT-AC-1, AC-PPY-6 and MH)

	Capacitance (@0.5 Ag^{-1}) (Fg^{-1})	Capacitance retention (%)	Coulombic efficiency (%)
HTAC-1	65.98	93	98
AC-PPY-6	140	99	N/A
MA	94.44	82	99.6

The MA device still proved to be more stable as it had a coulombic efficiency of 99.6 % which correlates with better electrochemical reaction.

The mixed cell was subjected to further ageing test, the voltage holding (as seen in Fig. 25(a, b)) was conducted for 80 hours, and the capacitance of the device was found to increase as time progressed. The specific capacitance increased from 94.44 F·g^{-1} to 219.48 F·g^{-1} after 80 hours. The device also had a higher current response after the voltage holding test, which confirms the improvement in the performance of the device.

References

1.   Bello, A., Manyala, N., Barzegar, F., Khaleed, A.A., Momodu, D.Y. and Dangbegnon, J.K. 2016. *Renewable pine cone biomass derived carbon materials for supercapacitor application. RSC Advances*,*6*(3), pp.1800-1809.

2.   Momodu, D., Madito, M., Barzegar, F., Bello, A., Khaleed, A., Olaniyan, O., Dangbegnon, J. and Manyala, N. 2017. *Activated carbon derived from tree bark biomass with promising material properties for supercapacitors. Journal of Solid State Electrochemistry*, *21*(3), pp.859-872.

3.   Hu, B., Wang, K., Wu, L., Yu, S.H., Antonietti, M. and Titirici, M.M. 2010. *Engineering carbon materials from the hydrothermal carbonization process of biomass. Advanced Materials*, *22*(7), pp.813-828.

4.   Momodu, D.Y., Madito, M.J., Barzegar, F., Masikhwa, T.M., Ugbo, F., Khaleed, A.A., Bello, A., Dangbegnon, J.K. and Manyala, N. 2016. *Activated carbon derived from tree bark biomass for high performance electrochemical capacitors*. In Meeting Abstracts (No. 7, pp. 984-984). The Electrochemical Society.

5.   Sun, H., He, W., Zong, C. and Lu, L. 2013. *Template-free synthesis of renewable macroporous carbon via yeast cells for high-performance supercapacitor electrode materials*. ACS applied materials & interfaces, 5(6), pp.2261-2268.

6.   Sadezky, A., Muckenhuber, H., Grothe, H., Niessner, R. and Pöschl, U. 2005. *Raman microspectroscopy of soot and related carbonaceous materials: spectral analysis and structural information*. Carbon, 43(8), pp.1731-1742.

7.   Zhang, H., Zhang, L., Chen, J., Su, H., Liu, F. and Yang, W. 2016. *One-step synthesis of hierarchically porous carbons for high-performance electric double layer supercapacitors*. Journal of Power Sources, 315, pp.120-126.

8.   Fasakin, O., Dangbegnon, J.K., Momodu, D.Y., Madito, M.J., Oyedotun, K.O., Eleruja, M.A. and Manyala, N. 2018. *Synthesis and characterization of porous carbon derived from activated banana peels with hierarchical porosity for improved electrochemical performance*. Electrochimica Acta, 262, pp.187-196.

9.   Mallard, L.M., Pimenta, M.A.A., Dresselhaus, G. and Dresselhaus, M.S. 2009. *Raman spectroscopy in graphene*. Physics Reports, 473(5-6), pp.51-87.

10.   Mao, Y., Duan, H., Xu, B., Zhang, L., Hu, Y., Zhao, C., Wang, Z., Chen, L. and Yang, Y. 2012. *Lithium storage in nitrogen-rich mesoporous carbon materials*. Energy & Environmental Science, 5(7), pp.7950-7955.

11.   Yao, L., Yang, G., Han, P., Tang, Z. and Yang, J. 2016. *Three-dimensional beehive-like hierarchical porous polyacrylonitrile-based carbons as a high performance supercapacitor electrodes*. Journal of Power Sources, 315, pp.209-217.

12.   Ofomaja, A.E. and Naidoo, E.B. 2011. *Biosorption of copper from aqueous solution by chemically activated pine cone: a kinetic study*. Chemical Engineering Journal, 175, pp.260-270.

13.   Sevilla, M. and Fuertes, A.B. 2009. *The production of carbon materials by hydrothermal carbonization of cellulose*. Carbon, 47(9), pp.2281-2289.

14.   Hu, S., Zhang, S., Pan, N. and Hsieh, Y.L. 2014. *High energy density supercapacitors from lignin derived submicron activated carbon fibers in aqueous electrolytes*. Journal of Power Sources, 270, pp.106-112.

15.   Peng, C., Yan, X.B., Wang, R.T., Lang, J.W., Ou, Y.J. and Xue, Q.J. 2013. *Promising activated carbons derived from waste tea-leaves and their application in high performance supercapacitors electrodes*. Electrochimica Acta, 87, pp.401-408.

16.   Rufford, T.E., Hulicova-Jurcakova, D., Khosla, K., Zhu, Z. and Lu, G.Q. 2010.

Microstructure and electrochemical double-layer capacitance of carbon electrodes prepared by zinc chloride activation of sugar cane bagasse. Journal of Power Sources, 195(3), pp.912-918.

17. Momodu, D., Bello, A., Oyedotun, K., Ochai-Ejeh, F., Dangbegnon, J., Madito, M. and Manyala, N. 2017. *Enhanced electrochemical response of activated carbon nanostructures from tree-bark biomass waste in polymer-gel active electrolytes*. RSC Advances, 7(59), pp.37286-37295.

18. Lao, Z.J., Konstantinov, K., Tournaire, Y., Ng, S.H., Wang, G.X. and Liu, H.K. 2006. *Synthesis of vanadium pentoxide powders with enhanced surface-area for electrochemical capacitors*. Journal of power sources, 162(2), pp.1451-1454.

19. Randles J.E.B. 1968. *Kinetics of rapid electrode reactions*. 20:1411–1414. RSC

20. Conway, B.E. 1999. *Electrochemical Capacitors: Scientific Fundamentals and Technology Applications*. Springer.

21. Fan, Z., Yan, J., Wei, T., Zhi, L., Ning, G., Li, T. and Wei, F. 2011. *Asymmetric supercapacitors based on graphene/MnO2 and activated carbon nanofiber electrodes with high power and energy density*. Advanced Functional Materials, 21(12), pp.2366-2375.

22. Momodu, D., Okafor, C., Manyala, N., Bello, A., ZebazeKana, M.G. and Ntsoenzok, E. 2017. *Transformation of Plant Biomass Waste into Resourceful Activated Carbon Nanostructures for Mixed-Assembly Type Electrochemical Capacitors*. Waste and Biomass Valorization, pp.1-13.

23. Barzegar, F., Khaleed, A.A., Ugbo, F.U., Oyeniran, K.O., Momodu, D.Y., Bello, A., Dangbegnon, J.K. and Manyala, N. 2016. *Cycling and floating performance of symmetric supercapacitor derived from coconut shell biomass*. AIP Advances, 6(11), p.115306.

24. Long, J.W., Bélanger, D., Brousse, T., Sugimoto, W., Sassin, M.B. and Crosnier, O. 2011. *Asymmetric electrochemical capacitors - Stretching the limits of aqueous electrolytes*. MRS Bulletin, *36*(7), pp.513-522.

26. Andreas, H.A. 2015. *Self-discharge in electrochemical capacitors: a perspective article*. Journal of The Electrochemical Society, 162(5), pp.A5047-A5053.

CHAPTER 5

SUMMARY, CONCLUSION AND FUTURE WORK

Activated carbon derived from hibiscus biomass waste and conductive polypyrrole (PPY) was synthesised, optimized and investigated as potential electrodes for energy storage devices.

The synthesis optimization process was done by considering three factors namely; the inclusion of a pre-hydrothermal step, varying the activation time and the amount of the activating agent with respect to the raw polymer material. The results obtained from the various detailed studies aid in providing a pathway to obtaining porous, electrochemically active carbon-based materials suitable for electric double layer capacitors as well as mixed hybrid devices.

5.1.   Activated carbon derived from biomass waste

Dried hibiscus calyces were used as the raw material in the preparation of activated carbon from biomass waste. The hibiscus calyces was subjected to preparation with the incorporation of a hydrothermal (HT) pre-processing step prior to carbonization with $KHCO_3$ as an activating agent. The biomass waste was optimized based on the effect of carbonization time, samples were prepared with the optimized carbonization times of 1 hr, 2 hrs, and 4hrs. Non-hydrothermalized (NHT) samples serving as control standards were also prepared.

The samples were found to contain a combination of micropores and mesopores necessary for efficient charge transport and storage. Furthermore, the inclusion of the HT process before actual activation halved the optimal carbonization time required for complete activation of the material from 2 hours to 1 hour based on the as-obtained specific surface area values. As shown in table 1, the 2 hours carbonization time produced a porous carbon material with a SSA value of ~ 1000 $m^2 \cdot g^{-1}$ for non-pre-treated hydrothermal raw materials. However, the time required to obtain the same nominal value > 1000 $m^2 \cdot g^{-1}$ was reduced to only 1 hour with the pre-treated sample (HTAC-1). From this, the HTAC-1 had the highest SSA and pore volume of 1337.12

$m^2 \cdot g^{-1}$ and 1.29 $cm^3 \cdot g^{-1}$ as compared to the NHTAC-2 sample with a BET SSA of 1057.28 $m^2 \cdot g^{-1}$ and pore volume of 2.53 $cm^3 \cdot g^{-1}$ respectively.

The structural and compositional characterization revealed that the as-synthesized samples consisted purely of carbon with an amorphous crystal structure based on the EDS and XRD results respectively.

The electrochemical results correlated with the results obtained in BET with the HTAC-1 sample yielding the highest current response and the longest charge-discharge times.

The samples had an operating potential window of 0.90 V in both the positive and negative potential windows. A specific capacitance of 127.12 $F \cdot g^{-1}$ and 66.39 $F \cdot g^{-1}$ was calculated for the HTAC-1 sample in the negative and positive operating potential windows respectively.

A symmetric device was fabricated using the HTAC-1 sample, which was operational in a voltage window of 1.80 V. The calculated specific capacitance for the device was 65.68 $F \cdot g^{-1}$, with a corresponding energy and power densities of 7.39 $Wh \cdot kg^{-1}$ and 450 $W \cdot kg^{-1}$ respectively at a specific current of 0.5 $A \cdot g^{-1}$.

Stability tests reports showed a 93 % capacitance retention obtained for the sample after 5000 constant charge-discharge cycles at a specific current of 10.0 $A \cdot g^{-1}$ with a corresponding coulombic efficiency of 98 %.

5.2. Activated carbon derived from polypyrrole

Polypyrrole (PPY) was used as the raw material in the preparation of activated carbon with K_2CO_3 serving as the activating agent (AA). The activated carbon was prepared by optimizing the activating agent mass content to the raw polymer material present for creation of necessary pores within the material. The AA:PPY ratios considered for the optimization process were 0:1, 2:1, 4:1, 6:1 and 8:1.

From the textural analysis, the AC-PPY-6 was found to have the best pore structure features with the SSA and pore volume being the highest as compared to the other samples. The AC-PPY-6 sample had a SSA and pore volume of 1980.81 $m^2 \cdot g^{-1}$ and 1.24 $cm^3 \cdot g^{-1}$ respectively.

From the electrochemical tests conducted on the AC-PPY-6 sample, an operating potential window of 0.80 V was recorded in both the positive and negative potential windows. The current response was found to increase with an increase in the scan rate while the discharge time decreased in a decrease in the specific current applied. A specific capacitance of up to 93.17 $F \cdot g^{-1}$ was calculated at a specific current of 1.0 $A \cdot g^{-1}$.

A symmetric device was fabricated using the AC-PPY-6 sample, which was operated in a voltage window of 1.60 V. A device capacitance per single electrode of 140 $F \cdot g^{-1}$ was obtained at a specific current of 0.5 $F \cdot g^{-1}$ with a 99% capacitance retention value after 10 000 cycles at a specific current of 2.0 $A \cdot g^{-1}$. The sample device was further subjected to a voltage holding ageing test, to determine the performance of the device as a function of constant applied voltage over extended periods of time. This has been described to be a much better route to performing ageing test as it mimics the actual practical device operation. From the results obtained, the device had an increased ion-storage capability based on the calculated capacitance and associated energy density values.

Due to an increase in the accessibility of pores after the ageing test, the capacitance and energy density increased from 75 $F \cdot g^{-1}$ – 137.5 $F \cdot g^{-1}$ and from 6.7 $Wh \cdot kg^{-1}$ to 12.2 $Wh \cdot kg^{-1}$ respectively, at a specific current of 2.0 $A \cdot g^{-1}$.

5.3. Mixed assembly energy storage device

A mixed assembly (MA) device was fabricated from the HTAC-1 and the AC-PPY-6 samples. The device had an operating voltage window of 1.70 V. A specific capacitance of 94.44 $F \cdot g^{-1}$ was calculated, with a corresponding energy and power densities of 9.45 $Wh \cdot kg^{-1}$ and 420 $W \cdot kg^{-1}$ respectively at a specific current of 0.5 $A \cdot g^{-1}$. The device had a capacitance retention of

82 % and a coulombic efficiency of 99.6% after 10 000 constant charge-discharge cycles. The performance of the device was found to improve after the voltage holding ageing test was conducted for 80 hours, the capacitance of the device increased as time progressed. The specific capacitance increased from 94.44 $F \cdot g^{-1}$ to 219.48 $F \cdot g^{-1}$ after 80 hours.

The mixed device was found to have better stability compared to the AC-PPY-6 and HTAC-1 symmetric devices. Although it has a low capacitance value compared to the AC-PPY-6 symmetric device, the MA device had a higher coulombic efficiency value. The fabrication of an asymmetric device from the HTAC-1 and AC-PPY-6 improved the stability of the device making it a more efficient energy storage device.

5.4. Future work

Future work will involve conducting further electrochemical performance tests on the carbon samples to determine their electrochemical response in ionic liquid electrolytes, including the effect of heating the electrolytes.

Ionic liquids can permit devices to be operational in an electrochemical potential ranges from 3 V to 6 V. They are classified as green solvents due to their low volatility and the potential to replace hazardous solvents presently used in energy storage devices, This makes them suitable novel environmentally friendly storage units [1–3].

It is well known that conductivity is a limiting factor in the use of ionic liquids in electrochemical capacitors; as such further studies will involve addition of conductive additives to improve ionic conductivity [1].

Operation of these devices at extremely low and high temperatures for highly specific applications where capacitors are required will also be explored in future studies.

Some of the ionic liquids proposed for further tests on the samples include, 1-ethyl-3-methylimidazolium bis(trifluoromethylsulfonyl)amide (EMIM-TFSI) and 1-butyl-1-methylpyrrolidinium bis(trifluoromethylsulfonyl)amide (PYR14-TFSI).

References

1. Solar, E.D.S. 2009. *Alternative Energy Photovoltaics, Ionic Liquids, and MOFs*. Material matters. 4(4)

2. MacFarlane, D.R., Tachikawa, N., Forsyth, M., Pringle, J.M., Howlett, P.C., Elliott, G.D., Davis, J.H., Watanabe, M., Simon, P. and Angell, C.A. 2014. *Energy applications of ionic liquids.* Energy & Environmental Science, 7(1), pp.232-250.

3. Brandt, A., Pohlmann, S., Varzi, A., Balducci, A. and Passerini, S. 2013. *Ionic liquids in supercapacitors*. MRS bulletin, 38(7), pp.554-559.
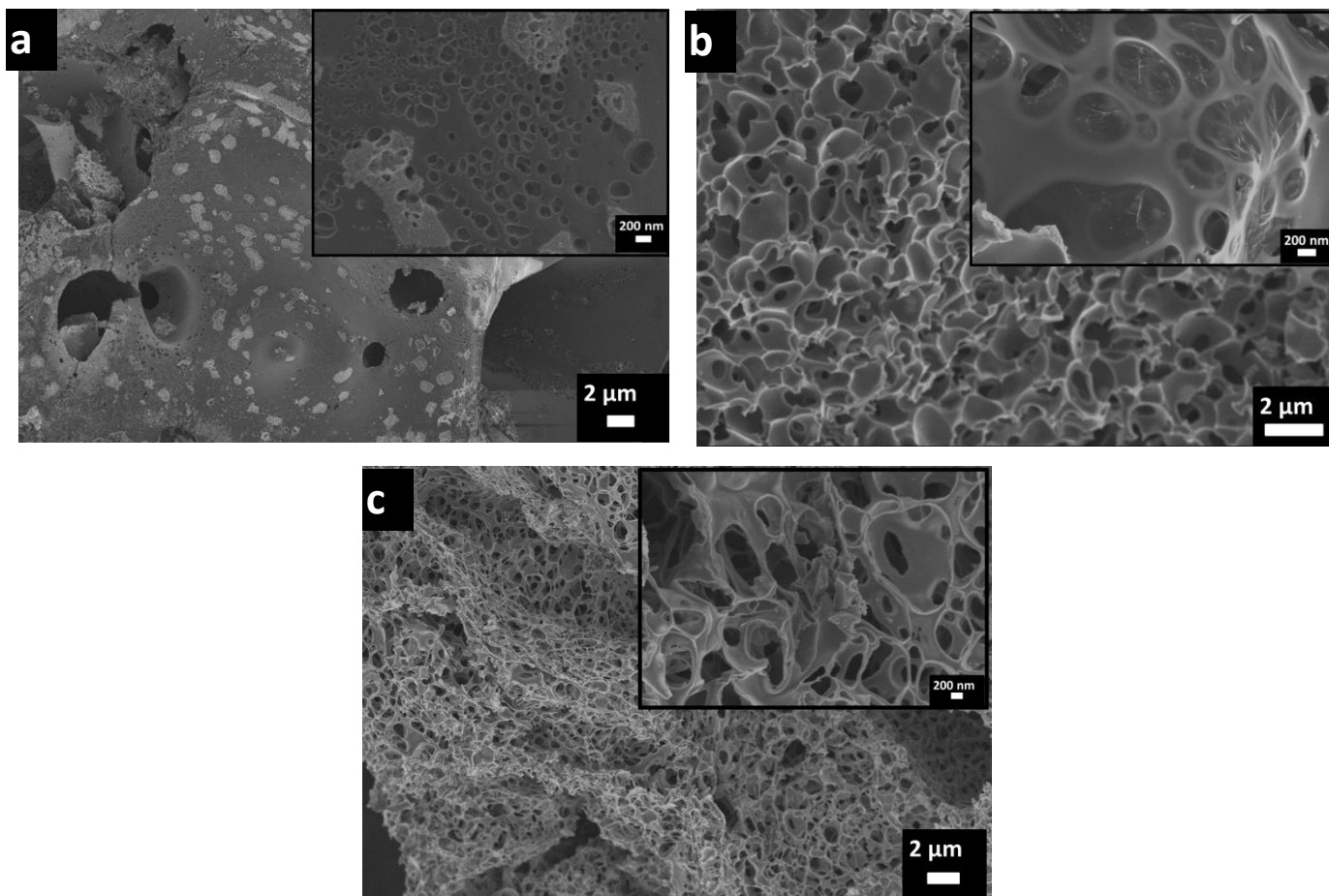
APPENDIX

Figure A1: SEM micrographs at low and higher magnifications (inset) of (a) NHTAC-1, (b) NHTAC-2 and (c) NHTAC-4.

Energy materials

CrossMark

Electrochemical analysis of nanoporous carbons derived from activation of polypyrrole for stable supercapacitors

Belinda Moyo[1] , Damilola Momodu[1] , Oladepo Fasakin[1,2] , Abdulhakeem Bello[1,3] ,
Julien Dangbegnon[1] , and Ncholu Manyala[1,*]

[1] *Department of Physics, Institute of Applied Materials, SARCHI Chair in Carbon Technology and Materials, University of Pretoria, Pretoria 0028, South Africa*

[2] *Department of Physics, Obafemi Awolowo University, Ile-Ife 220005, Nigeria*

[3] *Department of Materials Science and Engineering, African University of Science and Technology (AUST), Abuja, Federal Capital Territory, Nigeria*

ABSTRACT

In this study, activated carbon was derived from polypyrrole (PPY) using a K_2CO_3 activating agent with varying mass ratios of the activating agent to PPY polymer (AA:PP), for the optimization of the hierarchical pore structure necessary for improved electrochemical performance. The textural study of the as-synthesized samples (AC-PPY) displayed an increase in the specific surface area (SSA) and pore volume with increase in the amount of the activating agent up to a threshold for AA:PP of 6:1. The increase in the SSA was due to the presence of hierarchical pores in the material structure for efficient ion penetration. Initial half-cell electrochemical tests performed on the different activated carbon samples with varying SSA revealed superior charge storage capability for the 6:1 sample in both negative and positive operating potentials. The highest current response value was obtained from the signatory EDLC-type cyclic voltammogram, along with the longest discharge time from the chronopotentiometry plot as a result of the lowest ion diffusion length for successful fast ion transport reported from the impedance spectroscopy analysis. A full symmetric device (AC-PPY-6) assembled from the best material using KNO_3 neutral electrolyte yielded a specific capacitance of 140 F g^{-1}, 12.4 Wh kg^{-1} energy density at 0.5 A g^{-1} gravimetric current. An energy density of 7.12 Wh kg^{-1} was still maintained at a specific current of 2 A g^{-1}. Interestingly, after the ageing test to ascertain device stability, the device energy density increased back to 12.2 Wh kg^{-1} as a result of the creation of additional active pores within the nanostructured material for charge storage via voltage holding tests which also led to the enhancement in specific capacitance to 137.5 F g^{-1} at 2 A g^{-1}. A 99.0% capacitance retention was recorded even after 10000 cycles at a moderate

Address correspondence to E-mail: ncholu.manyala@up.ac.za

Springer

specific current of 2 A g^{-1}. A substantial approach was used to elucidate the degradation phenomena from the device self-discharge profile, which showcased the device retaining up to 70% of its operating potential after 80 h (> 3 days) on open circuit. The results obtained demonstrate the potential of adopting the AC-PPY material in potential device for energy storage purposes.

Introduction

The exponentially increasing global demand for energy, coupled with the fossil fuels consumption and the related greenhouse gas (CO$_2$) emissions causing global warming [1], has led to the search for alternative energy sources. This has also led to the development of new technologies using renewable, clean and sustainable energy resources over the last couple of decades. However, one of the major issues underplaying these new technologies lies in the ability to store and supply the generated energy based on specific requirements in addition to the generated surplus in some instances which might not be needed at that occasion. Efficient energy storage technologies, such as batteries and recently supercapacitors, have been at the forefront of this research and are essentially exploited to proffer solution to the current energy crisis.

Supercapacitors (SCs) are high power technological devices capable of powering portable electronic devices and transportation systems due to their quick power delivery and extended cycle life [2, 3]. The charging time of SCs ranges from seconds to minutes which brings about their fast energy harvesting, but SCs store less energy when compared with most batteries [4]. Nevertheless, efforts to improve the SCs performance without sacrificing their high power density and cycling life need to be further explored, especially through exploring cheaper and new classes of electrode materials, (including oxides, 2-D materials, sulphides, transition metal carbides) and also the electrolytes [4]. Carbon is the typical material adopted in electrochemical double-layer capacitors (EDLCs) in which the charge storage occurs at the electrode–electrolyte interface. In particular, activated carbons (ACs) are the only commercially available carbon used in the energy storage industry due to its adequate porosity, high specific surface area, high electrical conductivity and good chemical stability [5–7].

Many of the ACs produced are based on template methods and are very efficient for the production of porous carbon with excellent and tuneable properties [8–10]. However, the difficulty with template-based approach is the usage of expensive materials such as silica and zeolite as templates [11, 12]. Other techniques adopted for the production of the carbon materials are the chemical and physical methods [13, 14]. The chemical treatment usually results in the formation of an aerogel or hydrogel material while the physical method (activation mostly with KOH, ZnCl$_2$ and H$_3$PO$_4$) and carbonization at elevated temperatures lead to the formation of porous carbons [15–17].

Many research groups have adopted the latter approach for the production of porous carbon from diverse sources of carbon ranging from inorganic to organic and biomass sources. For example, hydrochars were transformed into porous carbons via hydrothermal carbonization by Wei et al. [18]. Three-dimensional hierarchical porous carbon using KOH activation was reported for use in high-performance supercapacitors by Qie et al. [19]. The as-obtained carbon displayed a large specific surface area (SSA) of about 2870 m^2 g^{-1}, high-level of heteroatom doping (N: 7.7 wt%, O: 12.4 wt%) and good electrical conductivity (5.6 S cm^{-1}). Furthermore, ultrahigh surface area carbon based on polypyrrole was obtained via chemical activation of polypyrrole with KOH by Sevilla et al. [20]. The as-synthesized carbon exhibited an excellent gravimetric and volumetric capacity due to the fact that their high porosity ensured high packing density. Pinecone biomass was also converted into porous carbon via KOH activation and carbonization at 800 °C. The porous carbon material exhibited a mesoporous framework with a SSA of 1515 m^2 g^{-1}, a gravimetric capacitance of 137 F g^{-1}, energy density of 19 Wh kg^{-1} in 1 M Na$_2$SO$_4$ electrolyte within a 2.0 V operating voltage [21]. In similar processes related to KOH activation, porous carbons derived from tree bark biomass were also explored as possible electrodes for electrochemical application with an optimization of the synthesis conditions [22].

Very recently, a new perspective has evolved in the materials activation field to produce porous carbons with less negative impact on the environment. This is due to the fact that KOH activation which is the common activating route is perceived to have environmental issues due to corrosive effects (highly alkaline) of KOH, which limits its use on a large scale [23]. Thus, environmentally benign approaches to produce porous carbons are necessary. Recently, a green approach towards achieving microporous carbon materials for high-performance supercapacitor electrodes was reported [23]. The activation of the materials was carried out via a mild chemical activation of the samples with potassium bicarbonate ($KHCO_3$), where it was concluded that the environmental benefits of this activating agent are supplemented by a 10% increase in the yield. It was also reported that the morphology of the starting material is retained after activation, ensuring better packing properties along with a reduced ion diffusion distances, all beneficial for improved electrochemical performance. Based on this, the motivation was developed to explore a similar activating agent potassium carbonate (K_2CO_3) to produce porous carbon from a conducting polymer known as polypyrrole (PPY). Our choice of the activating agent originally lies in the above-mentioned characteristics owing to the fact that $KHCO_3$ still decomposes to form K_2CO_3 which also retains the material morphology as reported earlier. PPY in its capacity also has a higher density and conductivity when compared to other conducting polymers [24], which we believe will lead to porous carbon materials with good electronic properties. PPY is a cost-effective and environmentally stable polymer with high conductivity and can provide high electrochemical performance in small volumes, and it is highly flexible [25–27]. Studies have recently been conducted to look into the flexible nature of PPY and its influence as a supercapacitor. According to Huang et al. [26], the intrinsic stretching ability of the material can maintain or enhance its performance.

Thus, in this work, we present the electrochemical performance analysis of a PPY-derived nanoporous carbon material electrode in a neutral 2.5 M KNO_3 aqueous electrolyte. Most importantly, the device fabricated was relatively stable at a high voltage of 1.6 V, exhibiting an energy density of 12.4 Wh kg^{-1}, excellent capacitance retention of 99% (only a 1% loss) for up to 10000 cycles, which was improved through floating test. The self-discharge test performed also showcased the material retaining up to 70% of its operating voltage for up to 80 h. The results obtained from this study further provide more information into efficiently designing supercapacitor devices for efficient use in energy storage units.

Experimental

Synthesis of activated carbon of polypyrrole

Polypyrrole (PPY) was prepared via a procedure reported previously [28]. The obtained PPY powder was mixed chemically with potassium carbonate anhydrous (K_2CO_3) in different K_2CO_3 mass proportions denoted as 0:1, 2:1, 4:1, 6:1 and 8:1, respectively. Each sample was then carbonized for 2 h at 800 °C with a ramping rate of 5 °C/min under argon gas flow. The activated carbon was then sonicated in 1 M HCl to remove the remaining unreacted salts and continuously rinsed with de-ionized water to attain a neutral pH. Oven drying was done at 60 °C for 12 h.

Physico-chemical characterization

The material textural properties were obtained using the Brunauer–Emmett–Teller (BET) technique from a Micrometrics Tristar II 3020 (version 2.00) Analyser at − 196 °C. The pore size distribution plot was obtained from the desorption branch of the Barrett–Joyner–Halenda (BJH) plots.

Scanning electron microscopy technique (using a Zeiss Ultra plus field emission scanning electron microscope, FESEM) was used to study the morphological properties of the as-synthesized activated carbon from polypyrrole denoted as AC-PPY-X henceforth, with $X = 0$, 2, 4, 6 and 8 for K_2CO_3:PPY ratio of 0:1, 2:1, 4:1, 6:1 and 8:1, respectively. The elements present in the prepared activated carbon were also revealed using energy dispersive X-ray (EDX) analyser attached to the FESEM. The EDX sample was prepared by mixing epoxy resin with the active material and allowed to solidify in an electric oven at 60 °C for 36 h.

The Raman spectra for the samples were obtained using a micro-Raman WITec confocal system preset to a 532-nm-wavelength laser at 50 mW power. The images were focused using a 50× objective lens, which was used to optimize the Raman spectra response.

Electrochemical characterization

Electrochemical analysis of the AC-PPY-X samples was done on a VMP300 Bio-Logic instrument. The electrodes were prepared by mixing the active AC-PPY-X material with polyvinylidene fluoride (PVDF) binder, carbon black in a mass ratio of 80:10:10 and few drops N-methyl-2-pyrrolidone (NMP) to make slurry. The slurry was homogeneously coated on nickel foam (NF) current collector and dried at 60 °C. Three-electrode measurements were taken initially to fully understand the charge storage behaviour of the half-cell electrode in a 2.5 M KNO_3 electrolyte using an Ag/AgCl reference electrode and glassy carbon counter electrode.

A symmetric electrochemical capacitor device was subsequently assembled in a coin cell type configuration with filter paper as the separator and 2.5 M KNO_3 as the operating electrolyte. The total mass of active material per unit area on each electrode in the full device was ca. 2.30 mg cm^{-2}. The cyclic voltammetry (CV) and chronopotentiometry (CP) measurements were investigated at different scan rates and gravimetric current densities, respectively. The electrochemical impedance spectroscopy (EIS) tests were run in a frequency range of 100 kHz to 0.01 Hz at open circuit potential. The specific capacitance of a single electrode was calculated from the slope of the CP plot according to Eqs. (1) and (2):

$$C_{el} = \frac{4I\Delta_t}{\Delta V_m} \tag{1}$$

$$C_{sp} = \frac{C_{el}}{4} \tag{2}$$

The energy density and the corresponding power density of the complete device were calculated according to Eqs. (3) and (4):

$$E_d = \frac{1}{2}C_{sp}(\Delta V)^2 = \frac{C_{el}(\Delta V)^2}{28.8} \ (\text{Wh kg}^{-1}), \tag{3}$$

$$P_d = 3600\frac{E_d}{\Delta t}(\text{W kg}^{-1}), \tag{4}$$

where m is the total mass of the electrode material, C_{el} is the specific capacitance of a single electrode, C_{sp} is the specific capacitance of the cell, I is the current applied, Δt is the discharge duration and ΔV is the device voltage window.

Results

The results from the textural analysis done on the as-synthesized AC-PPY samples (shown in Fig. 1) displayed the N_2-absorption–desorption isotherm of type VI with a hysteresis loop present, which is attributed to the adsorbate condensation in the hierarchical pores within the porous carbon materials [29]. The quantity of gas absorbed was observed to increase as the amount of K_2CO_3 was added to the raw material up to a limiting point "X" at 6:1 (AA:PP) after which it decreased. This observation is suggested to be due to pore enlargement and possible breakdown of the porous carbon framework by excess activating agent leading to the widening and possible collapse of pore sites [22, 30]. Figure 1b shows the associated plot illustrating the exact values of BET SSA variance with activating agent ratio. As observed, a drop is observed once the ratio exceeded 6.

The pore size distribution (PSD) plot (Fig. 1c) calculated by the Barrett–Joyner–Halenda (BJH) branch shows the nature of the pore range present within the activated carbon sample.

A combination of micropores and mesopores is observed from the PSD plot. A summary of the BET SSA and pore sizes for the AA:PPY-X samples is tabulated in Table 1.

The structural characteristic of the carbon material was investigated using the observed peaks obtained from the Raman spectroscopy tests. Figure 1d displays the Raman spectra for the pristine AC-PPY material without any activating agent as well as those for the activated carbon samples with varying activating agent content. A distinct peak (*) is recorded at a wavenumber of 1100 cm^{-1}, which is linked to the pristine polymer material due to the fact that this peak is present in all activated samples.

However, the intensity of the peak reduces with the introduction of an activation/carbonization process.

This is likely due to the conversion of the polymer into disordered graphitic carbon. For all other samples activated and carbonized, the distinct D- and G-peaks are obtained which confirms the successful conversion of the polymer into a highly disordered carbonaceous material [31].

This agrees with results [32, 33] obtained from other studies with similar porous activated carbon material and thus confirms the presence of sp^2 graphitic-type carbon with C–C bonds.
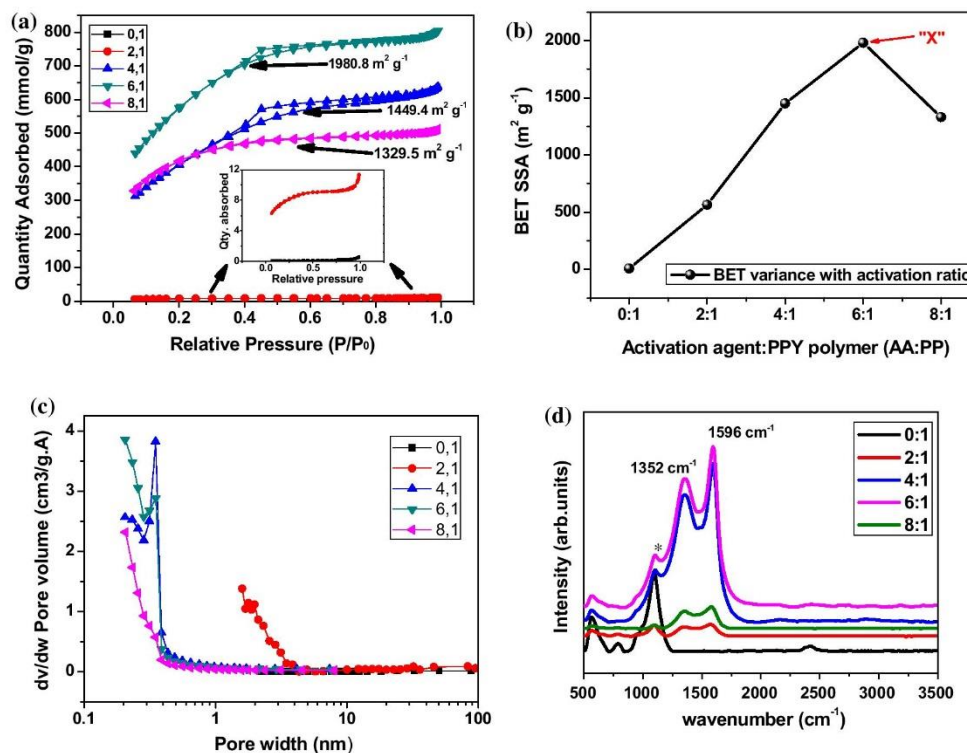
Figure 1 **a** N_2 absorption/desorption isotherm, **b** variance of BET SSA with activating agent content, **c** pore size distribution plots for the different activated samples from PPY-conductive polymer and **d** Raman spectra of the different activated samples showing the distinct carbonaceous D- and G-peaks.

Table 1 Summary of textural properties of activated carbon from PPY samples

Sample	Specific surface area (S_{BET}, $m^2 \, g^{-1}$)	Total pore volume (V, $cm^3 \, g^{-1}$)	Micropore volume (V_{micro}, $cm^3 \, g^{-1}$)	Mesopore volume (V_{meso}, $cm^3 \, g^{-1}$)	Average pore diameter (nm)
0:1	7.57	0.02	0.00	0.02	9.82
2:1	562.83	0.38	0.057	0.32	2.68
4:1	1449.42	0.98	0.019	0.96	2.75
6:1	1980.81	1.24	0.029	1.21	2.50
8:1	1329.47	0.79	0.14	0.65	2.38

To endorse the potential use of this material for supercapacitor application, the electrochemical performance of the AC-PPY electrode material was evaluated in a three-electrode system with 2.5 M KNO_3 as the aqueous electrolyte.

Firstly, cyclic voltammetry (CV) and chronopotentiometry (or galvanostatic charge–discharge) (CP or GCD) measurements were taken. Figure 2a shows the CV curves of all electrode materials activated with different K_2CO_3:PPY ratio at 20 mV s^{-1}. The samples all exhibited rectangular-shaped CV curves between 0 and 0.8 V, showing the typical EDLC behaviour. Furthermore, the charge separation (current response) seems to be enhanced with increasing K_2CO_3:PPY ratio up to 6:1 before diminishing with higher K_2CO_3:PPY ratio. The electrochemical performance is found to be intimately related to the K_2CO_3:PPY used during the electrode material preparation as shown from the BET SSA in Fig. 1b. Explicitly, both the BET SSA and charge separation
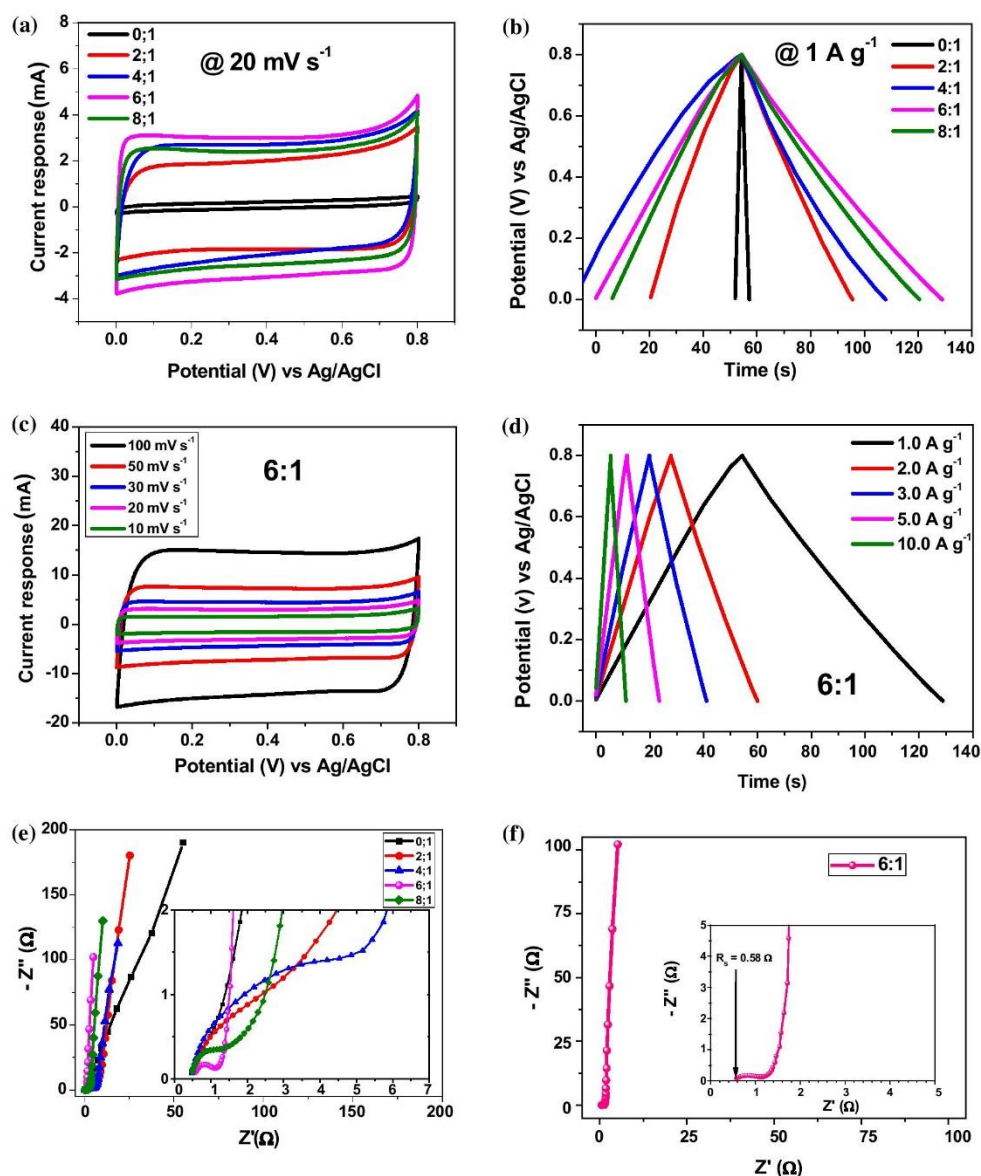
Figure 2 **a**, **b** Cyclic voltammetry (CV) and associated chronopotentiometry (CP) plots of activated carbon from PPY (AC-PPY) with varying quantities of K_2CO_3; **c**, **d** detailed CV and the related CP profile of AC-PPY-6 sample at varying scan rates and current densities; **e**, **f** EIS plot of the AC-PPY-X electrodes for different quantities of K_2CO_3 and **f** the AC-PPY-6 sample in a 2.5 M KNO_3 electrolyte.

increase with increasing K_2CO_3:PPY ratio, reaching a maximum value at a ratio of 6:1. Upon introduction of more activating agent, a decrease in current response was recorded showing that the best sample is the one synthesized at a ratio of 6:1.

For this ratio, the higher SSA and the presence of hierarchical micropores necessary for storage and high power performance at high gravimetric current will boost its capacitive performance. Furthermore, the observed rectangular shape of the CV profile

suggests small resistive behaviour for this electrode material.

Figure 2b shows the CD plots of all electrode materials at a current density of 1 A g^{-1}. Typical triangular-shaped CD curves for EDLCs are observed for all electrodes. In addition, the discharge time and consequently the capacitance increase with increasing K_2CO_3:PPY ratio up to 6:1. Additional increase in the ratio led to a decreased discharge time and charge storage capacity. It is observed that the 4:1 sample had a longer charge period as compared to discharge process. It is suggested that this is due to the presence of functional groups which are only active during the charging step but become inactive during the discharge process.

This is in good agreement with the CV results, confirming the high capacitive performance of the electrode synthesized with a K_2CO_3:PPY ratio of 6:1. The best electrode was further analysed by varying the sweep rate and the current density. Figure 2c shows the CV curves of AC-PPY-6 at different current densities. The rectangular shape is preserved even at a high scan rate of 100 mV s^{-1}, with no apparent distortion when compared to its shape at lower sweep rate. This confirms the insignificant resistive behaviour of the electrode material, which could otherwise reduce the capacitive performance of the electrode material.

Figure 2d displays the CP plot of the AC-PPY-6 electrode at different values of gravimetric current. The triangular curve is visible for all current densities with no significant IR drop, confirming the low equivalent internal resistance of the electrode.

To fully understand the electrical properties and electrochemical performance of the carbon-based electrode materials, EIS measurements were also taken and the results are shown in Fig. 2e.

The solution resistance which is equivalent to the equivalent series resistance (ESR) is approx. 0.5 Ω for all electrodes. However, the discrepancy appears for the charge transfer resistance (R_{ct}) obtained from the diameter of the semicircular part of the Nyquist plot in the high-frequency region. The electrode material activated with K_2CO_3:PPY in ratio of 6:1 displayed the smallest R_{ct} value with the shortest diffusion length.

The angle of the Nyquist plot with the Z'-axis at the low-frequency region defines the capacitive behaviour of the material electrode [34]. An ideal capacitor has a complete vertical line which is parallel to the imaginary impedance axis at the low-frequency region. The AC-PPY-6 sample displays the capacitive response closest to the ideal capacitance. The results from the impedance spectroscopy analysis are in good agreement with the results discussed in Fig. 2a.

In summary, the AC-PPY-6 material has the lowest leakage current associated with the highest charge separation, longest discharge time and highest BET SSA, as compared to the other electrode materials with varying K_2CO_3 content. Therefore, activation of the PPY with K_2CO_3 in a AA:PP ratio of 6:1 gives a material with the best electrochemical performance necessary for energy storage application.

The AC-PPY-6 nanostructured material electrode was further used in the fabrication of a full symmetric device. As shown in Fig. S2(a), this electrode works symmetrically from − 0.8 to 0 V and from 0 to 0.8 V, with very similar current response. This predicts a stable working potential window of 1.6 V for the full cell, as shown in Fig. 3a, which displays the CV profile of the full cell at different scan rates.

The rectangular shape is still maintained for scan rate up to 50 mV s^{-1}, demonstrating the fast ion diffusion kinetics and the fast current response on voltage reversal of this electrode.

Figure 3b shows the CP plot of the symmetric supercapacitor at different current densities. The triangular shape remains for all the applied current density values, exhibiting a good capacitive behaviour. The specific capacitance calculated from the CP plots is displayed in Fig. 3c.

The specific capacitance showed a steep decrease from 140 to 80 F g^{-1} when the current density was increased from 0.5 to 2.0 A g^{-1}. In other words, more than half of the initial capacitance is retained when the current density is quadrupled. Further increase in the current density has less significant effect on the specific capacitance which varied from 80 to 65 F g^{-1} for an increase in current density from 2.0 to 10.0 A g^{-1}. This corresponds to an impressive 81% of capacitance retention between 2.0 and 10.0 A g^{-1}.

This high rate capability is not only related to the fast diffusion kinetic of the electrolyte ions but also to the existence of suitable pores contained within the active electrode material required for energy storage application. Figure 3d shows the Ragone plot of the symmetric cell.

A high energy density of 12.4 Wh kg^{-1} corresponding to a power density of 415 W kg^{-1} is calculated at a
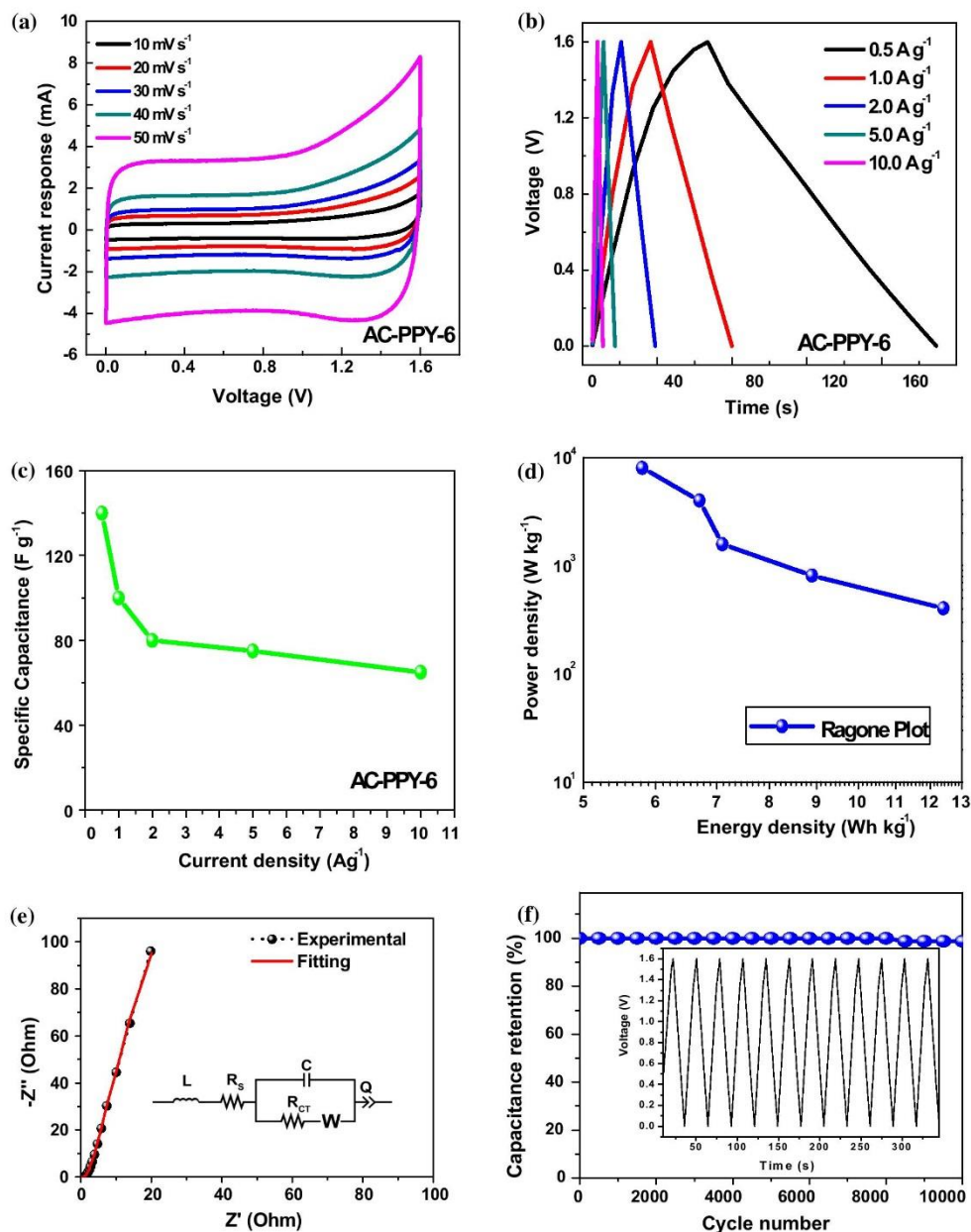
<img>⚛ Springer</img>

Figure 3 Electrochemical performances of the AC-PPY-6 symmetric device showing **a**, **b** CV and CP plots at different scan rates and gravimetric current densities; **c** associated specific capacitance as a function of gravimetric current density; **d** relationship between current density of 0.5 A g^{-1}. The energy density remained at 5.8 Wh kg^{-1} corresponding to a power density of 8 kW kg^{-1} at a current density of 10 A g^{-1}.

energy density and power density; **e** EIS plot showing the equivalent series circuit fitted to the plot and **f** capacitance retention versus cycle number with the figure inset showing a few galvanostatic charge–discharge cycles at 2 A g^{-1}.

The cycling stability of the cell was also investigated with continuous charging–discharging for up to 10000 cycles at a current density of 2 A g^{-1} (see Fig. 3f).

Springer

The cell retained 99% of its initial capacitance up to 10000 cycles, hinting at a negligible deterioration of the electrode material upon cycling.

Figure S2(b) shows the EIS Nyquist plot before and after cycling. An increase in the R_s value as well as the decrease in the ideal EDLC response based on the slope of the Nyquist plot in the low-frequency region was observed after cycling, which accounts for the slight decrease in specific capacitance.

Further ageing test was done by alternately holding the cell at its maximum voltage for an extended period of time while subjecting the device to constant charging–discharging steps at every 10 h intervals for more than 3 days. The specific capacitance was calculated from the average discharge time from the charge–discharge plot at each 10 h interval, and the result is presented in Fig. 4a. This experiment aimed at studying any deteriorating effect from holding the device at its maximum operating voltage for a prolonged period of time.

The result obtained can be divided into four steps: an increase in specific capacitance after the first 10 h of voltage holding, a constant device specific capacitance recorded from 10 to 40 h, a further increase in the specific capacitance from 40 to 60 h before stabilizing onwards. The first increase could be related to the time needed for a good wettability of the electrolyte on the surface of the electrode material. In other terms, within the first 10 h, the wettability of the electrode material could improve and subsequently more ions are stored at the electrode/electrolyte interface. The second increase is most likely related to the availability of more pores which were not participating in the initial storage process. The accessibility of these new pores is due to the repeated cycling and voltage holding, which could force the ions into these hidden pores. It is worth noting that the specific capacitance has almost doubled after the ageing experiment, increasing from 75 to 137.5 F g^{-1}. This will also result in an increase in the energy
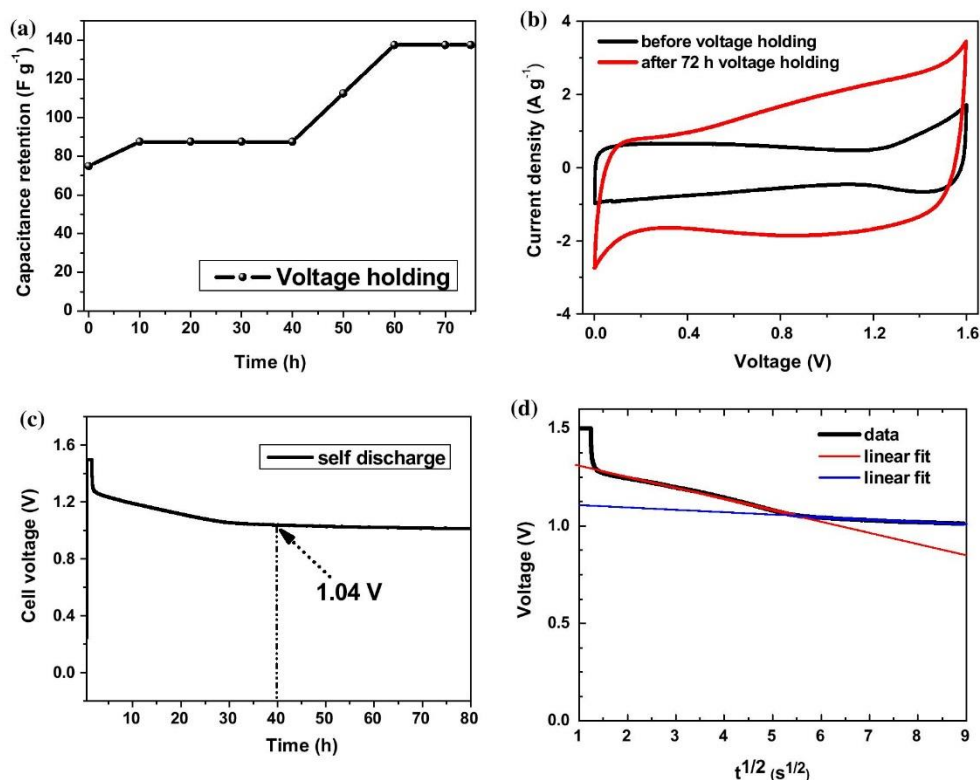

Figure 4 **a** Specific capacitance variation with voltage holding time for a period of 72 + h (3 days), **b** CV profile before and after voltage holding, **c** self-discharge profile for a period of 80 h and **d** fitting of self-discharge curve as a function of $t^{1/2}$ with two lines.

⚫ Springer

86

density from 6.7 to 12.2 Wh kg^{-1} at 2 A g^{-1}. This corresponds to an approx. 91% energy increase after ageing tests. Therefore, assuming similar increase for all current densities, one can predict an energy density as high as 23.7 Wh kg^{-1} at 0.5 A g^{-1} and 11.1 Wh kg^{-1} at 10 A g^{-1} after voltage holding.

Note that the energy density at 10 A g^{-1}, after ageing test, is almost equal to that of the cell at 0.5 A g^{-1}, before the ageing test. Thus, a good approach in optimizing the energy density of this symmetric supercapacitor will be to use it after ageing test. This symmetric supercapacitor matches the energy density of supercapacitors reported in the literature and even outperformed them in certain cases as shown Table 2. These excellent electrochemical properties of the symmetric cell are also linked to the small solution and charge transfer resistances observed from Fig. 3e.

In order to elucidate the increase in the specific capacitance value after ageing test, the CV curves before and after floating test are shown in Fig. 4b. A higher charge separation was observed after floating, owing to the augmentation of accessible pores for energy storage after the floating test.

This is in line with the increase in the specific capacitance value since more ions can be stored after floating, substantially increasing the specific capacitance.

Self-discharge experiment, related to the loss of voltage associated with the difference in Gibbs'

energy between the charged and the discharged states, was also performed.

The results from tests performed on the cell are as presented in Fig. 4c. The cell was charged up to 1.5 V and held at this potential for 1 h in order to minimize charge redistribution. Thereafter, the behaviour of the cell at open-circuit voltage was investigated.

Since no current can flow through an external circuit in open circuit configuration, only Faradaic reactions dissolving impurities in the electrolyte, decomposition of the electrolyte or more Faradaic reactions occurring at the surface of the electrode material, can explain the self-discharge phenomenon. A steep decrease in the voltage down to 1.27 V within the first minute of self-discharge is noticed.

This was followed by a much slower discharge up to 1.04 V from 40 up to 80 h. The first voltage loss could be associated with the instability of the aqueous electrolyte which could generate oxygen.

This phenomenon becomes more apparent when the applied voltage is removed unlike in previous experiment shown in this study. The instability of the electrolyte becomes less visible below 1.27 V, which coincides with thermodynamic potential of water at 1.23 V.

Diffusion-controlled mechanism for self-discharge can be fitted with Eq. (5) below:

$$V_t = V_i - m \cdot t^{1/2}, \tag{5}$$

Table 2 Comparison of the properties of symmetric cells based on carbonaceous-type materials and PPY in aqueous electrolytes

Symmetric cell	Electrolyte	I (A g^{-1})	v (mV s^{-1})	E_d (Wh kg^{-1})	P_d (W kg^{-1})	References
Activated carbon-fibre with NaOH and KOH	6 M KOH	–	50	8.1	–	[35]
Activated carbon from pomelo peel	1 M NaNO$_3$	0.50	–	17.1	420	[36]
Carbon nanopetal/PPY nanocomposite	1 M LiClO4	–	–	38.9 Wh kg^{-1}	–	[37]
Polypyrrole/carbon fibres	LiClO$_4$/PVA gel electrolyte	–	–	1.0	680	[38]
Reduced graphite oxide	1 M Na$_2$SO4$_4$	0.10	–	10.4	–	[39]
3-D carbon framework	1 M Na$_2$SO4$_4$	0.20	–	12	400	[40]
Mesoporous carbon	6 M KOH	0.05	–	7.84	–	[41]
Hierarchical porous carbon	KOH/PVA	0.50	–	19.74	500	[42]
N-doped carbon network	1 M Na$_2$SO$_4$		–	24.8	29600	[43]
Nanoporous carbon	2.5 M KNO$_3$	0.50	–	12.4 (BF)[a] 22.7 (AF)[b]	404 (BF)	This work

[a]Before floating test

[b]After floating test

where V_t is the voltage at a given self-discharge time, V_i is the maximum voltage, t is the self-discharge time and m is a constant which depends on the diffusion and geometrical parameters of the material electrode [44].

In other words, the plot of V_t as a function of $t^{1/2}$ must be linear for a diffusion-controlled self-discharge mechanism. As shown in Fig. 4d, the curve can be fitted with two lines with different m-value, suggesting two diffusion-controlled mechanisms. Therefore, one could think of the possible involvement of O_2 and H_2 generated from the electrolyte decomposition. These elements can deplete the ions stored at each interface with the electrode material, forming new species that could dissolve in the electrolyte [45]. A lowering of the initial voltage applied below the thermodynamic potential of water could mitigate this self-discharge phenomenon. However, a relatively good potential of 1.04 V was still maintained on the cell up to 80 h of self-discharge.

Conclusion

In this experiment, the textural properties and electrochemical performance of activated carbon synthesized from a conducting polypyrrole polymer (AC-PPY) was determined. The AC-PPY was prepared using a chemical activation method with varying amounts of K_2CO_3 activating agent to polymer raw materials (AA:PP) in the ratios 0:1, 2:1, 4:1, 6:1 and 8:1.

The samples were then carbonized via a chemical vapour deposition system at 800 °C for a period of 2 h. From the BET results obtained, an optimized 6:1 AA:PP ratio yielded the sample with the highest BET specific surface area and pore volume combination. Further increase in the amount of activating agent only resulted in a decrease in both the SSA and pore volume recorded.

The initial three-electrode electrochemical tests showcased the AC-PPY-6 sample electrode giving the highest current response from the cyclic voltammetry test within an operating potential window of 0.8 V in both positive and negative ranges. The CV curves all exhibited the characteristic EDLC rectangular response signifying the charge storage mechanism were mainly electrostatic in origin. From the chronopotentiometry sample tests, the AC-PPY-6

sample also had the highest discharge time and corresponding specific capacitance (C_S) calculated from the slope of the discharge plot. The C_S values decreased with increasing specific current, which is linked to the failure of ions to adequately access inner charge storage porous sites due to the limited ion transport at increased current densities [46, 47] The electrochemical impedance spectroscopy test correlated with the results obtained from the CD and CV tests with the sample with the AA:PP of 6:1 exhibiting the shortest charge transfer resistance and diffusion length for successful ion transport.

A symmetric device fabricated from the optimized sample recorded an operating voltage of 1.60 V as shown in the cyclic voltammetry tests. The quasi-rectangular shape of the CV curves was maintained, demonstrating the fast ion diffusion kinetics and fast current response on voltage reversal. A specific capacitance of 140 F g^{-1} was obtained at a 0.5 A g^{-1} specific current. The cell retained 99% of its initial capacitance after continuously cycling for 10000 charge–discharge cycles at 2.0 A g^{-1}, showing that there is no significant deterioration (relative stability) of the electrode material assembled in the device. An extended ageing test was conducted to further confirm the device stability at its maximum operating voltage with charge–discharge tests included to monitor the specific capacitance at 10-h intervals. The device specific capacitance was pointedly found to improve after voltage holding tests which was linked to the wettability of the electrode coupled with its ability to store more ions as well as the generation of initially redundant pores which were not participating in the initial storage process. The specific capacitance of the device increased from 75 to 137.5 F g^{-1} at 2.0 A g^{-1} at after the ageing test. This tallied with a similar increase in the device energy density from 6.7 to 12.2 Wh kg^{-1} at a current density of 2.0 A g^{-1} suggesting ageing tests as a potential route to improving device performance.

Acknowledgements

Electronic supplementary material: The online version of this article (https://doi.org/10.1007/s10853-017-1911-y) contains supplementary material, which is available to authorized users.

References

[1] Simon P, Gogotsi Y, Dunn B (2014) Where do batteries end and supercapacitors begin? Science 80(343):1210–1211

[2] Lukatskaya MR, Dunn B, Gogotsi Y (2016) Multidimensional materials and device architectures for future hybrid energy storage. Nat Commun 7:12647

[3] Chabi S, Peng C, Hu D, Zhu Y (2014) Ideal three-dimensional electrode structures for electrochemical energy storage. Adv Mater 26:2440–2445

[4] Béguin F, Presser V, Balducci A, Frackowiak E (2014) Carbons and electrolytes for advanced supercapacitors. Adv Mater 26:2219–2251, 2283

[5] Pandolfo AG, Hollenkamp AF (2006) Carbon properties and their role in supercapacitors. J Power Sources 157:11–27

[6] Simon P, Gogotsi Y (2008) Materials for electrochemical capacitors. Nat Mater 7:845–854

[7] Simon P, Gogotsi Y (2013) Capacitive energy storage in nanostructured carbon-electrolyte systems. Acc Chem Res 46:1094–1103

[8] Nishihara H, Kyotani T (2012) Templated nanocarbons for energy storage. Adv Mater 24:4473–4498

[9] Yu C, Fan J, Tian B et al (2002) High-yield synthesis of periodic mesoporous silica rods and their replication to mesoporous carbon rods. Adv Mater 14:1742–1745

[10] Meng W, Chen W, Zhao L, Huang Y, Zhu M, Huang Y, Fu Y, Geng F, Yu J, Chen X, Zhi C (2014) Porous Fe_3O_4/carbon composite electrode material prepared from metal-organic framework template and effect of temperature on its capacitance. Nano Energy 8:133–140

[11] Kyotani T, Ma Z, Tomita A (2003) Template synthesis of novel porous carbons using various types of zeolites. Carbon 41:1451–1459

[12] Basavalingu B, Calderon Moreno JM, Byrappa K et al (2001) Decomposition of silicon carbide in the presence of organic compounds under hydrothermal conditions. Carbon 39:1763–1766

[13] Lillo-Rodenas MA, Cazorla-Amoros D, Linares-Solano A et al (2003) Understanding chemical reactions between carbons and NaOH and KOH: an insight into the chemical activation mechanism. Carbon 41:267–275

[14] Raymundo-Pinero E, Azais P, Cacciaguerra T et al (2005) KOH and NaOH activation mechanisms of multiwalled carbon nanotubes with different structural organisation. Carbon 43:786–795

[15] Wang T, Tan S, Liang C (2009) Preparation and characterization of activated carbon from wood via microwave-induced $ZnCl_2$ activation. Carbon 47:1880–1883

[16] Liu Q-S, Zheng T, Wang P, Guo L (2010) Preparation and characterization of activated carbon from bamboo by microwave-induced phosphoric acid activation. Ind Crops Prod 31:233–238

[17] Wang J, Kaskel S (2012) KOH activation of carbon-based materials for energy storage. J Mater Chem 22:23710

[18] Wei L, Sevilla M, Fuertes AB et al (2011) Hydrothermal carbonization of abundant renewable natural organic chemicals for high-performance supercapacitor electrodes. Adv Energy Mater 1:356–361

[19] Qie L, Chen W, Xu H et al (2013) Synthesis of functionalized 3D hierarchical porous carbon for high-performance supercapacitors. Energy Environ Sci 6:2497

[20] Sevilla M, Mokaya R, Fuertes AB (2011) Ultrahigh surface area polypyrrole-based carbons with superior performance for hydrogen storage. Energy Environ Sci 4:2930–2936

[21] Bello A, Manyala N, Barzegar F, Khaleed AA, Momodu DY, Dangbegnon JK (2016) Renewable pine cone biomass derived carbon materials for supercapacitor application. RSC Adv 6:1800–1809

[22] Momodu D, Madito M, Barzegar F, Bello A, Khaleed AA, Olaniyan O, Dangbegnon J, Manyala N (2016) Activated carbon derived from tree bark biomass with promising material properties for supercapacitors. J Solid State Electrochem 21:859–872

[23] Sevilla M, Fuertes AB (2016) A green approach to high-performance supercapacitor electrodes: the chemical activation of hydrochar with potassium bicarbonate. Chemsuschem 9:1880–1888

[24] Snook GA, Kao P, Best AS (2011) Conducting-polymer-based supercapacitor devices and electrodes. J Power Sources 196:1–12

[25] Huang Y, Li H, Wang Z, Zhu M, Pei Z, Xie Q, Huang Y, Zhi C (2016) Nanostructured polypyrrole as a flexible electrode material of supercapacitor. Nano Energy 22:422–438

[26] Huang Y, Tao J, Meng W, Zhu M, Huang Y, Fu Y, Gao Y, Zhi C (2015) Super-high rate stretchable polypyrrole-based supercapacitors with excellent cycling stability. Nano Energy 11:518–525

[27] Yang P, Mai W (2014) Flexible solid-state electrochemical supercapacitors. Nano Energy 8:274–290

[28] Bello A, Barzegar F, Madito MJ et al (2017) Floating of PPY derived carbon based symmetric supercapacitor in alkaline electrolyte. ECS Trans 6:3–5

[29] Bello A, Barzegar F, Madito MJ, Momodu DY, Khaleed AA, Mashikhwa TM, Dangbegnon JK, Manyala N (2016) Stability studies of polypyrrole-derived carbon based symmetric supercapacitor via potentiostatic floating test. Electrochim Acta 213:107–114

[30] Yao L, Yang G, Han P, Tang Z, Yang J (2016) Three-dimensional beehive-like hierarchical porous polyacrylonitrile-based carbons as a high performance supercapacitor electrodes. J Power Sources 315:209–217

[31] Mao Y, Duan H, Xu B et al (2012) Lithium storage in nitrogen-rich mesoporous carbon materials. Energy Environ Sci 5:7950

[32] Sadezky A, Muckenhuber H, Grothe H, Grothe H, Niesnner R, Poschl U (2005) Raman microspectroscopy of soot and related carbonaceous materials: spectral analysis and structural information. Carbon 43:1731–1742

[33] Zhang H, Zhang L, Chen J, Su H, Liu F, Yang W (2016) One-step synthesis of hierarchically porous carbons for high-performance electric double layer supercapacitors. J Power Sources 315:120–126

[34] Momodu DYY, Barzegar F, Abdulhakeem B, Dangbegnon J, Masikhwa T, Madito M, Manyala N (2015) Simonkolleite-graphene foam composites and their superior electrochemical performance. Electrochim Acta 151:591–598

[35] Hu S, Zhang S, Pan N, Lo Hsieh Y (2014) High energy density supercapacitors from lignin derived submicron activated carbon fibers in aqueous electrolytes. J Power Sources 270:106–112

[36] Peng C, Lang J, Xu S, Wang X (2014) Oxygen-enriched activated carbons from pomelo peel in high energy density supercapacitors. RSC Adv 4:54662–54667

[37] Cherusseri J, Kar KK (2016) Hierarchical carbon nanopetal/polypyrrole nanocomposite electrodes with brush-like architecture for supercapacitors. Phys Chem Chem Phys 18:8587–8597

[38] Chang Y, Han G, Chang Y, Xiao Y, Hou W, Zhou W (2017) Flexible and compressible electrochemical capacitors based on polypyrrole/carbon fibers integrated into sponge. J Alloys Compd 708:1206–1215

[39] Shivakumara S, Kishore B, Penki TR, Munichandraiah N (2014) Symmetric supercapacitor based on partially exfoliated and reduced graphite oxide in neutral aqueous electrolyte. Solid State Commun 199:26–32

[40] Bello A, Barzegar F, Momodu D, Dangbegnon J, Taghizadeh F, Manyala N (2015) Symmetric supercapacitors based on porous 3D interconnected carbon framework. Electrochim Acta 151:386–392

[41] He X, Li R, Qiu J et al (2012) Synthesis of mesoporous carbons for supercapacitors from coal tar pitch by coupling microwave-assisted KOH activation with a MgO template. Carbon 50:4911–4921

[42] Hao P, Zhao Z, Tian J et al (2014) Hierarchical porous carbon aerogel derived from bagasse for high performance supercapacitor electrode. Nanoscale 6:12120–12129

[43] Wang Q, Yan J, Xiao Y et al (2013) Interconnected porous and nitrogen-doped carbon network for supercapacitors with high rate capability and energy density. Electrochim Acta 114:165–172

[44] Andreas HA (2015) Self-discharge in electrochemical capacitors: a perspective article. J Electrochem Soc 162:A5047–A5053

[45] Oickle AM (2013) A systematic study of self-discharge mechanisms in carbon-based, aqueous electrolyte electrochemical capacitors. Ph.D. dissertation, Chemistry Department, Dalhousie University

[46] Reddy RN, Reddy RG (2006) Porous structured vanadium oxide electrode material for electrochemical capacitors. J Power Sources 156:700–704

[47] Lao ZJ, Konstantinov K, Tournaire Y et al (2006) Synthesis of vanadium pentoxide powders with enhanced surface-area for electrochemical capacitors. J Power Sources 162:1451–1454